# Microprobe Investigations of Semiconductor Structures

Thesis by
Robert J. Miles
Adviser: Professor Thomas C. McGill, Fletcher Jones Professor
of Applied Physics

In Partial Fulfillment of the Requirements
for the Degree of
Doctor of Philosophy

California Institute of Technology
Pasadena, California

1995
(Submitted June 13, 1994)

to My Family

# Acknowledgements

My experience here at Caltech, though at times trying, has been extremely rewarding and had a profound effect on my young life. The stimulating intellectual day-to-day exchanges with fellow techno-warriors has been not only challenging but surprisingly fun. I count myself lucky of have associated with such a world-class group of individuals.

First and foremost, I am indebted to Tom McGill, my advisor. He forced me to grow as a student and researcher, by allowing me to test new ideas, make mistakes, and finally persevere. By exhibiting dogged determination to solve his own problems, he served as an excellent role model for myself and fellow researchers. His tutorials in technical writting along with guidelines such as "avoid cliches like the plague" proved invaluable. I look forward to working with Tom again in the future, whether in science, business, or simply solving the problems of the world.

I would also like to express the fun and satisfaction I had with interacting with all members of the group as well as the valuable lessons they have shared with me. Johanes Swenberg, who performed the ZnTe growns studied in this thesis, provided me insight into the difficulties of the II-VI world as well as thoughtful conservative political commentaries that remarkably approach my own views. Mike Wang, who performed the Auger and XPS analysis, proved that behind even the most innocent of faces lurks mischief and mayhem. Ron Marquardt, the quintessence of the straight man, showed that innocence can be an attractor of said mischief and mayhem.

Doug Collins, who was responsible of the III-V growths in chapter 5 of this thesis as well as some of the analysis, proved to me the difference between a good MBE user and an excellent one. He also convinced that Ginsing is better than any Assertiveness class I could take. Harold Levy as well as Doug are living proof that a messy desk is the sign of a creative mind. Harold also taught me that its best to follow your own vision, particularly when that vision involves goggles and an oxygen tank. Peo Pettersson, who performed the Si/$CaF_2$ growths in chapter 3 as well as some of the analysis, showed that socialists can be converted into capitalists, as long as they can make some money in the process.

I would also like to thank the theorists in the group, Chris Springfield, Yixin Liu, Dave Ting, and Shaun Kirby, who taught me that dealing with computers is alot like dealing with the God of the Old Testament; lots of rules and no mercy. Dave especially served as a abundant source of knowledge for transport theory, band structure, and Ginsing preparation.

I would also like to thank the other alumi and associates who molded my stay at Caltech; Ed Croke, Ed Yu, Mark Phillips, Ogden March, Gerald Picus, Jim McCaldin, Ron Grant. Thoughtful discussions with these people lead to many new insights for me. I would also like to thank the new members of the group, Alicia Alonzo, Erik Daniels, and Xiao-Chang "did I pronounce it corectly" Cheng, whose enthusiasm and anticipation of research made the last year not only motivational but also at times highly entertaining.

I would like to thank Marcia "I'd like you to meet my parents" Hudson for her infinite patience and her ability to keep things running smoothly under the most adverse conditions (i.e. working with graduate students). Her sense of humor and wit provided a welcome relief on days where little seemed to go right.

Finally I would like to thank my family, particularly my parents, for their love and understanding that at times seemed like the only things that kept me going.

# Abstract

This thesis describes the results of experimental studies of semiconductor structures using local microprobe techniques. The studies primarily concern two questions: the detection of local variations in material quality and transport properties, and the control of material preparation and growth to minimize these variations.

In chapter 2 we investigate the source of defects in nitrogen-doped ZnTe grown on ZnTe and GaSb substrates. Through the use of atomic force microscopy (AFM) and transmission electron microscopy (TEM), we find that defect generation is minimized on GaSb substrates with nitrogen delta-doping. Using selective etching techniques, we also show that the Zn $\{111\}$ fault planes tend to originate at the doping layers while Te $\{111\}$ fault planes tend to originate at the substrate/epilayer interface. A simple doping model from Chadi et al., explains the observed effect.

In chapter 3 we studied the effects of electron-beam-assisted molecular beam epitaxy (EB MBE) on the growth of Si on $CaF_2$/Si(111). By irradiating the surface of $CaF_2$ with low energy electrons, the surface free energy of the $CaF_2$ is raised and the subsequent Si layer is smoother. By using AFM, X-ray diffraction, and XPS, we find that an optimal range of exposures exist that minimizes surface roughness and we present a simple thermodynamic model to explain this. We further show that for temperatures below the epitaxial growth temperature of Si (500°C), the irradiation causes a transition in the Si grown from amorphous to ordered.

In chapter 4 we investigate the electrical properties of the intrinsic ZnTe(110) surface. Using scanning tunneling microscopy (STM) and spectroscopy, we find

a new criterion for determining the extent of Fermi level pinning. This criterion involves observing the enhancement of reverse bias current with increasing tip-sample separation. The mechanism is an increase in the tunneling transmission of carriers through the semiconductor's space charge region that more than compensates for the reduced tunneling transmission through the tip-sample gap as the tip retracts from the surface. We also find that upon subsequent exposure of the surface to contaminates, the surface becomes pinned.

Chapter 5 describes our ballistic electron emission microscopy (BEEM) investigations of semiconductor structures. We describe our studies of Au/Si(100) interfaces and show that the barrier height extracted from the spectroscopy using a simple model agrees well with the known Au/Si Schottky barrier height. We also present preliminary studies of InAs/AlAs/GaAs single barrier structures. Through frequency plots we feel we can confidently identify transport associated with specific local band structure, particularly the GaAs and AlAs Γ-pt.

Finally, in Appendix A we discuss the contemporary STM theories along with the theory we used for our calculations in chapter 4. In Appendix B, we discuss in detail the construction of BEEM equipment along with its operation.

# List of Publications

Work related to this thesis has been, or will be, published under the following titles:

**Surface Morphology of Silicon Grown on $CaF_2/Si(111)$ By Electron-Beam-Assisted MBE**

P. O. Pettersson, R. J. Miles, and T. C. McGill, to be published in Journal of Applied Physics.

**Temperature Dependence of Surface Morphology of Silicon Grown on $CaF_2/Si(111)$ By Electron-Beam-Assisted MBE** R. J. Miles, P. O. Pettersson, and T. C. McGill, to be published.

**Investigation of Crystal Quality and Surface Morphology of ZnTe:N Epilayers Grown on ZnTe and GaSb Substrates**

R. J. Miles, J.F. Swenberg, M.W. Wang, M. C. Phillips, and T. C. McGill, *J. Cryst. Growth* **138**, 523 (1994).

**Measurement of the MgSe/CdZnSe Valence Band Offset by X-ray Photoelectron Spectroscopy**

M.W. Wang, J.F. Swenberg, R. J. Miles, M. C. Phillips, E. T. Yu, J. O. McCaldin, R.W. Grant, and T. C. McGill, *J. Cryst. Growth* **138**, 508 (1994).

**Advances in the development of Graded Injector Visible Light Emitters** J.F. Swenberg, M.W. Wang, R. J. Miles, M. C. Phillips, and T. C. McGill, *J. Cryst. Growth* **138**, 692 (1994).

**Observation of Transition from Schottky Barrier to Thick Gap Device of ZnTe Surface Using Scanning Tunneling Spectroscopy**
R. J. Miles and T. C. McGill, to be published.

# Contents

# List of Figures

# List of Tables

# Chapter 1

# Introduction

## 1.1 Overview of Thesis

The work of this thesis primarily addresses two related questions. The first question concerns the detection of local variations in material quality and transport properties in semiconductor structures. The second question concerns how material growth can be controlled to minimize the adverse affects due to these inhomogenities. These questions are of particular technological relevance since the industrial pressures for higher packing densities, lower power requirements and faster speeds for semiconductor devices are driving the miniaturization of devices according to Moore's Law, that is, the exponential increase in the complexity of integrated circuits over time [1]. As miniaturization progresses, the electronic performance of devices will be no longer be determined by the weighted spatial average of its local properties. Instead the spatial variance of these properties will increasingly introduce more variance into performance across different devices[2].

The major results of the work are as follows. We have developed a hypothesis for the generation of $\{111\}$ stacking faults in nitrogen-doped ZnTe, a material used in green-blue light emitters. Through correlations with AFM and TEM micrographs, we identify particular surface morphologies with defects propagating from the substrate/ZnTe epilayer interface and from the doped ZnTe:N/ZnTe epilayer interface. By selective etching techniques we identify the defects starting at the substrate/ZnTe epilayer interface to be along the Te {111} planes while defects starting at the doped ZnTe:N/ZnTe epilayer interface tend to be along the Zn {111} planes. Reducing doping levels below $10^{19}$ $\mathrm{cm}^{-3}$ reduces defect formation and also their propagation. We also conclude that GaSb is preferred over a ZnTe substrate due to difficulties in oxide removal on the ZnTe substrate. Substrate surface roughness as measured by the AFM does not appear to play a significant role.

We have also advanced a technique to reduce surface roughness of Si/$CaF_2$/Si structures, a material with potential for semiconductor-on-insulator technology and quantum devices. Through low energy electron-beam irradiation of the surface of $CaF_2$ prior to Si growth, we show that we can increase the surface free energy of the $CaF_2$ and thus improve the crystalline quality of the subsequent Si layer. We also investigate the temperature dependence of the growth and find that irradiation causes a transition for amorphous growth to ordered growth of the Si layer.

We have also investigated the electrical characteristics of the cleaved ZnTe(110) surface using STM. We show that the surface obeys thermionic emission theory for very small tip-sample separations and that the surface's Fermi level is unpinned. As the separation increases, we observe an enhancement in the reverse bias current. We attribute this to an increase in tunneling transmission through the semiconductor space charge region that more than compensates for the decreased transmission through the gap region. We also show that the surface's Fermi level pins upon subsequent exposure to contaminates.

Finally, we have modified a STM inhouse to perform Ballistic Electron Emission Microscopy (BEEM), a technique to study buried interface properties. We have studied the surface and interface properties of Au/Si(100) to reproduce other researchers' results and then performed preliminary studies on the single barrier structure InAs/AlAs/GaAs. From spectroscopic data we determine roughly the energies for strong current onset and correlate these energies with the local band structure energies of the sample, particularly the Γ-points in the GaAs and AlAs.

The remainder of chapter 1 has been organized to give the reader motivation for the work as well as technical background for the methods utilized in this thesis. In section 1.2 we present motivation and historical background for the ZnTe and Si/$CaF_2$ studies. We will also discuss motivation behind the construction of the BEEM equipment along with the significance of investigating interface properties, particularly single barrier devices. We then feel it would be instructive to discuss the methods that have made up the bulk of the experimental work. This is because these techniques, Scanning Tunneling Microscopy (STM), Atomic Force Microscopy (AFM), and Ballistic Electron Emission Microscopy (BEEM), are relatively new to most researchers (the first STM was built in 1981 while the first BEEM was built in 1987). An introduction to STM will be give in section 1.3 followed by AFM in section 1.4. In both sections there will be an emphasis on experimental considerations and data collection artifacts. Theoretical approaches for STM tunneling calculations including the approach we use in chapter 4 can be found in Appendix A along with a discussion on AFM tip-sample interactions. BEEM will be briefly discussed in section 1.3 with the STM; a detailed discussion of BEEM technique along with equipment construction can be found in Appendix B.

## 1.2 Motivation for Investigations

### 1.2.1 ZnTe Studies and Light-Emitting Devices

The quality of electronic materials has intrinsic importance since it has a direct correlation with usefulness in device application. The ability to grow a huge array of homoepitaxial and heteroepitaxial structures has made great advances since the development of the technique of molecular beam epitaxy (MBE). This ability to grow epitaxial layers of one semiconductor on another with abrupt, high quality interfaces has resulted in a large variety of device application, some of which we will describe in the following sections. These structures also offer the opportunity to study basic physics phenomena such as hot carrier scattering or local band structure effects, both of which we will discuss later.

Devices that we have studied that is of particular technological interest are blue and blue-green light emitters. With the world wide LED market worth over a billion dollars, it may be surprising that an efficient blue LED is not commercially available[3]. One of the more promising material systems for these devices is the II-VI compounds since they have direct band gaps near the blue and blue-green energies. Our proposed device, a n CdSe/graded MgCdSe/p ZnTe junction, and devices proposed by other research groups that use a ZnSe-based material systems have a similar problem; the inability to form highly doped p-type regions in the ZnTe and ZnSe[11, 12, 13]. These highly doped regions are important for making ohmic contacts to the device and for reducing the voltage drop across the device due to high resistance layers.

Large bandgap II-VI materials have a history of doping problems[4]. Using conventional doping techniques (excluding metastable doping techniques which we will discuss below) binary II-VI compounds can be doped n-type or p-type but not both. Specifically, tellurides tend to be doped p-type, while the rest tend to be doped n-type. It is widely believed that the problem is not due to the lack of shallow dopants but due to a self-compensation mechanism (to be discussed in more detail in chapter 2) that becomes energetically favorable whenever dopants are introduced[4, 5]. Chadi et al., proposed that N would be the ideal p-type dopant to suppress the self-compensating effect. Shortly afterwards, Parks et al. reported hole concentrations of $3.4\text{x}10^{17}$ in ZnSe using a nitrogen plasma source [6]. Doping levels of $1\text{x}10^{18}$ and $1\text{x}10^{20}$ are currently reported for p-ZnSe and p-ZnTe, respectively.

However, cross-sectional TEM of these structures reveals an additional problem;

defects and stacking faults are easily generated at this substrate/epilayer interface and propagate through the device to the surface. These devices have typically contained a high density of defects and stacking faults ($10^6$ $cm^{-3}$) which we suspect is substantially reducing the injection and radiation efficiency of the device. The defects and faults propagating through the device can reduce injection efficiency or radiation efficiency through charging and/or trapping of carriers at defects and the defects can also act as nonradiative recombination centers[7]. We have investigated the source of these defects using TEM, AFM, and selective etching techniques. In order to reduce the defect density and the variability across devices to ensure reliable device operation and yield, one must also study the quality of the substrate and substrate surface. This is because the substrate effectively acts as a template for all subsequent growth layers and any suboptimal surface characteristics could possibly form into the observed device-killer defects. Using AFM and x-ray rocking curves we have investigated the effects of substrate quality on ZnTe:N epitaxial growth.

### 1.2.2 SOI and Quantum Devices in Silicon

The growth of semiconductors on epitaxial insulators (SOI) has a large number of applications and benefits. Initially, the advantage was radiation-hardness since the insulator isolated and limited the ionization damage by limiting the charge collecting region of the device. For integrated devices, SOI facilitates 3-D high density circuits since it isolates devices from each other and also reduces parasitic capacitance[8]. The Si/$CaF_2$/Si system is a natural choice for several reasons. First, Si substrates are highly desirable because of their low cost, large size, high quality, mechanical robustness, and well developed processing technology. $CaF_2$ is a logical choice for the insulator since it closely lattice matches Si, is stable at processing temperatures, has good chemical bonding at the interface, and has a large band gap and favorable band offsets to Si. In fact, $CaF_2$ also shows promise for the fabrication of quantum tunnel devices in Si-based systems. Quantum devices have recently gained much interest as a way to incorporate ultra dense memory, neural networks, and high speed electronics.

Although it has been shown that high quality epitaxial $CaF_2$ can be grown on Si(111) substrates[14], there exists a fundamental problem in realizing 3-D circuits. The problem is that even though $CaF_2$ easily wets the surface of Si, Si deposited on $CaF_2$ forms large islands that lead to amorphous growth[15]. This is because $CaF_2$ has a substantially lower surface free energy than Si (450 ergs/cm$^2$ for $CaF_2$ (111) verses 1240 ergs/cm$^2$ for Si(111)) and the surface strives for the lowest thermodynamic surface energy under equilibrium conditions[18]. In addition, the thermal expansion coefficients of Si and $CaF_2$ are dissimilar enough to produce strain and dislocations in the structure upon cooling. Many different methods have been tried to improve the crystalline quality of epitaxial Si/$CaF_2$, including varying growth temperatures, or predepositing Si at low temperatures on the $CaF_2$ and rapidly annealing[16, 17]. In an attempt to raise the surface free energy of $CaF_2$ to improve the subsequent growth of Si on top, we chose to study the effects of irradiating the surface of $CaF_2$ with low energy electrons. Low energy electrons have been shown in previous studies to desorb $F^+$ from $CaF_2$(111) and leave an ordered array of surface F-centers[9]. This array of F-centers will have a higher surface free energy than the $CaF_2$ surface and thus should favor 2D growth or at least lower the contact angle in 3D growth of Si on $CaF_2$.

### 1.2.3 BEEM and Inhomogeneous Subsurface Properties

One can divide problems associated with device miniaturization into two categories: those associated with single devices (intradevice) and those associated across devices (interdevice). We will ignore the rich field of interconnection problems. Much recent work has focused on intradevice difficulties. For example, from Carver Mead's calculations, a device's fundamental limit will be determined by the supression of parasitic currents such as oxide tunneling and junction-drain tunneling [19]. The following argument summaries the effect: as the feature size continues to shrink, the substrate doping must be increased to prevent punch-through. This increase in substrate doping will increase the junction electric field and thus increase junction-drain tunneling. To decrease this tunneling, the source voltage must be reduced which furthermore reduces the difference between the on and off current. This difference approaches KT below a feature size of about 0.03 microns.

Even though technology is not at these limits yet, there may be an even more fundamental limit. Lateral variation across a device may become a significant problem when the size of the device approaches the characteristic length of the spatial variance. The characteristic length is the length at which one could expect certain device characteristics to change significantly. It is when device dimensions are in this regime that the properties of one device can vary substantially from the properties of an adjacent device. When the characteristic length scale is larger than the single device limit, the fabrication of integrated devices might be limited to this longer length scale. To illustrate this point, consider a simple metal-GaAs Schottky contact. The electrical characteristics of a ohmic contact depends on the local proximity of discrete dopants to the metal-semiconductor interface. For a stochastic doping process in which the average doping levels in the semiconductor is $10^{19}$ $\text{cm}^{-3}$, a square device of length 400 angstroms will have contact resistances that vary from one device to another by a factor of two[2]. Hence, even though the individual device limit has not been reached, the interdevice fluctuations kill any chances of integrated device fabrication.

In order to investigate the local fluctuations across devices, we have constructed a Ballistic Electron Emission Microscopy (BEEM), a three contact modification of the STM (see figure 1.1). Where the STM simply biases the local probe (tip) and

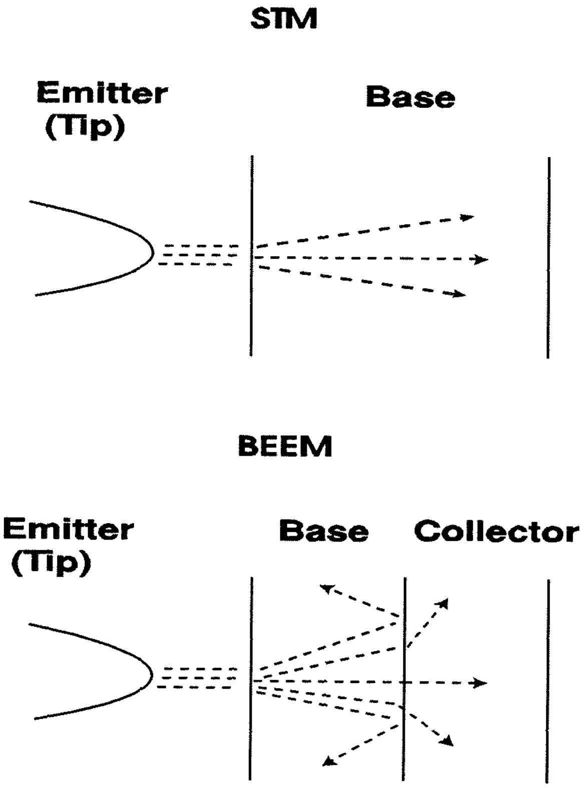

Figure 1.1: Basic BEEM experimental setup

measures the carriers that transverse between the tip and the sample surface, the BEEM measures both this current and the carriers that travel ballistically across a buried interface in the sample. Thus BEEM can give *simultaneously* both surface information and interface information.

To verify the operation of the BEEM instrumentation and to corroborate previous experiments, we investigated the Schottky barrier characteristics of Au deposited on Si(111). Using BEEM, we obtained a topographic map of the surface and of the underlying interface and, in addition, we performed spectroscopy at several different points on the surface. Using a simple theory developed by L. D. Bell et al., we were able to obtain an excellent fit to the spectroscopic data and extract Schottky barrier height information[20].

In addition we are the first to investigate the local surface and subsurface characteristics of a single barrier tunnel structure, Au/InAs/AlAs/GaAs(100). This system is of fundamental interest for several reasons. First, InAs/AlAs is a highly strained system for which we would hope to see defects due to interface relaxation since we have grown the InAs layer beyond the critical thickness length[23]. That is, we would hope to see evidence of lateral inhomogenities in the BEEM images that would not be correlated with the surface topography. Secondly, we hoped to see local band structure effects, that is, if the X-point, L-point, and Γ-point in AlAs and GaAs were observable in the spectroscopic data. In particular, if we do see the onset in L-point tunneling in spectroscopy, then we have direct evidence of the randomization or spreading of the carrier distribution in the base. The details behind the base carrier distribution are important not only in settling resolution issues for BEEM experiments but also in predicting current channels that are only available if certain criteria are met, such as conservation of the parallel momentum [21, 22, 24]. Spreading of the carriers in k space is necessary to observe L-point tunneling since the injected distribution from the tip is narrow in k space and preferentially in the (100) direction. This can be shown from WKB theory since the carriers in states with energy E relative to the unbiased Fermi level and with parallel wavevector $k_{||}$ will decay into the gap with an inverse decay length $\kappa = [(2m\phi/\hbar^2) - k_{||}{}^2)]^{1/2}$ where $\phi = [(\phi_t + \phi_b)/2 - E + (eV/2)]$ is the average barrier height between the emitter and the base workfunctions, $\phi_t$ and $\phi_b$ respectively, and V is the applied bias. Hence states with larger $k_{||}$ will have a shorter decay length and thus states with $k_{||} \sim 0$ will dominate the tunneling current into the base. However, for these same carriers to access L-point states, they must have a substantial $k_{||}$ component, indicating that the carriers must have scattered elastically while propagating through the base. In the experiments we do see evidence of $\Gamma$ and possibly X-point tunneling, indicating not only local band structure effects. We do not see conclusive evidence of L-point tunneling.

## 1.3 Fundamentals of Scanning Tunneling Microscopy

### 1.3.1 Background and Basics

This section is designed to provide the reader with a technical background for the work involving scanning tunneling microscopy. The additional complications of BEEM, a modification to the STM, will be discussed in a later chapter and in Appendix B. Since both of these techniques are related and relatively new, we will first give a basic overview of the construction and operation of the STM before we delve into the details and concerns for the systems we are particularly interested in. More specifically, we will focus on metal-gap-semiconductor tunneling for the STM experiments.

STM has developed rapidly into a unique and flexible surface analysis technique. Although several "microscopes" had been developed previous to the STM to analyze surfaces, each one had strict limitations [27] [34] [32]. For example, the resolution of the high resolution optical microscope (HM), phase contrast microscopy (PCM), and scanning electron microscope (SEM) were inadequate for resolving

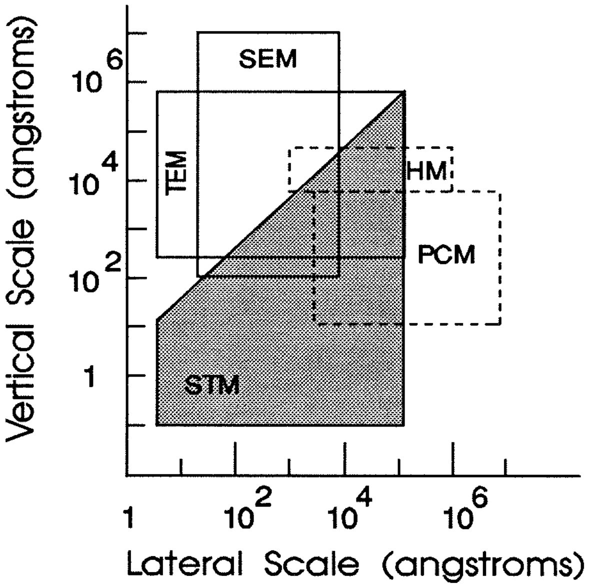

Figure 1.2: Comparison of the range of resolutions of the STM and other microscopes

individual atoms. High-resolution transmission electron microscopy (TEM), used mainly to image bulk or interface regions, must be used only on specially thinned samples. The field emission microscope (FEM) and the field ion microscope (FIM) image the surface of sharp tips with radius < 1000 Å. Scattering experiments such as low energy electron diffraction (LEED), x-ray, He diffraction, or ion scattering yield only limited reciprocal space information. However, as seen in figure 1.2, only STM offers nondestructive, real-space imaging with atomic resolution. In addition, it also allows one to probe local transport properties both on and below the surface (BEEM). This is possible because the displacement of the probe can be controlled with subangstrom precision. Figure 1.3 illustrates through a simple diagram the basic construction that allows such fine control[53].

In a typical STM experiment, a bias is applied across the tip and sample which are typically separated 5-20 Å, causing carriers to tunnel across the gap. The tunneling probability, from simple WKB theory, is proportional to $e^{-A\bar{\phi}^{1/2}s}$, where

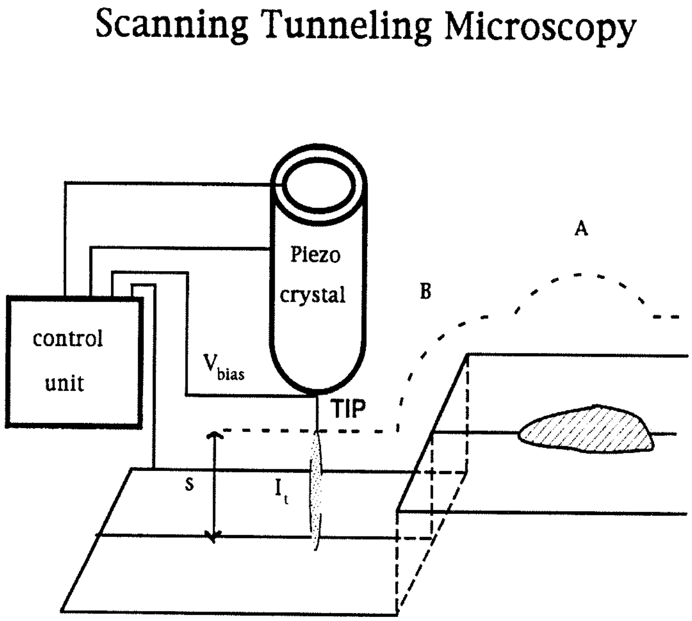

Scanning Tunneling Microscopy

Figure 1.3: Basic STM experiment

$A = 1.025\ \mathrm{eV}^{-1/2}\text{Å}^{-1}$, $\bar{\phi}$ is the average barrier height, and s is the tip-sample separation. Since the average barrier height is about 4 eV, the tunneling probability changes by roughly an order of magnitude for a 1 Å change in s[28]. This large change in signal for small change in separation allows tip-sample separation to be controlled vis-a-vis a feedback circuit within 0.1 Å.

For the work involved in this thesis, we have used the STM in two modes, the constant current mode and the spectroscopy mode. In the constant current mode, the tip is scanned over the the surface by rastering the voltage to a set of piezocrystals that the tip is mounted on. A feedback circuit measures the tunneling current and compares it to a preselected setpoint current. The difference becomes the error signal which is then used for two purposes. First it is used to generate a correcting voltage for the piezos to change the tip height and reduce the error signal. Secondly, the error signal is used to generate a topographic map of the surface. For spectroscopy measurements, the tip is held stationary over the sample and the bias voltage is ramped over a preselected range while the current is recorded.

### 1.3.2 Experimental Artifacts

Before interpreting the data acquired in the constant current mode as a topographic map of the surface, there are several sources of artifacts that one must be aware of. We define an artifact as a measurement that results in an image feature different from the actual surface feature. The sources of these artifacts can be separated into four categories; tip-related, piezo-related, electromechanical-related, and sample-related. We will discuss all four sources but postpone the a theoretical treatment of tunneling until Appendix A.

The tip is arguably the most crucial component of an STM or BEEM experiment. This is because any information that is gathered is a convolution of the tip and the sample characteristics. The tip must be well characterized to be useful experimentally. The characteristics include tip shape and stability, electrical properties, and mechanical characteristics. A well characterized tip shape means that tunneling occurs at only one localized region on the tip (no multiple tips), and that this region does not change during data acquisition. We use PtIr (80% and 20%, respectively) tips purchased commercially that are electrochemically etched, ion milled, and characterized by SEM to have an effective radius less than 500 Å, modeling the tip's end as a sphere[29]. PtIr's stiffness provides mechanical stability and its inertness prevents tip modification due to contamination under non-UHV conditions. We have also used gold tips but have found they are inferior due to their malleability and lack of mechanical stability. In addition, the tip should have a well-defined workfunction and simple band structure (i.e., metal) so that theoretical comparisons with actual data are not unnecessarily complicated.

The effective radius of the tip is very important for both the constant current mode and the spectroscopy mode. For measuring abrupt surface features such as steps or trenches, the smaller the tip radius, the greater the resolution of the

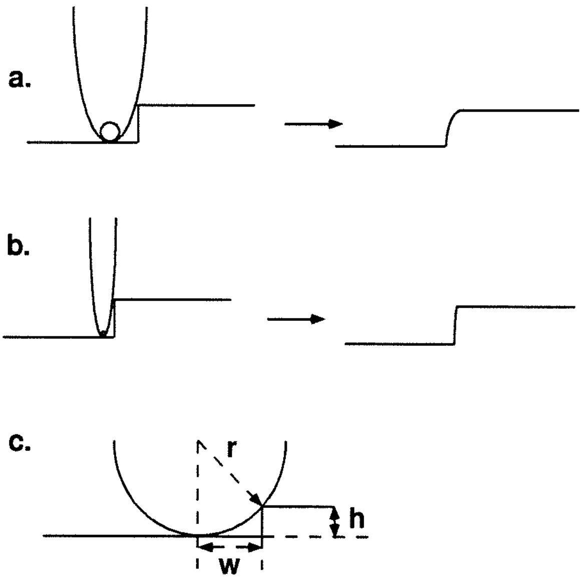

Figure 1.4: The effect of tip shape and aspect ratio on surface morphology

feature. This effect is illustrated in (a) and (b) of figure 1.4. The small circle at the end of the tip represents the effective radius model. One can roughly estimate the effective radius of the tip if one knows the true size of a surface feature, such as an atomic step[30]. For a single atomic step shown (c) of figure 1.4, one can easily derive the relationship $r = W^2/2h + h/2$. For AFM tips r is approximately the radius of the tip neglecting tip-surface interactions while r is actually the tip radius plus the tunneling gap distance for the STM tip. While we have neglected many factors in this gross simplification, it is still useful in obtaining a rough estimate of the tip's size. For example, we have measured atomic steps on graphite and ZnTe and have found that mechanically cut PtIr tip radii vary from 20 to several hundred Å, while the well characterized tip previously described vary from 50 to 200 Å. Tips can be made duller by rapidly raising the current to microamps, which has been speculated to locally "melt" the tip at the end[31].

Although sharp tips are necessary for detecting abrupt surface features, for spectroscopic measurements a duller tip (i.e., larger tip radius) is more desirable for several reasons. One reason is because a larger tip ($>$ 500 Å) yields more stable spectroscopic data since it averages over a larger area than a small tip. This averaging effect reduces the influence of tip drift, that is, an uncontrollable movement between the tip and the sample surface that is caused by temperature differences between the tip holder and the sample holder or by piezo creep (to be discussed later). Ideally, one should be able to eliminate the drift by simply waiting several hours or days until equilibrium is reached. However since our experiments are not performed in UHV, we are slowly contaminating the surface and thus are under a time constraint. More crucial than the averaging effect is the fact that a larger tip has better energy resolution than a sharper tip[31, 32]. Lets assume that a sharp tip has a effective radius of 3 Å and a dull tip has a radius of 800 Å (this is about the tip size we used to take spectroscopy data by our estimations). We can roughly relate the lateral resolution ($\Delta x$) to the tip radius (R) and the tunneling gap (d) by $\Delta x = [2\mathring{A}(R + d)]^{1/2}$[40]. If we assume a tunneling gap of 5 Å, the uncertainty relationship $\Delta k \Delta x \approx 1$ indicates that a sharp tip and a dull tip will have a momentum uncertainty of 0.25 Å$^{-1}$ and 0.025 Å$^{-1}$, respectively (Although the crystal momentum in a solid is not a physical momentum, a resolution limit can be estimated). Figure 1.5 shows the band structure of a nearly free electron dispersion for k = 1 Å$^{-1}$ with the spread of uncertainty for a dull and a sharp tip at a probing energy $V_a$. The curves for the dull and sharp tip are displaced from the dispersion curve for clarity. Note that for a single atom tip the spread in energy can be considerable.

The piezoelectric crystals that control the tip movement can also cause artifacts in image interpretation. There are three phenomena that are the main culprits; piezo non-linearity, hysteresis, and creep[33]. Non-linearity refers to a non-linear mechanical distortion of the piezo with a linear change in applied voltage. Hysteresis is a type of time-dependent non-linearity in which the response of the mechanical deformation of the ceramic lags that which is expected based on the applied voltage. Creep is the phenomena in which the piezo continues to

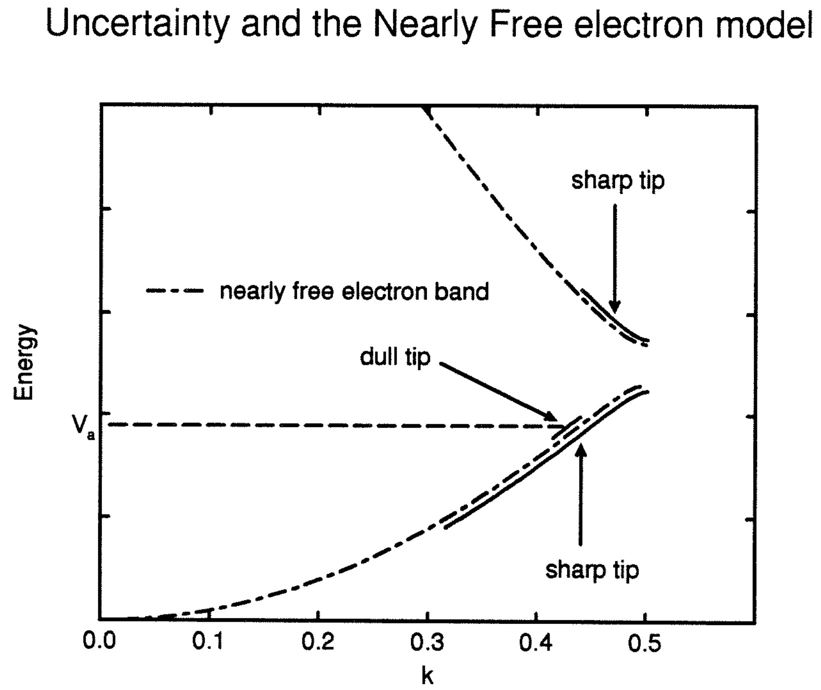

Figure 1.5: Nearly free electron model for a dull and sharp tip

deform after a rapid change in voltage. Creep and hystesis can both be minimized by operating the piezos at low electric fields. This amounts to maintaining the mean piezo voltage around zero during scanning. In addition, a rapid increase in voltage, possibly caused by scanning over an abrupt feature, may produce an overshoot and subsequent ripples in the piezo mechanical deformation, as the piezo and the electronics "hunt" for the correct tip height.

We attempt to mitigate the non-linearity effects by calibrating the piezos prior to and after each experiment. To calibrate, we use commercially available samples that have a Ir surface and well characterized step heights, widths, and pitches and scan the calibration sample at the same frequency and range at which we expect to perform the experiment. We compare the known dimensions of the calibration sample to the measured ones and adjust a set of parameters that determines the waveform of the piezo's applied voltage. The waveform consists of a linear term and a decaying exponential of varying magnitude and time scale. We then rescan to ensure that the recorded image is within the uncertainty of the calibration sample.

Electromechanical factors include vibration isolation and feedback oscillation[33, 34]. Exponential dependence of the tunneling current on gap distance makes vibration isolation an extremely sensitive factor. We mount the entire STM on Si gel pads and bunge cords to ensure sufficient isolation from mechanical vibration, particularly low frequency oscillations near 1 Hz. In addition, the feedback circuit can produce electronic oscillations in the images[34]. For example, a large amount of gain is desirable since the tip responses to the surface more readily. However, gain causes a phase shift in the normally negative feedback circuit that may change to positive feedback for the closed loop response if it is set high enough. The onset of this phenomena shows up as oscillations in the image that rapidly grow with increased gain. The solution is to keep the gain just below this point and to adjust the gain as conditions change.

Last of all, surface conditions and bulk characteristics can lead to image artifacts that do not reflect the true surface morphology. First, the surface must be sufficiently conductive to ensure the current characteristics are not dominated by the back contact to the sample or by the spreading resistance[35]. The back contact should have a negligible resistance compared to the effective tunneling resistance, a feat that is usually straightforward to engineer. Spreading resistance ($R_s$), the resistance carriers experience when they pass through a small orifice and "spread" spacially on the other side, is more difficult to control. Since tunneling occurs at the very end of the tip, which may only comprise of a few atoms, this resistance can be modeled as a small orifice that the carriers must pass through. The effects of spreading resistance can be divided into two region; the high Knudsen and low Knudsen limit where the Knudsen factor is $K = l/a$ where l and a represent the inelastic mean free path and the orifice radius, respectively[36, 37]. In the low Knudsen limit the spreading resistance, first solved by Maxwell[38], is expressed as $R_s = \rho/2a$ where $\rho$ is the resistivity of the sample. In the high Knudsen limit the spreading resistance depends on the ratio of the inelastic mean free path to

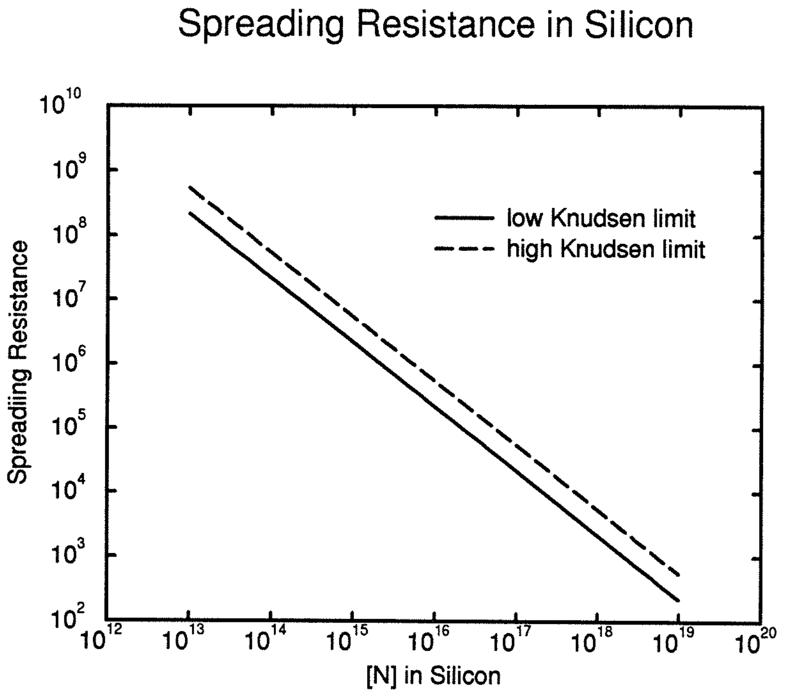

Figure 1.6: Spreading resistance in Si

the orifice radius and can be expressed as $R_s = (\rho K)/4a$ [39]. The orifice effect is stronger in the high Knudsen limit since the carriers must travel ballistically through the orifice. For STM or BEEM experiments, the tip (orifice) radius may realistically be between 10 - 1000 Å. Since the inelastic mean free path is on the order of hundreds of angstroms, we are not clearly in either limiting case. Figure 1.6 shows the dependence of the spreading resistance on resistivity for a 10 Å tip radius for both the high and low Knudsen limit for electrons in Si. Typically in STM the bias voltage is 1 volt and the demand current is 1 nA, so $R_s < 10M\Omega$ adds a voltage of less than 10 mV, a negligible effect. For Si, with a doping level below 1 x $10^{15}$ $\mathrm{cm}^{-3}$, $R_s$ may become comparable to the tunneling resistance and cause the tip to crash into the surface. To prevent problems related to conductivity and spreading resistance, we choose samples for which we can readily make ohmic contacts and which are doped to greater than 1 x $10^{17}$ to reduce any spreading resistance effects.

Second, the sample must be prepared so as to eliminate excessive surface contamination and roughness. Of course certain types of surface contamination may be desirable to study experimentally. However, if the contamination is several monolayers thick and is either physabsorbed onto the surface or conducts poorly, the tip will be continously modified through interactions with the surface and the data will be unstable. Likewise, if the sample surface is too rough, the finite response time of the feedback circuit will cause the tip to contact surface features, thus modifying the tip and the surface. To mitigate problems we may encounter with rough surfaces or excessive surface contamination, we cleave or etch a fresh surface just prior to experiments, which are performed in a custom built Vacuum Atmosphere's Glove Box with 0.3 $\mu$m filters and filled with an inert argon atmosphere. The unit also contains an alumina molecular sleeve to remove moisture and carbon dioxide, an alumina filter to remove oxygen, and a cold trap which removes any condensible gases and hydrocarbons. The oxygen content is maintained to less than one ppm and the moisture content is maintained to less than 10ppb. Thus we can observe a relatively clean surface for several hours prior to oxygen or moisture contamination.

## 1.4 Fundamentals of Atomic Force Microscopy

### 1.4.1 Background and Basics

Atomic Force Microscopy is a modification of STM in which the sensing mechanism is the physical deflection of the probe as it moves across the surface[54]. Figure 2.2 shows the basic AFM setup that we use. The sample is mounted on a piezo tube which scans the surface underneath the cantilever or tip. Features on the surface cause the cantilever to deflect. The optical detection system consists of a diode laser, several mirrors, and a pair of photodiodes which sense the movement of the cantilever. The laser diode's beam reflects off the back of the cantilever onto the

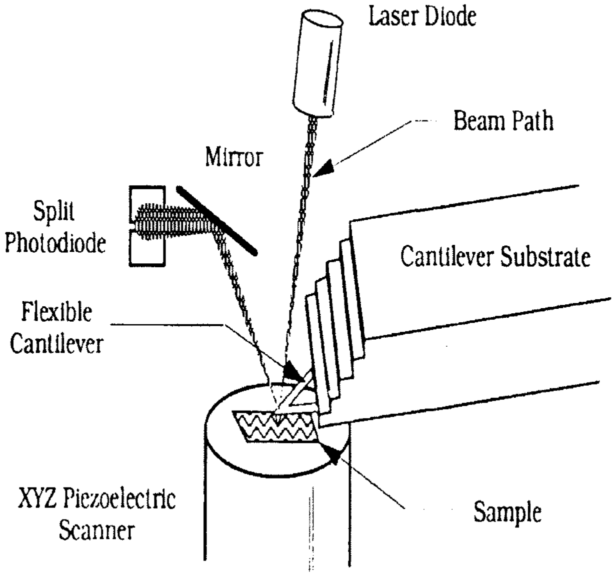

Figure 1.7: Basic AFM experiment

photodiodes. As the cantilever moves vertically, the beam is deflected more into one photodiode and less into the other. This differential signal is compared to a reference voltage to produce an error signal which is used as negative feedback to reposition the piezo height to keep the deflection constant, similar in operation of the STM constant current mode. The piezo height relates directly to the surface topography. Because only the deflection of the cantilever is necessary for sensing, nonconductive as well as conductive surfaces can be examined.

The AFM is generally used in either the constant force mode or the variable force mode. The operation described above is the constant force mode since the deflection and hence the force (for a homogeneous surface) is kept constant. In the variable force mode, the piezos are not under feedback control and the cantilever is free to deflect in response to surface features. This mode improves the response of the AFM to small surface features but has a limited dynamic range. In addition, operation in this mode may lead to excessive tip-surface interactions if the surface

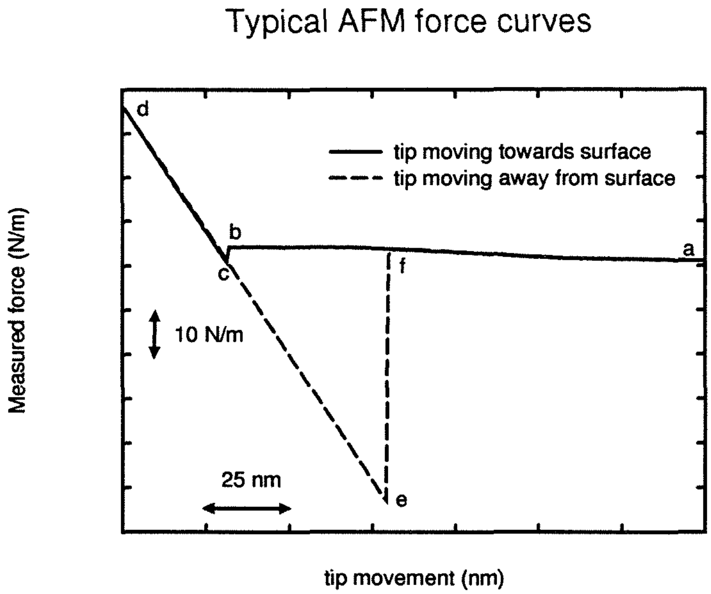

Figure 1.8: Typical AFM force curve

is too rough. For our experiments, we operate in the constant force mode but also measure the variable force or deflection signal as well. The deflection signal represents the change in the error signal and hence directly reflects the derivative of the surface topography.

In addition, the AFM can indirectly measure the force as a function of tip-sample separation. These measurements generate what is commonly referred to as force curves, shown in figure 1.8. Region a-b denotes the approach of the tip to the surface prior to any interaction. Along b-c the tip is attracted to the surface by a thin layer of liquid that usually forms on the surface. From the force curve we see that the layer is about 1 nm thick. Along the line c-d the tip is in contact with the surface and its slope is a measure of the system's effective spring constant. Since the movement of the tip along c-d is the same in both directions, the interaction with the surface in elastic. An inelastic interaction with the surface appears as a hystersis along line c-d. As the tip retracts from the surface it approaches point e, the point of greatest adhesion. The tip eventually pulls away from the surface and moves along line f-a. The deflection of the tip can be converted into a force by $F_{measured} = k_t \Delta z$, where $k_t$ is the tip's spring constant and $\Delta z$ is the tip movement.

For experiments performed in air, a layer of water several nanometers thick forms on the surface. This layer abruptly attracts the tip as it approaches and leaves the surface thus leading to instabilities, as seen in figure 1.8[55]. It should be noted that the true force exerted on the surface is unknown since the complexities of the tip-surface interaction are unknown. We give a brief overview of the vast array of tip-surface interactions that are possible along with their characteristics in the Appendix A. What force measurements do provide is a relative comparison of the tip-surface interactions provided that the tip remains unmodified. When quantitatively comparing surfaces of different samples it is important to know if the tip-surface interaction is substantially different since this strongly influences how accurately the image reflects the true surface.

### 1.4.2 Experimental Artifacts

Since the AFM has many similarities to the STM, both techniques share certain experimental artifacts. These include artifacts associated with the piezoelectric crystals and also electromechanical artifacts. The tip-sample interactions comprise the remaining source of artifacts. In AFM, one can show that the data is actually a convolution of the elasticity of the tip and surface. Through a simple model we will derive the relationship for both the variable force and the constant force modes. (see figure 1.9)[56].

In this simple model, the tip and tip-surface interaction are modeled as springs with spring constants $\mathrm{k}_t$ and $\mathrm{k}_s$, respectively (see figure 1.9)[56]. We assume that $k_t$ is constant and $k_s$ is dependent on the applied force. We will initially assume we are scanning over a surface in the variable force mode so that there is no feedback to adjust the tip height, and thus $k_{s1}$ is different from $k_{s2}$. Since the forces must add to zero, $k_t \Delta z = k_{s2}(\Delta h - \Delta z)$.

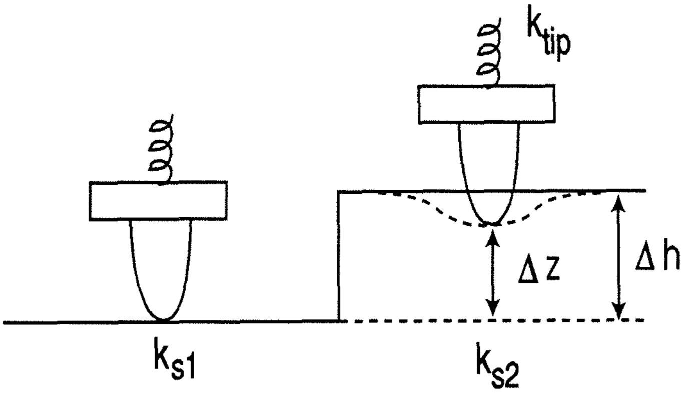

Figure 1.9: Simple model of tip-surface interaction

We can express this slightly differently as

$$\Delta z = \frac{k_{s2}}{(k_{s2}+k_t)}\Delta h. \tag{1.1}$$

As previously mentioned, the measured force is $k_t\Delta z = [\frac{k_{s2}k_t}{k_{s2}+k_t}]\Delta h$. Thus in the variable force mode, if $k_t << k_{s2}$ the deflection of the tip is approximately the feature height. An alternative viewpoint is, instead of scanning the tip across a feature, one can advance the piezo $\Delta h$ toward the surface, as when measuring a force curve. Thus the term in the brackets is the measured slope, $k_m$, of the force curve and reflects the convolution of the tip and surface stiffness.

From $k_m$ one can explain the tip instabilities in figure 1.8. When the tip initially touches the fluid on the surface, a meniscus forms causing an attractive force. This attractive force means $k_s$ is negative. Thus when the attractive force is large enough so that $k_t = -k_s$, $k_m$ and the force become infinite and the tip becomes unstable until it contacts the surface.

In the constant force mode, we can also see how the measured feature height depends on the force curve. In figure 1.10, we start with a set force, $k_{s1}z_o$, and scan over the surface feature to where the interaction is $k_{s2}$. The feedback circuit will adjust the tip height until the force reduces to $k_{s1}z_o$. However, there will

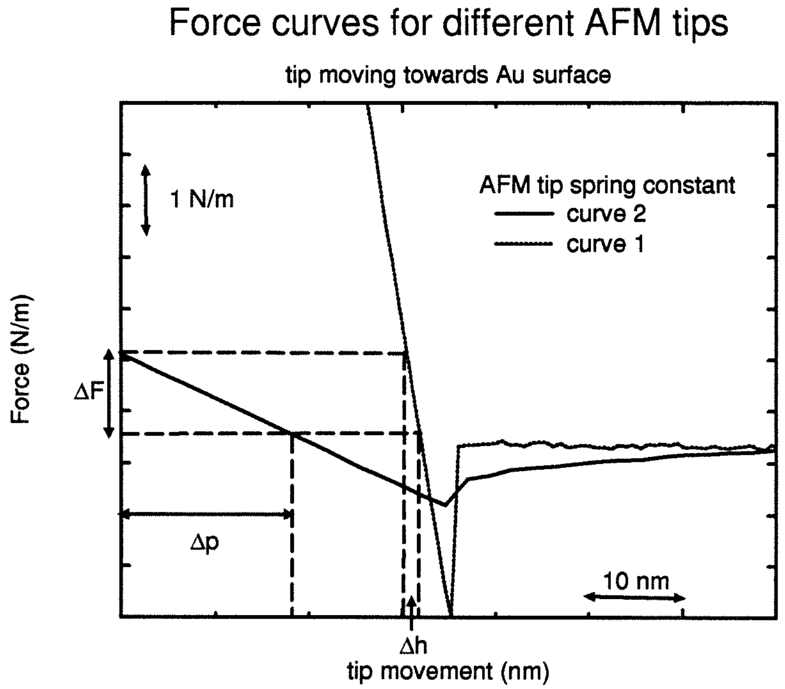

Figure 1.10: Force curves for tip with large and small tip spring constant

be a temporary deflection of the tip prior to this adjustment which results in a temporary movement up the force curve, $\Delta F$ [57]. Figure 1.10 illustrates the consequences of this excursion. Curve 1, called the true force curve, represents a force curve where $k_t >> k_s$. The slope of this curve upon contact is approximately $k_s$ and any movement of the piezos and tip reflect the true surface height. Curve 2 represents the convoluted force curve and has slope $\frac{k_{s2}k_t}{k_{s2}+k_t}$ upon contact with the tip. For a given change in force, $\Delta F$, the corresponding movement in the piezos is $\Delta h$, the true surface height, for curve 1 and $\Delta p$ for curve 2. From the slopes of these curves, one can relate $\Delta h$ and $\Delta p$ as

$$\Delta F = \frac{k_t k_s}{k_t + k_s}\Delta p = k_s \Delta h, \tag{1.2}$$

$$\Delta p = [(k_t + k_s)/k_t]\Delta h. \tag{1.3}$$

Thus for positive (negative) tip-surface interactions, the measured feature, $\Delta p$, is much larger (smaller) than the actual feature size, $\Delta h$. From equation 1.3, we see that if $k_t >> k_s$ then $\Delta p \approx \Delta h$. To minimize $k_s$, we use as small a force as possible while still maintaining tip stability. By having tips of various thicknesses and lengths, we can select the maximum $\mathrm{k}_t$ (within a range of 0.06 to 0.58 N/m) that does not modify the surface. Tips with large $\mathrm{k}_t$, while producing images that more closely match the actual surface (without tip convolution), tend to "dig up" soft surface features.

If one is looking at surfaces that are inhomogeneous, the above arguments imply that the force curve should be known at each image point in order to properly interpret image features. We do measure force curves when we encounter abrupt features of interest on the surface. As a manner of procedure we investigate one or two similar surface features and assume that the rest behave likewise.

## 1.5 Outline of Thesis

The remainder of the thesis is organized as follows. Chapter 2 will address the material properties of nitrogen doped ZnTe grown by MBE on both ZnTe and GaSb substrates. First a systematic comparison of the substrates will be made after each processing step using AFM. Second, the crystal quality of the epilayer will be analyzed by TEM and AFM, and a direct correlation is shown between the two. Finally, a model will be proposed that explains the formation of the defects following the theoretical work of Chadi et al.

In chapter 3 Si grown on $CaF_2$/Si using electron-beam-assisted MBE will be studied as a function of substrate temperature and electron beam dosage using AFM, TEM, and XPS. At normal growth temperatures the Si surface will be shown to form hexagons as predicted by Waldroff reconstructions. We will also show that a distinct minimum in surface roughness as a function of electron dosage exists. We discuss several possible thermodynamic and kinematic explanations for the minimum including the formation of surface F-centers and nucleation sites by florine desorption. At low temperatures we also see a transition from amorphous to ordered growth as a function of electron dosage.

We present surface images and spectroscopy of cleaved ZnTe using the STM in chapter 4. We examine the spectroscopy in detail and show that the reverse bias current increases in magnitude as the tip is withdrawn for the surface over a certain range. We confirmed this effect in the I vs s measurements, where s is the tip-sample separation. We model the system using a model similar to Duke's independent electron tunneling model with an unpinned semiconductor surface and show that the observed effect is consistent with theoretical predictions. We also present data that suggests that contaminates pin the surface Fermi level near midgap.

Chapter 5 discusses the subsurface investigations of Au/Si and InAs/AlAs/GaAs systems using BEEM and conventional iv measurements. For Au/Si, we confirm previous investigator's conclusions of the lateral inhomogenities of the Au/Si interface and the measured barrier height. We discuss the current theoretical issues surrounding BEEM and attempt to test the "searchlight" effect through the data. In the InAs/AlAs/GaAs system we present BEEM spectroscopy that demonstrates the onset of Γ-point and possibly X-point tunneling through the AlAs into GaAs. We present evidence through frequency plots that the quadratic onset of the collector current represents the band edges for the transport of carriers into the GaAs substrate.

# Bibliography

[1] R. K. Watts, *Submicron Integrated Circuits* (John Wiley and Sons, New York, 1989).

[2] W. Boudville, Ph.D. Thesis, California Institute of Technology, 1988.

[3] M. Phillips, Ph.D. Thesis, California Institute of Technology, 1993.

[4] J. O. McCaldin, *J. Vac Sci. Technol. A* **8**, 1188 (1990).

[5] D. J. Chadi, *Appl. Phys. Lett.* **59**, 3589 (1991).

[6] R. M. Parks, M. B. Troffer, C. M. Rouleau, J. M. DePuydt, and M. A. Haase, *Appl. Phys. Lett.* **57**, 2127 (1990).

[7] S.Guha, J. M. DePuydt, M. A. Haase, J. Qiu, and H. Cheng, *Appl. Phys. Lett.* **63**, 3107 (1993).

[8] S. M. Sze, *VLSI Technology* (McGraw-Hill, New York, 1988) p. 366.

[9] K. Miura, K. Sugiura, and H. Sugiura, *Surface Science Letters* **253**, 1407 (1991).

[10] W. J. Kaiser and L. D. Bell, *Physical Review Letters* **60**, 1406 (1988).

[11] M. C. Phillips, J. F. Swenberg. M. W. Wang, J. O. McCaldin, and T. C. McGill, *Physica B* **185**, 485 (1993).

[12] M. C. Phillips, M. W. Wang, J. F. Swenberg, J. O. McCaldin, and T. C. McGill, *Appl. Phys. Lett* **61**, 1962 (1992).

[13] Y. Fan, J. Han, J. Sarave, R. C. Gunshor, M. M. Hagerott, and A. V. Nurmikko, *Appl. Phys. Lett* **63**, 1812 (1993).

[14] L. J. Schowalter, R. W. Fathauer, R. P. Goehner, L. G. Turner, R. W. DeBlois, S. Hashimoto, J.-L. Peng, W. M. Gibson, and J. P. Krusius, *J. Appl. Phys.* **58**, 302 (1985).

[15] L. J. Schowalter and R. W. Fathauer, *CRC Reviews of Solid State Materials Sciences* **15**, 367 (1989).

[16] T. Asano and H. Ishiwara, *Appl. Phys. Lett.* **3**,68 (1982).

[17] R. W. Fathauer, N. Lewis, E. L. Hall, and L. J. Schowalter, *J. Appl. Phys.* **60**, 3886 (1986).

[18] J. J. Gillman, *J. Appl. Phys.* **31**, 2208 (1960).

[19] C. Mead, *Scaling of MOS Technology to Submicrometer Feature Sizes*, Colloquium at Caltech, Pasadena, California (1993).

[20] L. D. Bell and W. J. Kaiser, *Phys. Review Lett.* **61**, 2368 (1988).

[21] A. M. Milliken, S. J. Manion, W. J. Kaiser, L. D. Bell, and M. H. Hecht, *Phys. Review Lett.* **46**, 12826 (1992).

[22] E. Y. Lee, B. R. Turner, J. R. Jimenez, and L. J. Schowalter, *J. Vac. Sci. Technol. B* **11**, 1579 (1993).

[23] A. E. Fowell, A. A. Cafolla, B. E. Richardson, T. H. Shen, M. Elliot, D. I. Westwood, and R. H. Williams, *Appl. Surface Science* **56**, 622 (1992).

[24] H. D. Hallen, A. Fernandez, T. Huang, J. Silcox, and R. A. Buhrman, *Phys. Review B* **48**, 5712 (1993).

[25] M. Kleefstra and G. C. Herman, *J. Appl. Phys.* **51**, 4923 (1980).

[26] E. H. Rhoderick and R. H. Williams, *Metal-Semiconductor Contacts* (Oxford Science Publications, Oxford, 1988) p. 136.

[27] J. M. Walls, *Methods of Surface Analysis* (Cambridge University Press, New York, 1989).

[28] G. Binning and Rohrer, *Helv. Phys. Acta.* **55**, 726 (1982).

[29] G. Binning and Rohrer, *IBM J. Res Develop* **30**, 355 (1986).

[30] Materials Analytic Services, Raleigh, North Carolina, 27607.

[31] L. Montelius and J. O. Tegenfeldt, *Appl Phys. Lett.* **62**, 2628 (1993).

[32] R. M. Feenstra, private communication.

[33] Y. Kuk and P. J. Silverman, *Rev. Sci. Instrum.* **60**, 165 (1989).

[34] D. W. Pohl, *IBM J. Res. Develop* **30**, 417 (1986).

[35] T. Tiedje and A. Brown, *J. Appl. Phys.* **68**, 649 (1990).

[36] M. B. Johnson and J. M. Halbout, *J. Vac Sci. Technol. B* **10**, 508 (1992).

[37] A. G. M. Jansen, F. M. Mueller, and P.Wyder, *Science* **199**, 1037 (1978).

[38] G. Wexler, *Proc. Phys. Soc. London* **89**, 927 (1966).

[39] J. C. Maxwell, *A Treatise on Electricity and Magnetism* (Clarendon, Oxford, 1904).

[40] Y. V. Sharvin, *Zh. Eksp. Teor. Fiz.* **48**, 984 (1965).

[41] J. Tersoff and D. R. Hamann, *Phys. Rev. Lett.* **50**, 1998 (1983).

[42] J. Bardeen, *Phys. Rev. Lett.* **6**, 57 (1961).

[43] M. S. Chung, T. E. Feuchtwang, and P. H. Culter, *Surface Science* **187**, 559 (1987).

[44] N. D. Lang, *Phys. Rev. Lett.* **56**, 1164 (1986).

[45] J. Tersoff, *Scanning Tunneling Microscopy and Related Methods* (Kluwer Academic Publishers, 1990) p. 77.

[46] R. M. Feenstra, J. A. Stroscio, J. Tersoff, and A. P. Fein, *Phys. Rev. Lett.* **58**, 1192 (1987).

[47] Z. H. Huang, M. Weimer, and R. E. Allen, *J. Vac. Sci. Technol. B* **9**, 2399 (1991).

[48] C. B. Duke, *Tunneling in Solids* (Academic Press, New York, 1969) p. 30.

[49] M. Weimer, J. Kramar, J. D. Baldeschwieler, *Phys. Rev. B* **39**, 5572 (1989).

[50] R. M. Feenstra and J. A. Stroscio, *J. Vac. Sci. Technol. B* **5**, 923 (1987).

[51] E. H. Rhoderick and R. H. Williams, *Metal-Semiconductor Contacts* (Oxford Science Publications, Oxford, 1988) p. 16.

[52] D. Z. Ting, E. T. Yu, and T. C. McGill, *Appl. Phys. Lett* **58**, 292 (1991).

[53] H. Heinzelmann, E. Meyer, H. Rubin, and H. J. Gunterrodt *Force Microscopy* (Kluwer Academic Publishers, Boston, 1989) pp. 450.

[54] G. Binning and C. F. Quate, *Phys. Rev. Lett.* **56**, 930 (1986).

[55] I. N. Sneddon *Int. J. Eng. Sci.* **3**, 47 (1965).

[56] N. A. Burnham and R. J. Colton, *J. Vac. Sci. Technol. A* **9**, 2548 (1991).

[57] N. A. Burnham, *Appl. Phys. Lett.* **63**, 114 (1993).

[58] D. R. Baselt and J. D. Baldeschwieler, *J. Vac. Sci. Technol. B* **10**,2316 (1992).

# Chapter 2

# The Growth of ZnTe:N on GaSb and ZnTe substrates

## 2.1 Introduction

The technological and economical importance of solid state blue and blue/green leds and lasers cannot be overstated. Among the many benefits from the reduction in wavelength are improvements in printer technology (from increased resolution and photoconductivity), a four-fold increase in data storage, and access to full color displays. Consequently, the recent success of fabricating these devices using II-VI materials has led to intensified efforts to solve the remaining dopant and contact problems preventing widespread use.

Recently, nitrogen doping has offered a partial solution to the doping and contact problems of ZnSe and ZnTe for the fabrication of II-VI blue light emitters [6, 2, 3, 4]. While the doping level in p-ZnSe is still too low for an adequate ohmic contact to be made, nitrogen-doped ZnTe offers a solution since it readily forms an ohmic contact to gold and can be graded with ZnSe [2]. In addition, ZnTe:N can serve as a basis for other light emitting devices [4]. However, to date there has been little progress on the understanding of the doping process or its

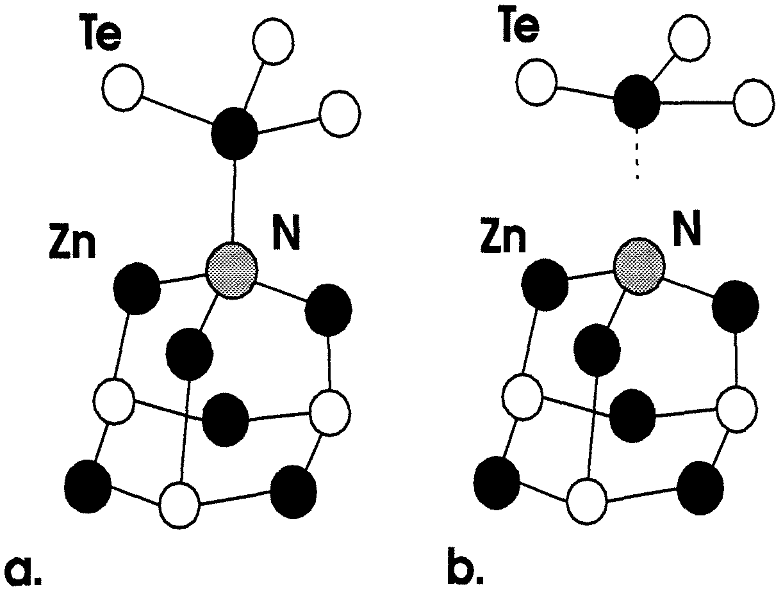

Figure 2.1: Model for 4-fold and 3-fold coordination of N in ZnTe

effect on crystal growth and quality. It is the purpose of this chapter to study the effect of nitrogen doping of ZnTe on crystal quality.

Crystal quality is especially important for light emitting devices because defects and dislocations can act as potential nonradiative recombination centers and can also increase electrical resistivity, therefore significantly degrading device performance. Unfortunately, nitrogen, a substitional acceptor for Te in ZnTe, is likely to promote defect and dislocation generation for several reasons.

According to Chadi et al., the uncompensated neutral nitrogen atom can transform into either a three-fold or four-fold coordinated state (see figure 2.1) [5]. It is energetically favorable for the neutral acceptor to undergo the following reaction:

$$2a^0 \rightarrow a^- + A^+, \tag{2.1}$$

where $a^-$ and $a^0$ are the negatively and neutrally charged four-fold coordinated state, respectively, and $A^+$ is the three-fold coordinated state with two holes bound to it. Thus about half the acceptors eventually become stable three-coordinated sites with a broken Zn bond. This broken bond can act as a source for extended dislocations. In addition, the bonds formed in either state will be significantly shorter since the neutral nitrogen atom is about 42.5% smaller than the tellerium atom. This results in local strain fields that can also serve as nucleation sites for defects and dislocation formation. Finally, the change in cation/anion fluxes when nitrogen is introduced and its effect on the growth dynamics is a complex issue that needs to be understood and optimized to ensure stochiometric growth. To gauge these effects, we have investigated the crystal quality and surface morphology of ZnTe:N epilayers grown on commercially-obtained ZnTe substrates and GaSb substrates using TEM, AFM, and x-ray diffraction.

## 2.2 Chapter Outline

This chapter has been organized as follows. In the first section, we present the results of characterizing and comparing GaSb and ZnTe substrates throughout their processing steps using primarily AFM. Next, the results of ZnTe:N grown on ZnTe substrates are presented. Two different approaches are used for the growth process, continuously doped and superlattices of delta-doped ZnTe:N with undoped ZnTe. We also discuss a model for defect generation based on nitrogen doping in ZnTe epilayers. Finally, the results of ZnTe:N/ZnTe superlattices grown on GaSb substrates are discussed and compared to the ZnTe substrate growths.

## 2.3 Substrate Characterization

We have studied the effects of two different substrates, commercially-obtained ZnTe and GaSb, on the crystal quality of ZnTe:N epilayers. The ZnTe substrates [7], doped p-type with antimony to a resistivity of 1.3 Ω cm, were grown using physical-vapor-transport with a proprietary seeding process which seeds a single crystal across a 2 inch wafer. X-ray rocking curve full width half maximum (FWHM)

| Sample Description | RMS (nm) | SD (nm) | Comments |
|---|---|---|---|
| ZnTe-RCA clean | 1.34 | 0.14 | Wavy |
| ZnTe-etched | 1.2 | 0.34 | Small pits |
| ZnTe-sputtered | 0.82 | 0.15 | Grains |
| GaSb-HCl clean | 1.1 | 0.07 | Grains |

Table 2.1: Summary of RMS and RMS standard deviation for substrate surfaces after processing steps

for these substrates ranged from 54 to 100 arc seconds. Further evidence of the substrate crystal quality was obtained by imaging the cleaved (110) plane using AFM. The surface showed several tilt boundaries which formed angles of 11-22°, corresponding to an edge dislocation every 5-10 atomic planes. The GaSb substrates, silicon doped p-type to about $10^{17}/\text{cm}^3$, were of higher crystal quality, with typical x-ray rocking curves FWHM of 15 arc seconds. While GaSb is nearly lattice matched to ZnTe (.15%), care must be taken to suppress interface reactions and substrate ion diffusion of Ga and Sb, which can act as dopants in ZnTe [8].

To prepare the substrate for epitaxial growth, surface oxides must be removed while minimizing surface roughness. For GaSb substrates, the surface oxides were removed by heating the substrate while under a sufficient Sb flux. ZnTe substrates, on the other hand, present a problem since the Zn and Te evaporate congruently at lower temperatures than ZnO. Thus the following steps were necessary to remove surface oxides prior to growth. First, a two minute soak was performed sequentially with TCE, acetone, and methonal to remove organics from the surface. Then a one minute 0.1% bromine/methanol etch was used to remove ionic contamination. The substrate was then annealed at 460°C in UHV to remove the tellurium oxides and finally sputtered with 3 keV Ar ions until Auger data indicated that the zinc oxides were removed.

We have performed a study of surface roughness of the ZnTe and GaSb substrates to investigate correlations between roughness and growth quality. The results from two substrates are shown in table 1. Nine images, acquired from different locations on the substrate, were used to calculate the average root mean square (RMS) and the RMS standard deviation of the image height data. Since the histograms of the AFM images are unimodal and gaussian-like, the RMS is a good measure of the surface roughness. The data was acquired with contact atomic force microscopy [9] with a silicon nitride tip with k = 0.58 N/m and a contact force of 5 nN. A contact force less than 5nN causes instabilities near rough features while a larger force caused a compression of the surface and a subsequent reduction in RMS values (30-40 nN forces reduced the RMS values about 5-10%). The ZnTe substrates, which oxidize slowly, were analyzed immediately in air after each process step. GaSb substrates, which oxidize more rapidly, were cleaned with HCl and methanol and analyzed in a glovebox with less than one ppm oxygen.

From table 1 we see that both substrates are quite similar in both roughness and morphology after their final step of processing. The GaSb substrate was slightly smoother than the sputtered ZnTe substrate yet both have small grains of less than 50 nm radius on the surface. The small grains on the ZnTe substrate are the result of sputtering damage. The grains on the GaSb substrate were most likely due to anisotropic oxide growth and their subsequent removal by HCL. Thus the variations in epitaxial quality grown on the subsequent layers are probably not due to variations in surface roughness but may be due to other substrate properties such as inherent strain, residual impurities or oxides on the surface, etc.

## 2.4 Growth Results-ZnTe substrate

For all growths, an undoped ZnTe buffer layer was grown followed by the nitrogen doped layer. The Zn:Te flux was adjusted during all growths to ensure slightly Zn-rich surface reconstruction. The radical nitrogen doping was produced by the

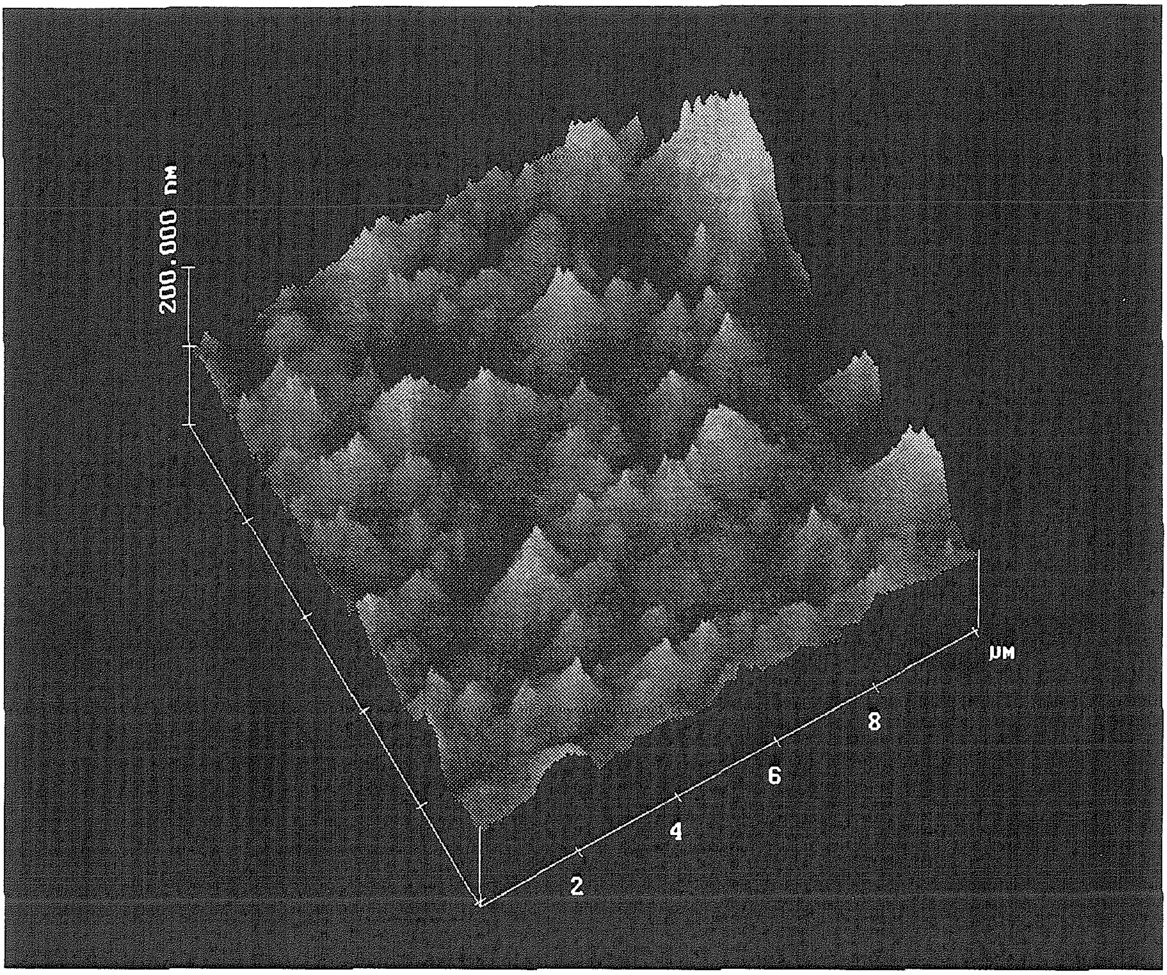

Figure 2.2: 10 $\mu$m x 10 $\mu$m AFM image of a continuous ZnTe:N epilayer grown on ZnTe substrate. Height range is 200 nm.

discharge of an Oxford Applied Research RF (13.5 Mhz) plasma source. The doping concentration was controlled by varying the nitrogen flow rate, which in turn was monitored by chamber pressure, for a fixed RF power. Doping levels were measured using standard Hall techniques. Two different approaches were used to obtain thick, conductive, nitrogen-doped epilayers: continuous doping during growth and delta doping between thicker undoped layers in a superlattice fashion. A comparison of the surface morphology resulting from these two approaches is illustrated in figures 2.2 and 2.3.

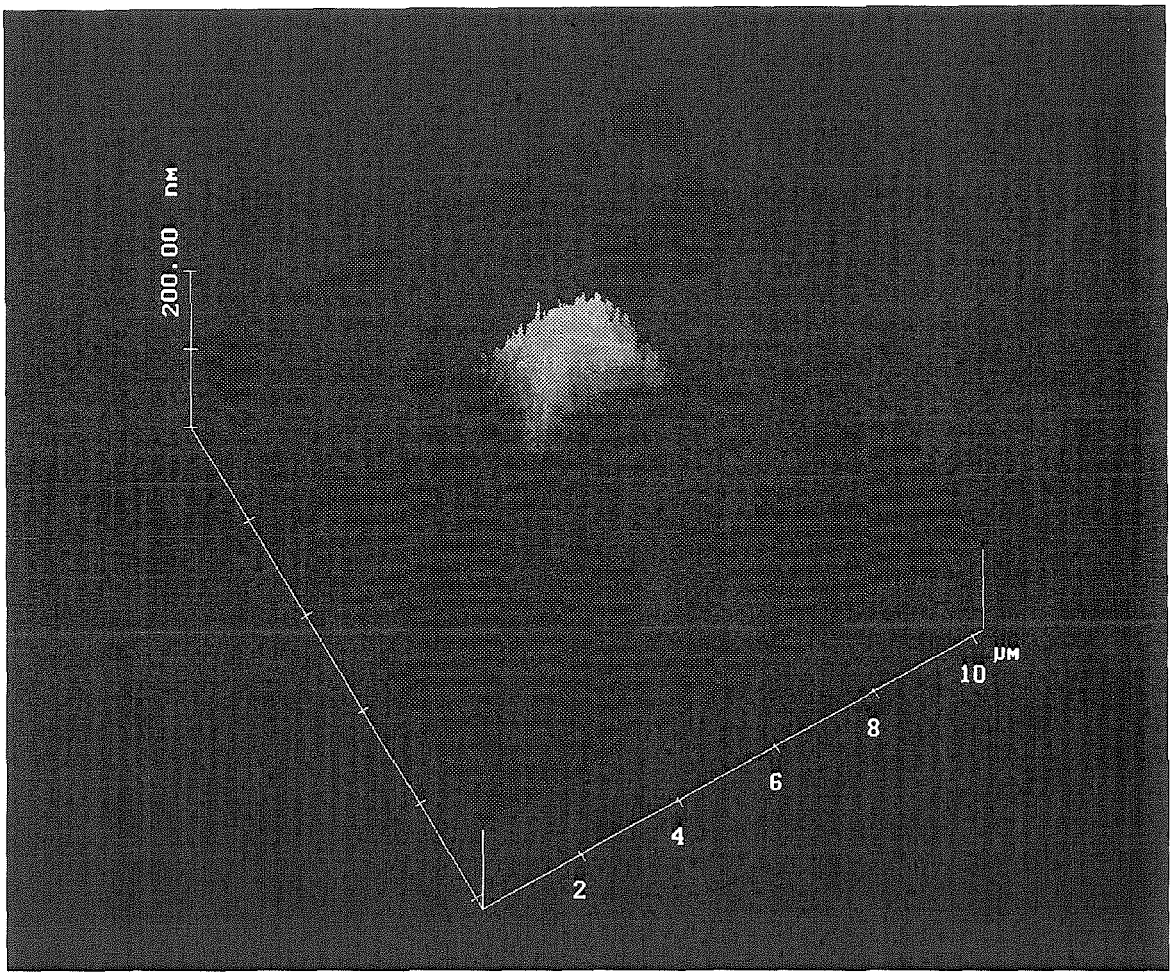

Figure 2.3: 10 $\mu$m x 10 $\mu$m AFM image of ZnTe:N/ZnTe superlattice grown on ZnTe substrate. Height range is 200 nm.

Figure 2.2 shows the surface of a sample grown with a 1.2 $\mu$m thick buffer layer followed by a 1.8 $\mu$m ZnTe:N doped to $10^{19}/\text{cm}^3$. The large RMS roughness of this surface, about 18.5 nm, is caused by a high defect density on the order of $10^8$ to $10^7$ defects/cm$^2$. X-ray rocking curves show that the epilayer is fully relaxed from the substrate.

Figure 2.3 shows the surface of a similar sample with a 0.5 $\mu$m buffer layer grown followed by a 40 period superlattice of 50 Å ZnTe:N and 500 Å ZnTe. The mean doping of the superlattice region is about $10^{18}/\text{cm}^3$. The surface RMS roughness has been reduced to about 4 nm with hillocks dispersed on the surface at a density of $10^6/\text{cm}^2$. The rocking curves again show that the epilayer is fully relaxed from the substrate. We have found that the hillocks, in general, take the form of the one shown in figure 2.3.

From the cross-sectional TEM of a hillock shown in figure 2.4, we see that the hillocks are bounded by $\{111\}$ fault planes that start at the substrate/buffer interface. When the sample's (110) face is further milled and tilted in the $[\bar{1}10]$ direction, additional $\{111\}$ twinning planes became visible that emanated from the superlattice/buffer layer interface region, as shown in figure 2.5. These sets of twin planes interact to form an amorphous core that provides the lift for the hillock peak.

The hillock model is presented in figure 2.6 and figure 2.7. Figure 2.6 shows graphically how the fault planes originate at both the substrate-buffer interface and at the buffer-superlattice interface. The different orientations were determined from the angles measured on the cross-sectional TEM images along with electron diffraction patterns of the different planes visible on these images, and dimensions measured using AFM images. As shown in figure 2.7, the edges of these hillocks lie in the $<110>$ directions, which is just the intersection of the $\{111\}$ fault planes with the (001) surface. The $\{111\}$ fault planes originating at the substrate/buffer, as in figure 2.4, interface define the $[\bar{1}10]$ base of hillocks while the $\{111\}$ fault planes originating at the superlattice/buffer interface define $[110]$ base of hillocks, as in

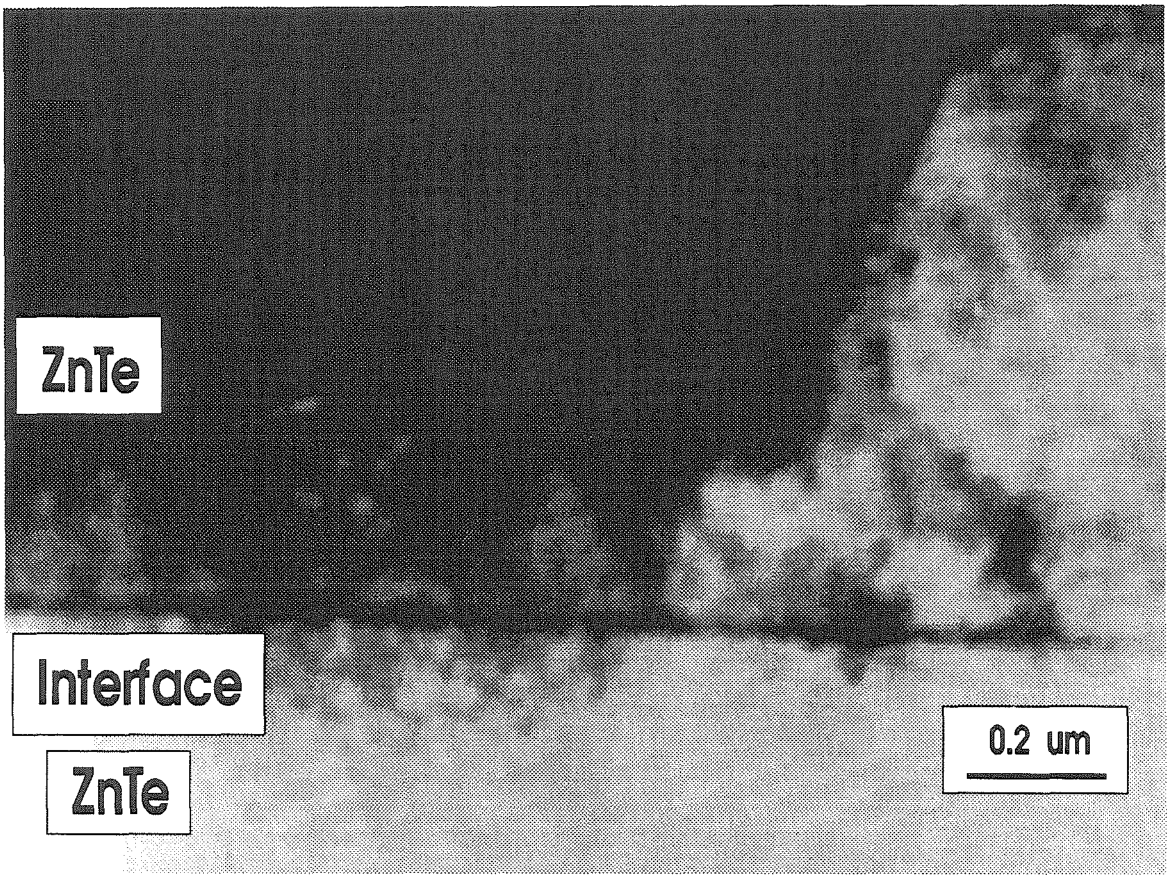

Figure 2.4: TEM cross-section ZnTe:N/ZnTe superlattice showing hillock originating from substrate/buffer interface

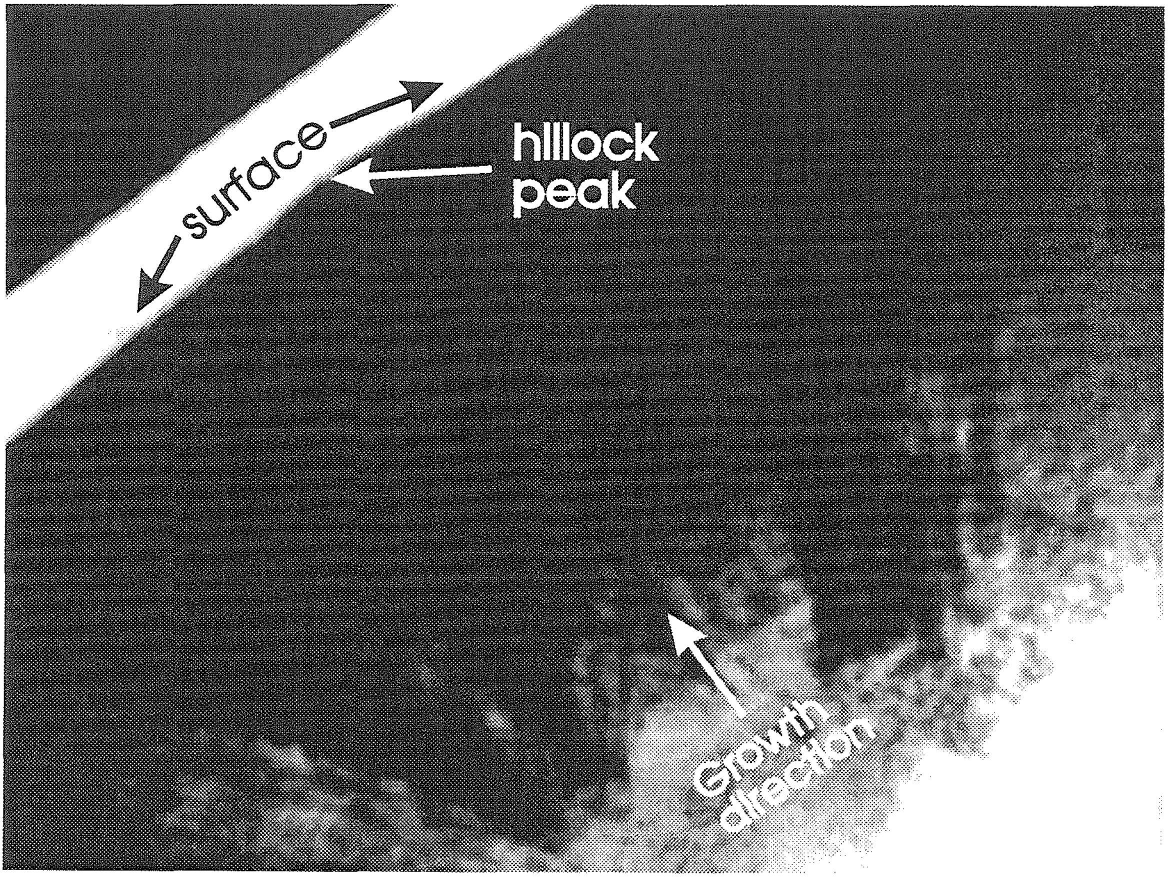

Figure 2.5: Fault planes originating at superlattice/buffer interface with Zn $\{111\}$ planes visible

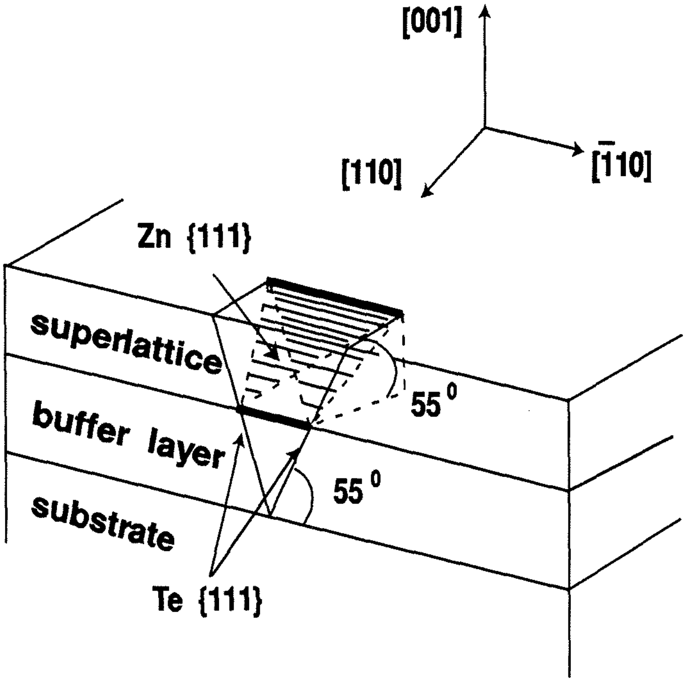

Figure 2.6: Side view showing 111 stacking fault planes at the superlattice layer and substrate-buffer layer

figure 2.4b. This is confirmed from the hillock's dimensions: the hillock in the [$\bar{1}$10] direction is $\sqrt{2}$ times the thickness of the entire epilayer while in the [110] direction the base is $\sqrt{2}$ times the thickness of the superlattice layer. However, about 10% of the hillocks have a larger base in the [110] direction than predicted with a few hillocks even forming symmetric pyramids. This indicates that some of the fault planes bounding the [110] base of the hillocks begin between the superlattice and substrate.

We have identified the {111} fault planes originating at the substrate to primarily be the Te {111} planes and the ones originating at the superlattice as primarily the Zn {111} planes through a selective etching technique. The technique involves etching the (001) surface in a solution of 20 ml: 10 ml: 4 gm of water, nitric acid, and potassium bichromate, respectively, and a trace of silver nitrate [10]. The nitric acid primarily attacks the zinc while $(Cr_2O_7)^{-2}$, a strong oxidizer, reacts

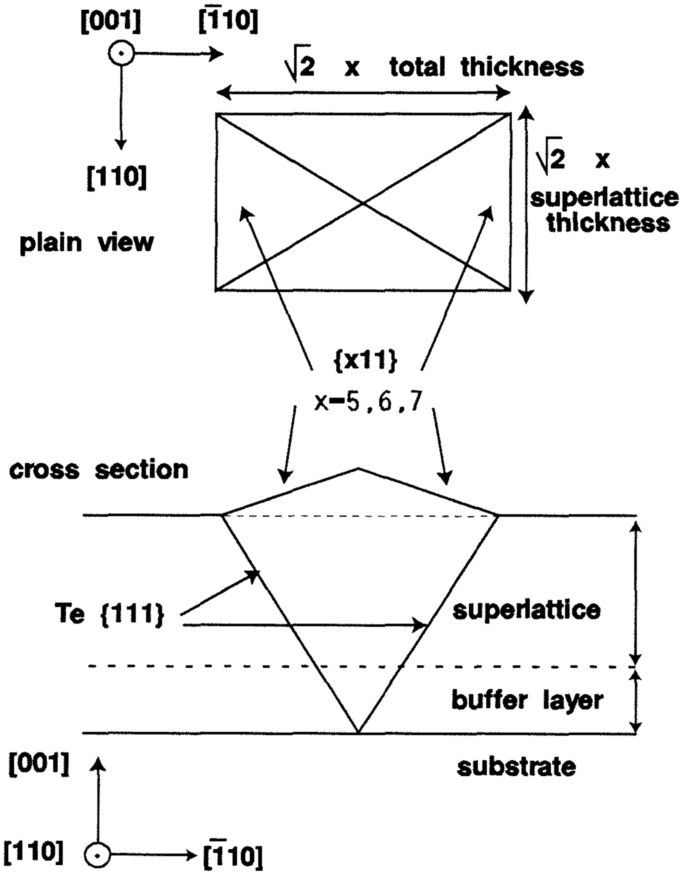

Figure 2.7: Front view of hillock model for ZnTe:N superlattice on ZnTe substrate

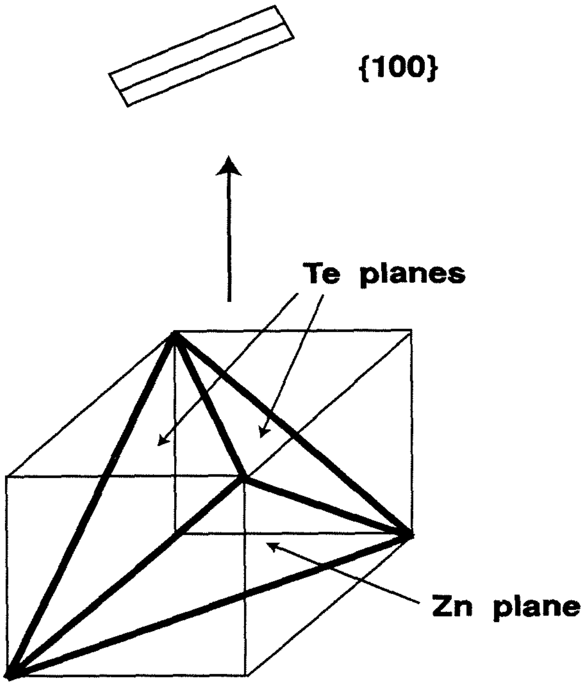

Figure 2.8: Formation of rectangular etch pit from (100) surface

with the tellurium to produce $TeO_2$, which is soluble in an acidic solution. The silver nitrate suppresses the zinc reaction so the tellurium reaction proceeds more rapidly [11]. This causes a rectangular shaped pit to form on the (001) surface with the short sides along the Te {111} planes and the long sides along the Zn {111} planes (see figure 2.8). Thus by noting the orientation of the etch pits with relation to hillock's orientation, we observed that the {111} planes emanating from the substrate interface are parallel to the Te planes as defined by the etch pits.

One possible reason why the Zn {111} twin planes preferentially form at the superlattice is because the nitrogen dopant forms a stable state with one broken Zn bond. This broken bond and the strain due to the short nitrogen radius acts to form dislocations along the Zn {111} planes. For the Te {111} fault planes, their origin is even more difficult to deduce since there is such a high concentration of defects near the substrate interface. Perhaps stochiometry problems during initial growth could lead to local Te-rich conditions which are known to cause hillock formation [12].

## 2.5 Growth Results-GaSb substrate

After a 1400 Å buffer of GaSb was grown on the GaSb substrates, the sample was transferred to a II-VI MBE chamber through a UHV transfer tube where a buffer layer of ZnTe was then grown. The first several atomic layers were usually grown at lower substrate temperatures (270 °C) than the rest of the growth (300 °C) in order to reduce interface reactions and substrate ion diffusion.

The cross-sectional TEM of a sample with a similar ZnTe:N/ZnTe superlattice epilayer doped to $10^{18}/\text{cm}^3$ in figure 2.9 shows a sharp reduction in dislocation density in this layer. The x-ray rocking curves now show that the epilayer is partially strained to the substrate.

As seen from high resolution TEM of the GaSb/ZnTe interface in figure 2.10, there is a visible region where interface reactions have occurred. In addition, we see that faults meet and eliminate each other in the epilayer. Thus, we do not observe their propagation through the doped epilayer nor do we see significant dislocation generation in this layer.

The surface morphology shown in figure 2.11 further illustrates the epilayer crystal quality. The RMS roughness of the surface has now been reduced to 1.7 nm without hillock formation. There does appear to be small precipitates on the surface with a maximum height of 10 nm. These are not the result of dislocations propagating in the epilayer as confirmed by TEM and may be substrate precipitates or Te pooling.

## 2.6 Summary

In conclusion, we have found that substrate selection is critical to growing high quality pseudoepitaxial layers of ZnTe:N. Prepared ZnTe substrates, although sim-

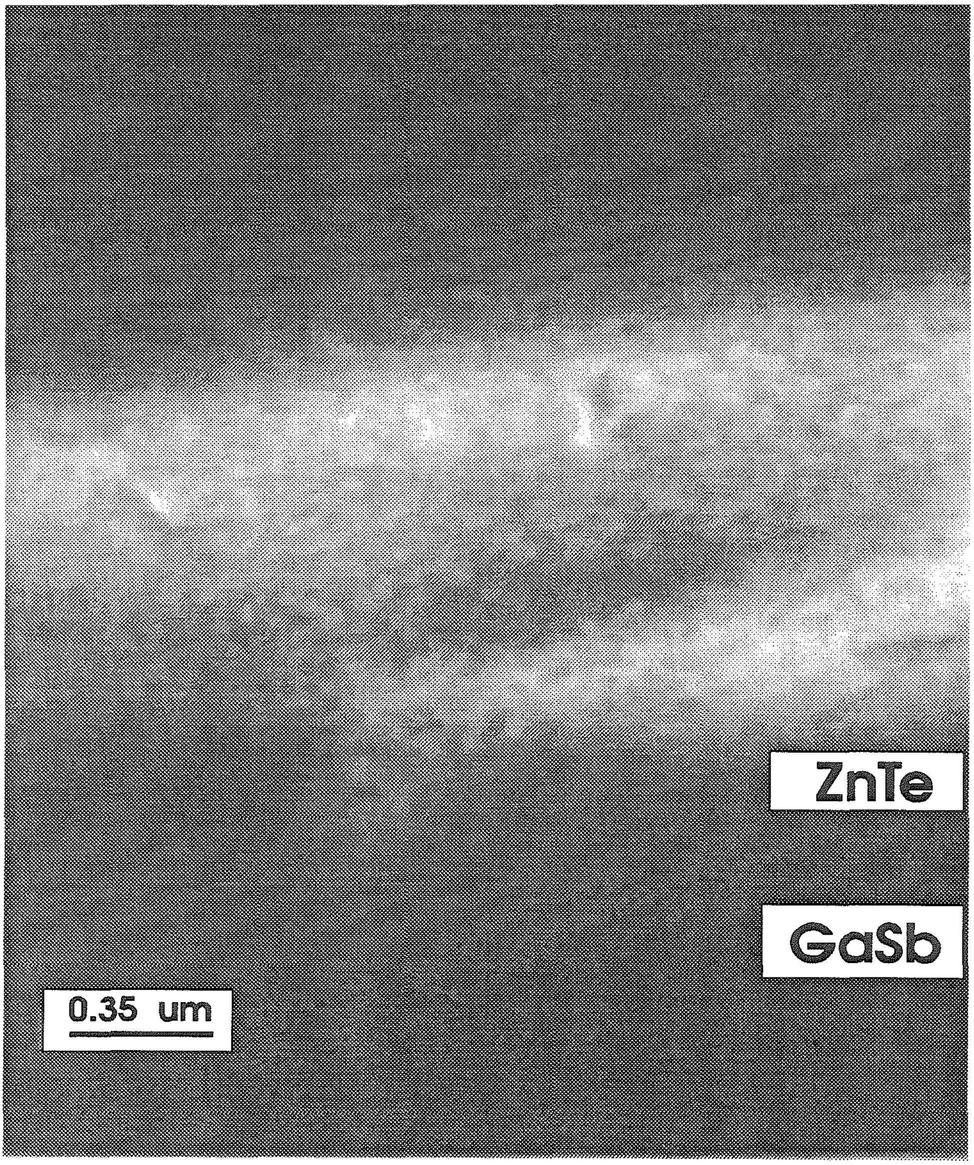

Figure 2.9: TEM cross-section of ZnTe:N epilayer grown on GaSb substrate

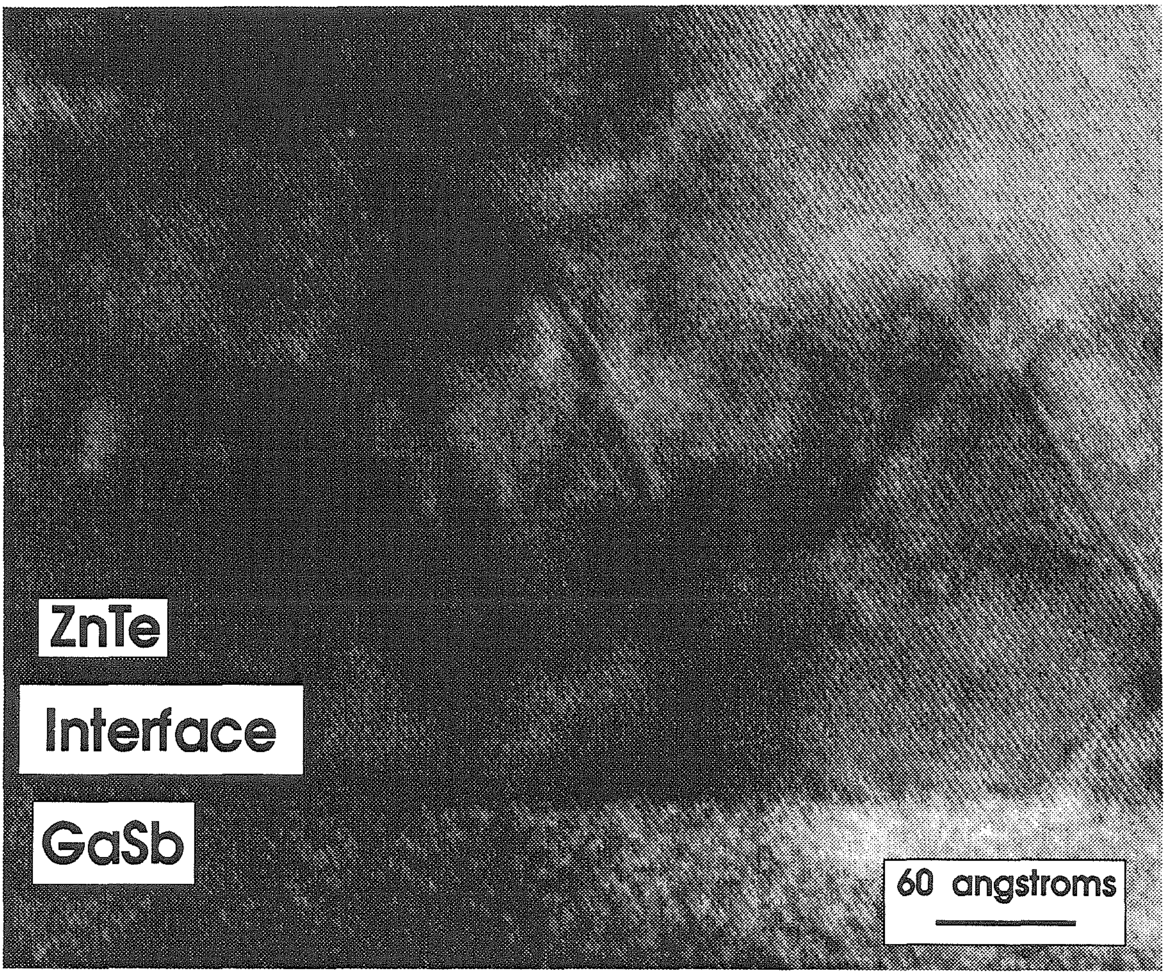

Figure 2.10: HRTEM of ZnTe/GaSb interface

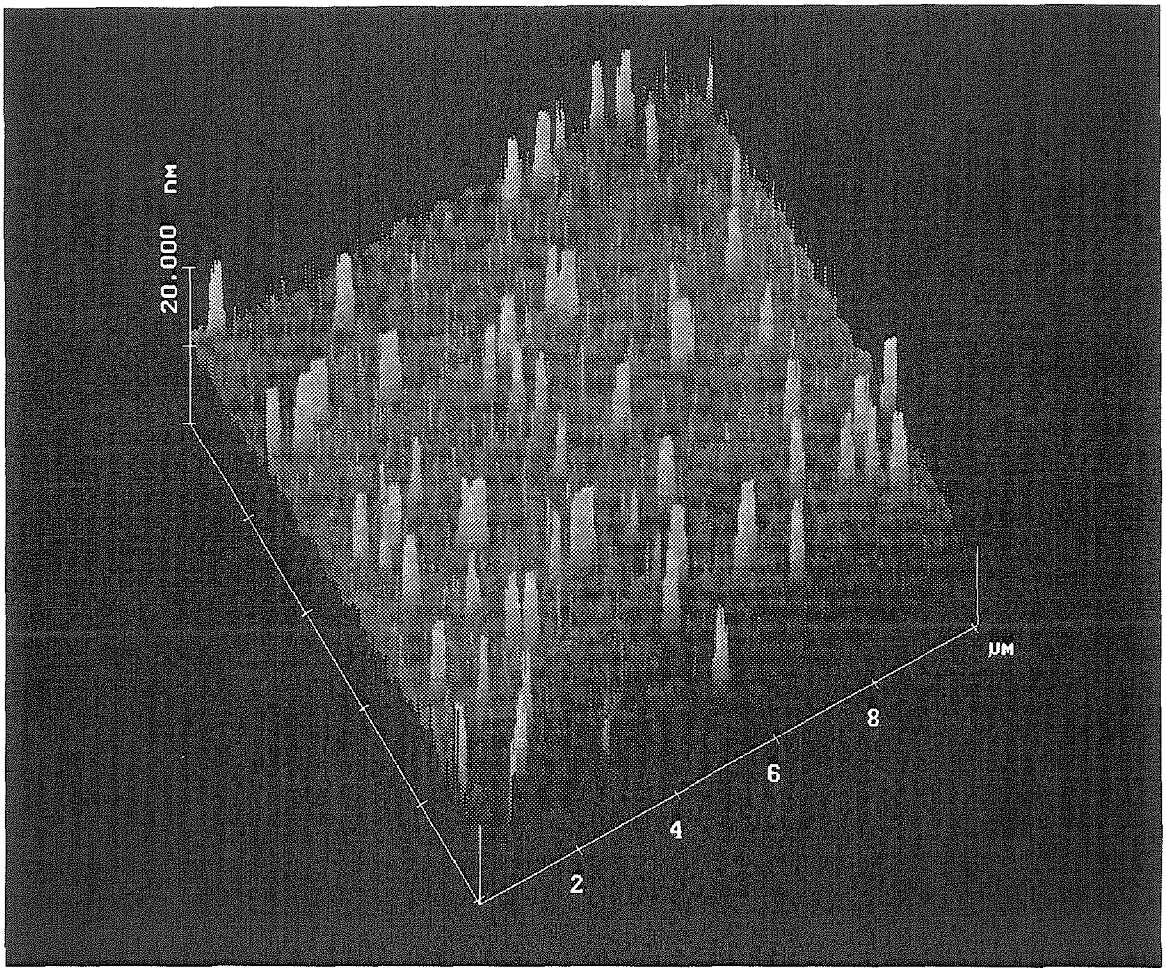

Figure 2.11: 10 $\mu$m x 10 $\mu$m surface of ZnTe:N epilayer grown on GaSb substrate. Height range is 20 nm.

ilar in morphology and roughness to GaSb substrates, yields inferior epilayers of both continuously grown ZnTe:N and ZnTe:N/ZnTe superlattices. High levels of nitrogen doping appear to encourage hillock formation and can be explained by a simple model which we propose. Hillocks found on the ZnTe substrates with superlattice doping layers are the result of Te $\{111\}$ fault planes originating at the substrate interface and Zn $\{111\}$ twin planes originating at the superlattice interface. The dislocation density in the epilayers grown on GaSb were reduced by a factor of 10-100 with no hillock growth but evidence of precipitates on the surface.

# Bibliography

[1] R. M. Park, M. B. Troffer, C. M. Rouleau, J. M. DePuydt, and M. A. Hasse, *Appl. Phys. Lett.* **57**, 2127 (1990).

[2] Y. Fan, J. Han L. He, J. Saraie, R. Gunshor, M. Hagerott, H. Jeon, A. Nurmikko, G. C. Hua, and N. Otsuka, *Appl. Phys. Lett.* **61**, 3160 (1993)..

[3] M. Haase, J. Qui, J. DePuydt, and H. Cheng, *Appl. Phys. Lett.* **59**, 1272 (1991).

[4] M. C. Phillips, J. F. Swenberg, M. W. Wang, J. O. McCaldin, and T. C. McGill, Physica B **185**, 485 (1993).

[5] D. J. Chadi, *Appl. Phys. Lett.* **59**, 3589 (1991).

[6] J. F. Swenberg, M. W. Wang, M. C. Phillips, and T. C. McGill, submitted to *J. Cryst. Growth* .

[7] Eagle-Picher Research Laboratory, Maimi, Oklahoma

[8] Y. Rajakarunanayake, B. H. Cole, J. O. McCaldin, D. H. Chow, J. R. Soderstrom, and T. C. McGill, *Appl. Phys. Lett.* **55**, (1989).

[9] Nanoscope III, Digital Instruments, Inc, Santa Barbara, Ca.

[10] M. Inoue, I. Teramoto, and S. Takayanagi, *J. Appl. Phys.* **33**, 2578 (1962).

[11] Y. Lu, R. K. Route, D. Elwell, and R. S. Feigelson, *J. Vac. Sci. Technol. A* **3**, 264 (1985).

[12] R. D. Feldman. R. F. Austin, P. M. Birdenbaugh, A. M. Johnson, W. M. Simpson, B. A. Wilson¡ and C. E. Bonner, *J. Appl. Phys.* **64**, 1991 (1988).

# Chapter 3

# Surface Morphology Of Silicon Grown On $CaF_2/Si$ by Electron Beam Assisted MBE

## 3.1 Introduction

The development of quantum devices such as resonant tunneling diodes has lead to advancements in several different fields including ultra dense digital memory circuits, high-speed electronics, and neural networks. In addition, SOI (semiconductor on insulator) is another promising development for silicon-based systems to enhance device performance since it improves the isolation of devices and reduces parasitic capacitance. However, despite the significance of these advances, at the present time there exist material problems that prevent the integration of such devices into silicon-based chips using standard VLSI silicon technology. One leading candidate for this integration effort is the $Si/CaF_2$ material system since the lattice mismatch is small (0.6 % at room temperature) and the crystalline structures are similar. Consequently, the system has been studied extensively and it was found that while $CaF_2$ grows in a two-dimensional epitaxial fashion on silicon

(111), silicon islands on $CaF_2$ [15]. In this chapter, we present the results of our efforts to reduce the tendency of the silicon to island by using a technique known as electron beam assisted molecular beam epitaxy (EB MBE). This technique has been used to improve growth of both Ge [2] and GaAs [3] on $CaF_2$, but as far we know there have not been any reports on its use in the growth of silicon on $CaF_2$. Through EB MBE, we investigate the effects of electron dosage and the growth temperature on the silicon surface morphology and roughness.

In EB MBE the $CaF_2$ surface is exposed to electrons in order to desorb fluorine from the $CaF_2$ surface before silicon is grown on it by MBE. It has been shown that low energy electron radiation desorbs fluorine as $F^+$ from the $CaF_2$ and creates an ordered array of surface F-centers on $CaF_2(111)$ [9]. A detailed mechanism for the desorption process which involves excitations of the Ca $3p$ core level has been proposed by Chakarian [5]. The array of F-centers will have a higher surface free energy than the $CaF_2$ surface and should thus favour 2D growth or at least lower the contact angle in 3D growth of silicon on $CaF_2$.

## 3.2 Chapter Outline

This chapter is organized as follows; in the experimental section we describe the sample structure and basic format for the study. The next two sections present cross-sectional TEM images for typical irradiated and nonirradiated structures along with AFM images for both the high (650 °C) and low (500 °C) temperature growths. In the data analysis section, we plot the relationship between surface RMS as a function of electron dosage and growth temperature along with supporting LEED and XPS data. In the discussion section we explain the results using a simple geometrical thermodynamics model. In the sixth and final section, we summarize the results.

## 3.3 Description of Experiment

The sample used in the experiment has three layers: 50 nm silicon on 10 nm $CaF_2$ on a 100 nm thick silicon buffer grown on a silicon (111) substrate. The reason for choosing a thick $CaF_2$ layer is to prevent electron beam penetration through it. Early TEM studies showed that 10 nm is sufficient for this purpose. Since the AFM measurements were performed in air, we chose a relatively thick (50 nm) silicon overlayer to ensure that the surface features due to oxidation are about a factor of 10-50 times smaller than the features due to the electron beam exposure.

Before growth, we degreased the 2 inch (boron doped to $3 \times 10^{18}$ $cm^{-3}$) silicon wafer and dipped it in a 25% HF solution in order to remove the contaminated native oxide and terminate the surface with hydrogen. Each wafer was exposed to the electron beam at four different locations in order to reduce scatter in the data due to variations in surface preparation and growth conditions. The background pressure in the MBE machine was about $10^{-9}$ Torr during electron beam exposure and $10^{-8}$ Torr during the growth. During silicon deposition, the substrate temperature was kept at 650 °C for the high temperature growth and 500 °C for the low temperature growth. During $CaF_2$ deposition the substrate temperature was kept at 700 °C. The deposition rates for $CaF_2$ and Si were 0.05 nm/sec and 0.04 nm/sec, respectively.

The Si buffer layer exhibited a sharp 7x7 LEED pattern. The surface morphology for AFM images of this surface is smooth and featureless with a mean RMS roughness of less than 2 nm. This pattern changed to the expected 1x1 pattern after the $CaF_2$ had been deposited.

To expose the surface, we defocussed the LEED beam to a spot diameter of about 4 mm and set the dose rate to 0.85 $\mu A/cm^2$ for the samples with doses ranging from zero to 1.0 $mC/cm^2$ and 12 $\mu A/cm^2$ for the samples with doses ranging from 0.5 to 50 $mC/cm^2$. The LEED pattern remained the same (except the spots were larger due to the defocussing) for the doses up to 1.0 $mC/cm^2$. The

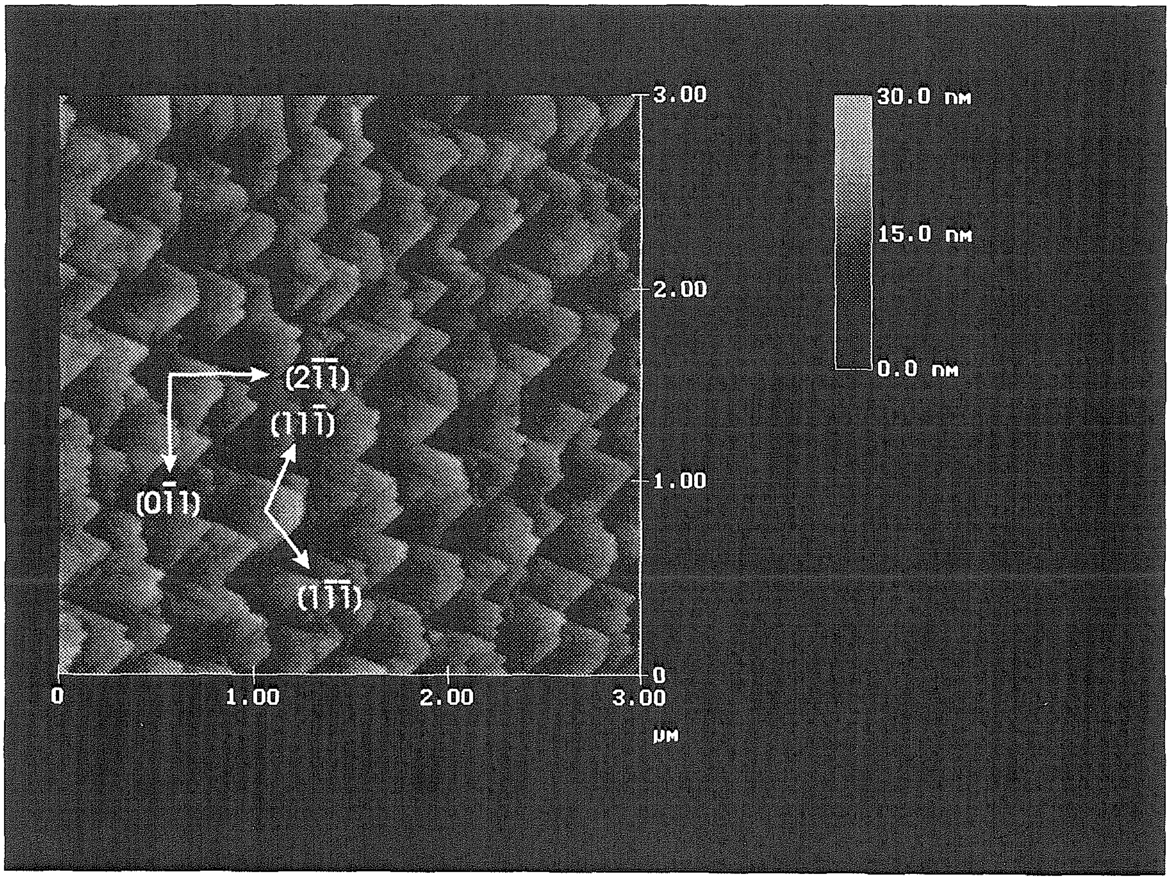

Figure 3.1: AFM image of $CaF_2(111)$ grown on a silicon (111) by standard MBE at 700 ° C.

unchanging LEED pattern shows that the surface remains ordered, indicating that the F-centers created by fluorine desorption form an ordered array [9]. For higher doses the LEED pattern lost contrast, which we interpret as a disordering of the $CaF_2$ surface by the electron irradiation. Figure 3.1 shows a AFM image of the $CaF_2$ surface. The surface forms triangular crystalites with a mean roughness of about 2.9 nm. The base of the triangular crystalites is along the $[\bar{2}11]$ direction, which is the same direction that the substrate is miscut by 6°. This miscut produces steps at which the $CaF_2$ would preferentially deposit due to the larger number of Si dangling bonds at the step than on the flat surface. From figure 3.1 we measured the triangular sides and found them to be in the $< 111 >$ directions, which is the lowest surface free energy face of $CaF_2$. Thus the triangular shape appears to be due to the surface free energy minimization of the $CaF_2$ crystal with preferential deposition at the step face. We could not detect any morpological or roughness differences between irradiated regions up to 1.0 $mC/cm^2$ and nonirradiated regions of the $CaF_2$ surface, suggesting that the electron irradiation damage of the surface is negligible. The silicon overlayers all exhibited a 1x1 pattern with fairly large spot size compared to the buffer layer.

Figure 3.2 shows a TEM cross-section for the entire structure for a nonirradiated and a low irradiated growth. Although stacking faults can be seen throughout the $CaF_2$ and subsequent silicon layers in both grows, it is apparent that the morphology is smoother in the EB grown sample. The abundance of stacking faults can be explained by a simple model. First, $CaF_2$ layers of this thickness have been observed to have large tensile strain in the plane parallel to the interface [14]. This strain is tensile because $CaF_2$ has a larger thermal expansion coefficient than Si (19 x $10^{-6}K^{-1}$ verses 2.5 x $10^{-6}K^{-1}$ at room temperature). At 700 ° C, the lattice of $CaF_2$ is about 2% larger than Si. Thus if a sufficient number of misfit dislocations are introduced during growth to relieve strain, when the structure cools tensile planar stress will form. A stepped surface (the substrate was cut 6° off the $[\bar{2}11]$ axis) will pin these dislocations, preventing plastic deformation at the interface and leading to the formation of stacking faults in the $CaF_2$ and subsequent Si layer.

## 3.4 High temperature growth: AFM and TEM images

Figure 3.3 shows the morphology (as measured by AFM) of the silicon overlayer with zero electron dose (since there are electron guns in the MBE system, there is a background of electrons, but this dose has a small compared to the doses used in this experiment). The islands are about 100-300 nm in diameter and many are hexagonal. The sides of the islands are generally aligned along the <011> directions of the substrate. The contact angles (defined in figure 3.9c) of the islands vary over a large range (0°-50°). This variation is probably due to the fact that the islands are in various stages of coalescing at the $Si/CaF_2$ interface. Experimentally we see that, in general, the stronger the coalescence, the lower the contact angle. “Free standing faces,” faces that are comparatively far from other islands, have a contact angle of 39° ± 5°.

The smoothest overlayer was obtained with an electron dose of 1.0 $mC/cm^2$. From figure 3.4, one sees that the island size distribution is similar to the zero dose case, however, the roughness of the surface is considerably less. There are fewer islands that are comparatively far from other islands and thus the contact angles are smaller; for the “free standing faces” the contact angles are 32° ± 5°.

## 3.5 Low temperature growth: AFM images

Figure 3.5 shows a comparison of the surface morphology for the both the unexposed surface and 1.0 $mC/cm^2$ grown at 500 ° C. It is again obvious that the exposed surface has a smoother morphology as compared with the unexposed one. One also notices that the unexposed surface appears amorphous and is not com-

Standard Si/CaF$_2$ Growth

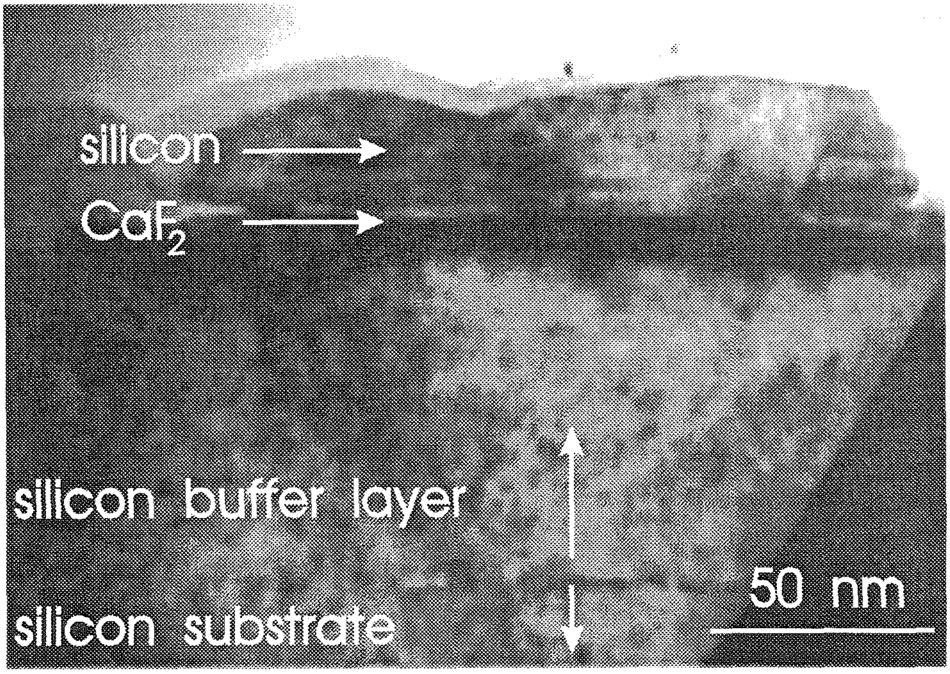

EB assisted Si/CaF$_2$ Growth

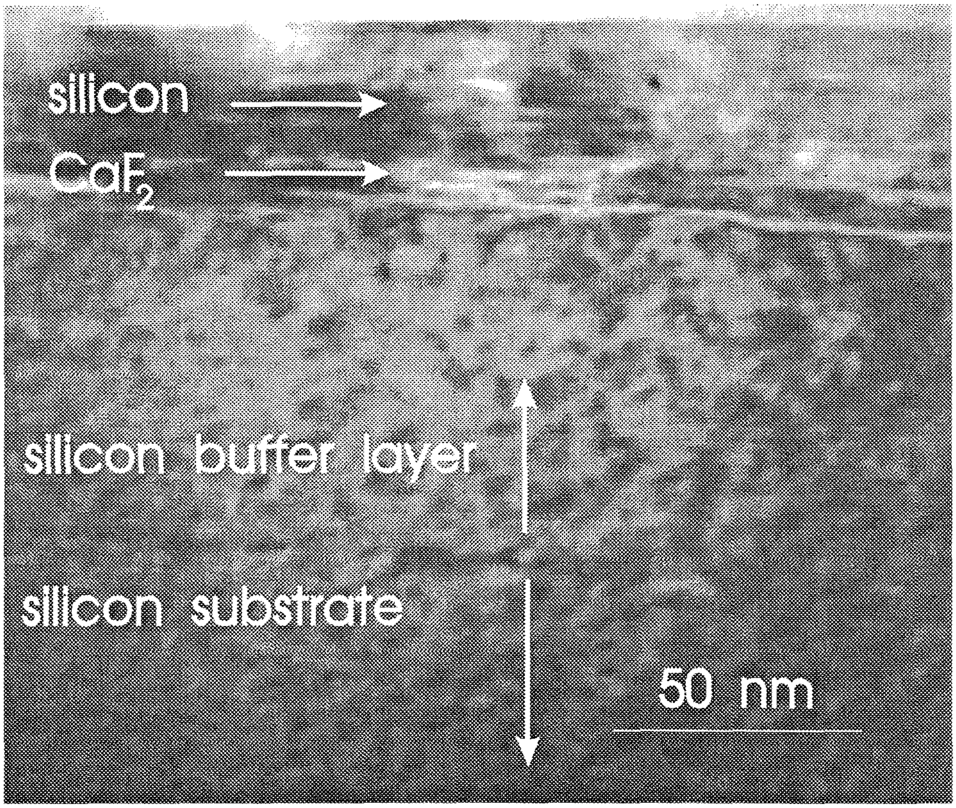

Figure 3.2: Typical TEM cross-section of silicon grown on CaF$_2$(111) by standard MBE and EB MBE at 650 ° C.

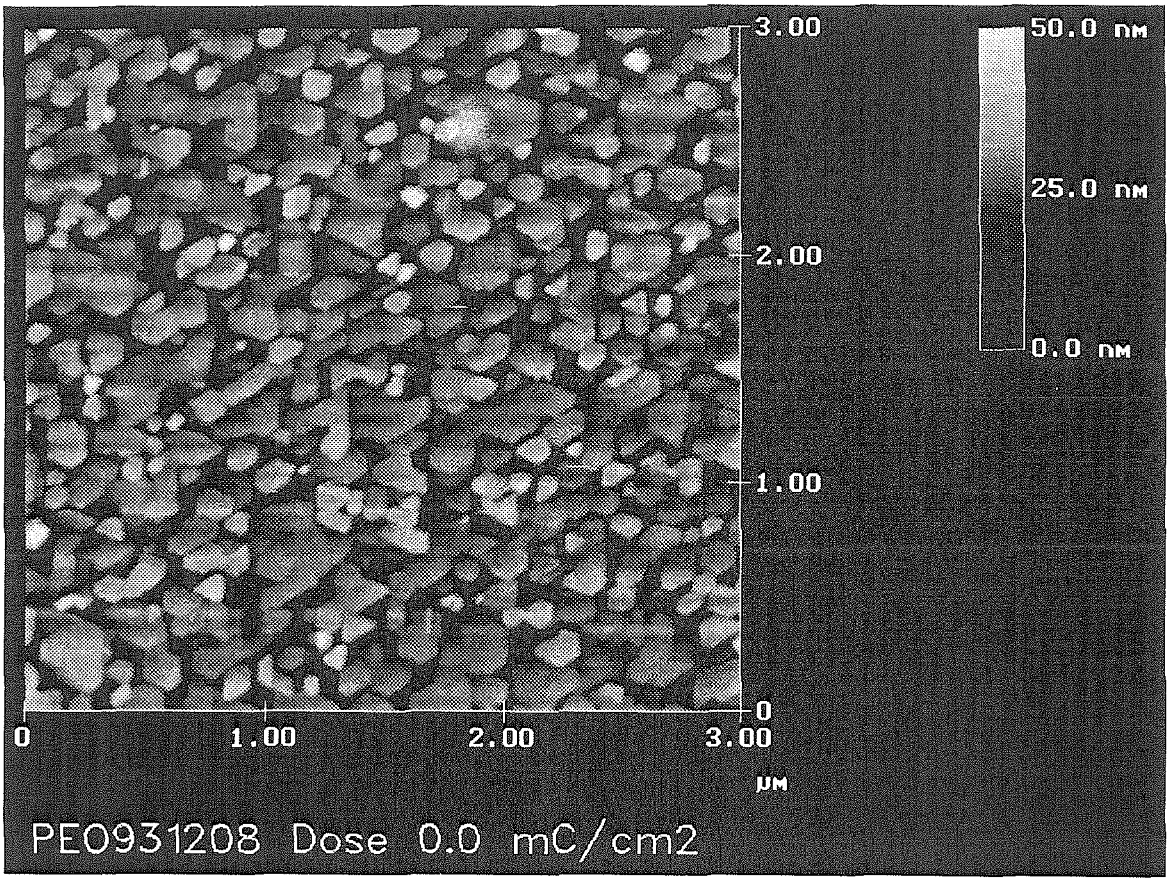

Figure 3.3: AFM image of silicon grown on $CaF_2(111)$ by standard MBE at 650 ° C.

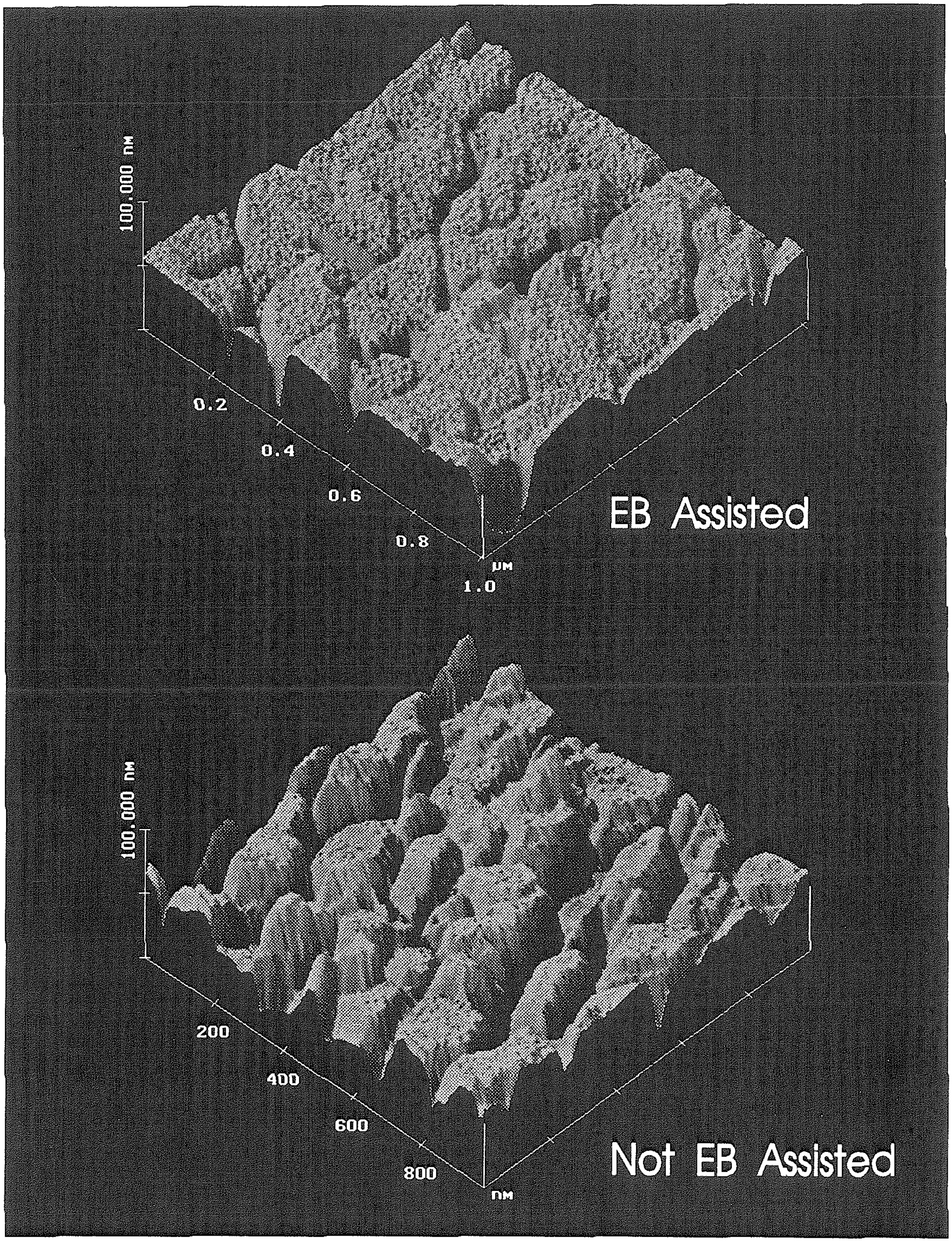

Figure 3.4: Comparison of AFM image of silicon grown at 650 ° C on $CaF_2(111)$ by electron beam assisted MBE with an electron dose of 1.0 $mC/cm^2$ with standard growth surface.

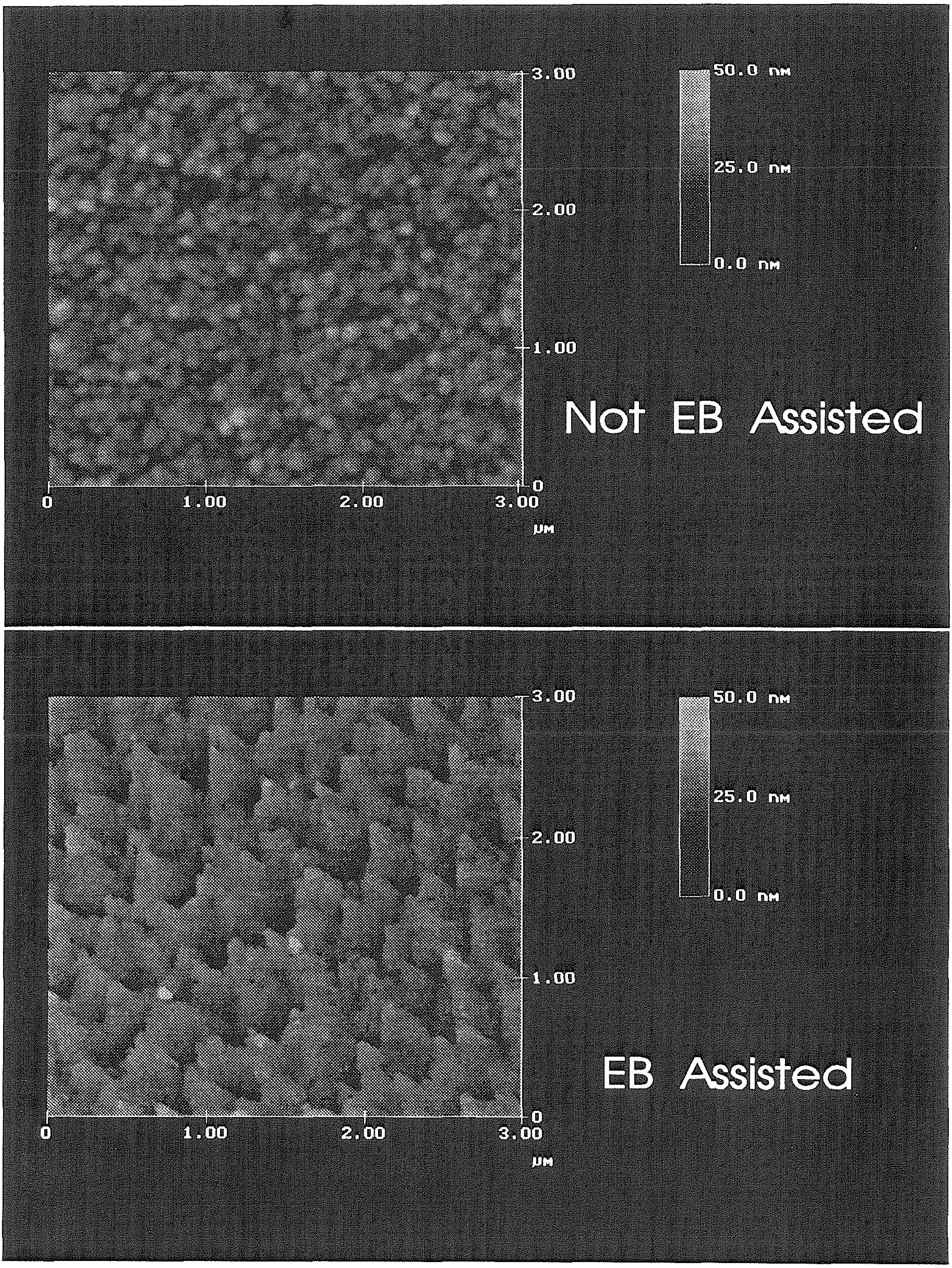

Figure 3.5: Comparison of AFM image of silicon grown at 500 ° C on $CaF_2(111)$ by electron beam assisted MBE with an electron dose of 1.0 $mC/cm^2$ with standard growth surface.

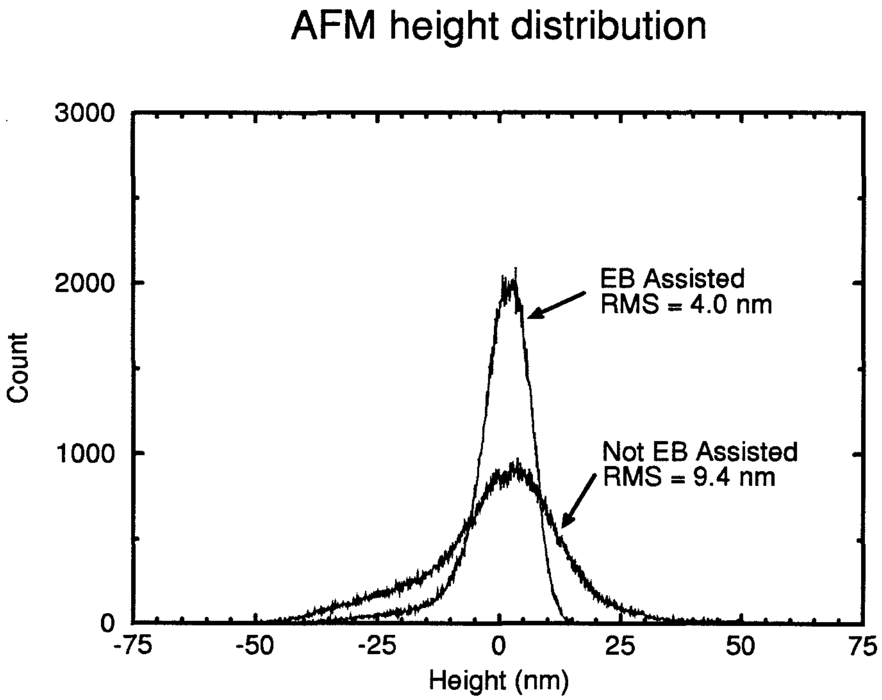

Figure 3.6: Comparision of two histograms of AFM Micrographs of growths performed at 650 ° C and their RMS roughness.

posed of well defined microcrystals. This is expected since the temperature is below the epitaxial growth temperature (525 °C) of silicon on $CaF_2$. However, as the dosage to the surface is increased, the surface undergoes an ordering to form smoother triangular crystalites, similar in size, shape, and orientation to the $CaF_2$ surface (see figure 3.1). This similarity suggests that the Si smoothly deposits on the $CaF_2$ triangular crystalites when the $CaF_2$ is irradiated.

## 3.6 Data analysis: High temperature growth

Figure 3.6 shows the histograms of two different samples and their respective root mean square (RMS) of the data. Since the histograms of the AFM images acquired in the constant force mode are unimodal and gaussian-like, the RMS is a good measure of the surface roughness.

It is important to note that the measured roughness depends not only on the surface morphology, but also on the magnitude of the force, the scanning rate, and the condition of the tip. Thus, in order to ensure that the measurements were quantitatively comparable, we used a small repulsive force (7.9 nN) and a slow scan rate (15 min/image). In order to check for tip modification, we scanned a calibration sample between each roughness measurement. Figure 3.7 shows that the roughness is significantly lower for the irradiated samples (the line drawn in the picture is there only to guide the eye). Overlapping data points at 0.5 and 1.0 mC/cm$^2$ are present because two samples were used for the high temperature growth study; one for low dosages and one for higher dosages. The roughness exhibits a broad minimum followed by an increase in roughness at 10 mC/cm$^2$. The surface morphology is similar for the doses up to 1.0 mC/cm$^2$; at 10 and 50 mC/cm$^2$, the morphology is completely different.

The higher dosage surface can be characterized as follows. At a dose of 10 mC/cm$^2$, the islands are shapeless, tall and spaced far apart (see figure 3.8). The islands do not to seem to have any specific crystal faces, instead their shape appears to be flattened spheres. In general, they stand about 50 nm tall with base diameter of about 200 nm and the spacing between them is about 2.5 $\mu$m. All of these values are rough averages with large (50% of the mean) standard deviations. The surface between the islands does not show any specific crystalline faces either and is relatively smooth, with a RMS roughness of about 2.2 nm. The reason for this change in surface morphology is probably due to the $CaF_2$ surface being randomized by the electron beam as indicated by the LEED. At a dose of 50 mC/cm$^2$, there are 40 nm deep triangular pinholes spaced about 1 $\mu$m apart instead of islands (see figure 3.8). The surface between the holes also shows triangular features. Again, we think that the damage done to the $CaF_2$ during the electron beam exposure is the reason for this change in surface morphology.

The $CaF_2$/Si XPS peak ratios shown in table 3.1 supplies additional evidence

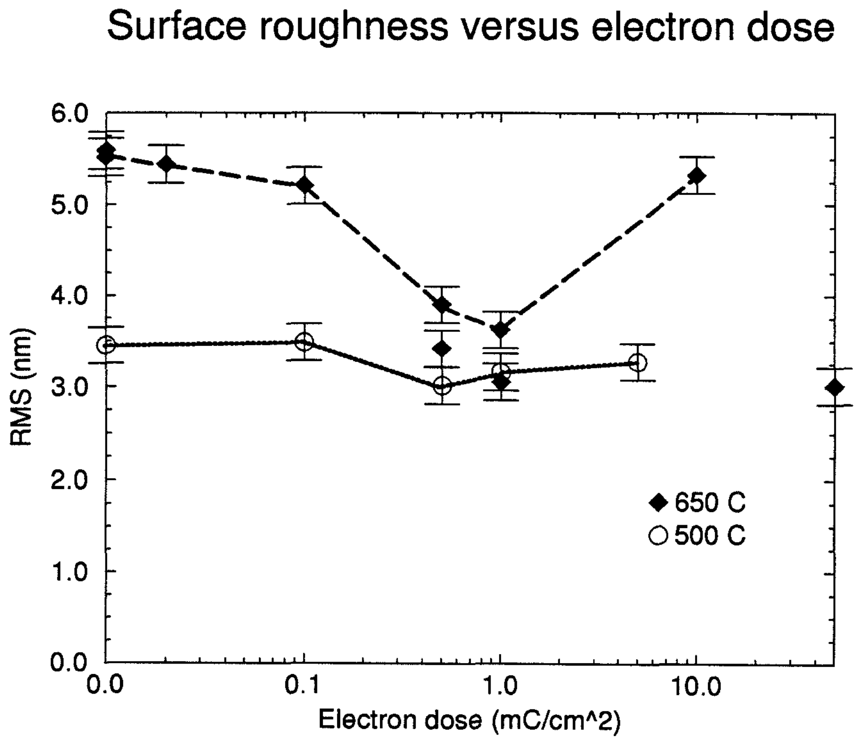

Figure 3.7: RMS of silicon grown on $CaF_2(111)$ versus electron dose for high and low growth temperatures.

Table 3.1: Calcium to silicon and fluorine to silicon XPS peak ratios of silicon grown on $CaF_2$ using electron assisted MBE (EB MBE). The dose refers to the electron dose used in the EB MBE growth. The samples were sputtered about 3 nm; the table shows the ratios both before and after the sputtering.

| Dose ($mC/cm^2$) | Ca/Si | | F/Si | |
|---|---|---|---|---|
| | pre sputter | post sputter | pre sputter | post sputter |
| 0 | 0.45 | 0.07 | 0.45 | 0.13 |
| 1 | 0.30 | 0 | 0.07 | 0 |
| 10 | 0.33 | 0 | 0.14 | 0 |
| 50 | 0.33 | 0 | 0.04 | 0 |

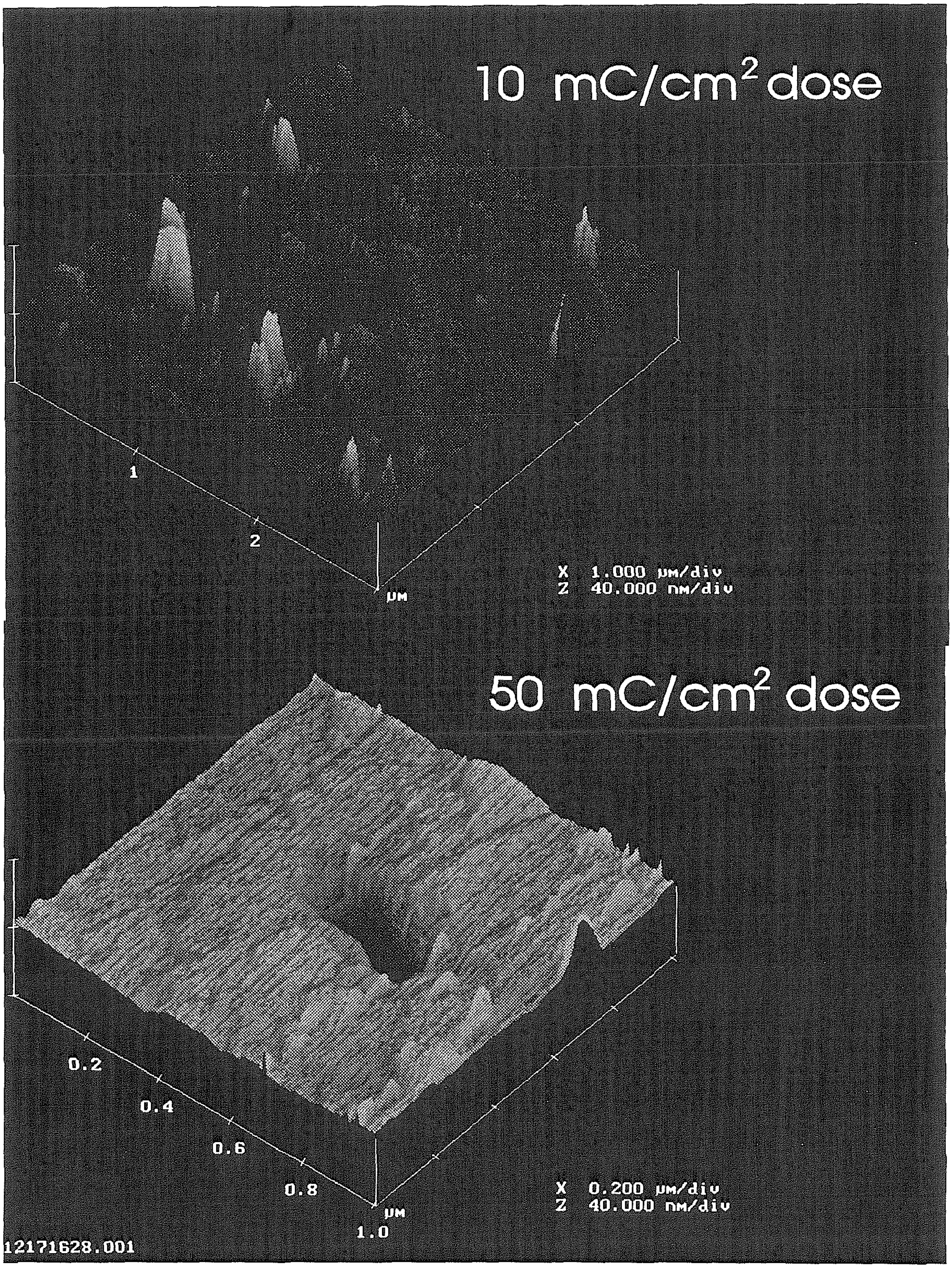

Figure 3.8: AFM image of silicon grown on $CaF_2(111)$ for 10 $mC/cm^2$ and 50 $mC/cm^2$ dosages grown at 650 °C

that the silicon nearly covers the $CaF_2$ in the 1.0 $mC/cm^2$ case whereas the coverage is incomplete in the zero dose case. The fluorine/silicon ratio is largest in the zero dose and diminishes significantly for the 1.0 $mC/cm^2$ surface. After sputtering about 3 nm, the calcium and flourine peaks vanish in all but the zero dose case. This is consistent with the model that the zero dose morphology consists of tall islands with valleys between whereas the $CaF_2$ surface in the 1.0 $mC/cm^2$ case is nearly completely covered with silicon. The tall islands shield the $CaF_2$ during sputtering, thus only the zero dose case shows calcium and fluorine peaks after sputtering. The calcium to silicon ratio is about the same for all samples before sputtering which is explained by the fact that calcium is known to ride on top of silicon [8]. The AFM images show that there are valleys that probably reach down to the $CaF_2$ layer in the zero dose case, but not in the 1.0 $mC/cm^2$ case. Since this agrees well with the model explaining the XPS data, we conclude that the silicon almost covers the $CaF_2$ completely in the 1.0 $mC/cm^2$ case whereas the coverage is incomplete in the zero dose case.

At 10 $mC/cm^2$, the pre-sputter fluorine to silicon XPS peak ratio increased from the value at 1 $mC/cm^2$. Since we expect the fluorine to silicon ratio to decrease monotonically with increased electron dose in the absence of shadowing effects, the increase in the ratio must be due to less complete coverage. This is supported by the extraordinary islanding observed by AFM. At 50 $mC/cm^2$, the pre-sputter fluorine to silicon XPS peak ratio decreases. This is most likely due to the large electron dose having desorbed most of the fluorine.

## 3.7 Discussion: High temperature growth

We can explain the observed crystal shape and roughness with a simple model based on geometrical thermodynamics. In this model, the electron dose creates an ordered array of F-centers that increases the surface free energy, favoring lower contact angles and a smoother surface morphology. If one assumes that the growth process is close to thermodynamic equilibrium and that the shear stress is small near the interface, the surface morphology can be determined by two conditions. The first one is that the Helmholz surface free energy is minimized and the second one is the contact angle between the surface and the epilayer is determined by the force balance of the respective surface tensions [9]. The minimization condition determines the shape of the silicon islands and the contact angle force balance allows us to estimate the surface tensions of the interface and the irradiated $CaF_2$.

The measured surface free energies are approximately 1240 ergs/cm$^2$ and 450 ergs/cm$^2$ for Si(111) and $CaF_2$(111) respectively [18]. Thus, in the case of $CaF_2$ growth on silicon, the surface free energy is minimized by the $CaF_2$ covering the silicon in a 2D fashion. On the other hand, in the case of silicon growth on $CaF_2$, the free energy is minimized by 3D growth of the silicon on the $CaF_2$.

The shape of the resulting microcrystal in the high temperature growth is determined by the directional dependence of the surface free energy. Using the Wulff construction [9] in order to minimize the Helmholtz surface free energy, one finds that a silicon crystal should be bound by the $\{111\}$ and $\{100\}$ faces. However, the common crystal habit of silicon also shows $\{113\}$ faces (see figure 3.9a).

The presence of this face can be explained by a surface reconstruction lowering the energy of the $\{113\}$ surfaces [11]. Thus, we expect the shape of a silicon microcrystal on a (111) substrate to be hexagonal (see figure 3.9b). As one can see in figures 3.3 and 3.4, silicon does indeed form hexagonally shaped microcrystals when grown both on electron irradiated and nonirradiated $CaF_2$.

The contact angle (defined in figure 3.9c) between the microcrystal and the substrate is determined by the force balance at the bottom of the edge of the crystal,

$$\gamma_{e,v}(\theta)\cos\theta = \gamma_{s,v} - \gamma_{s,e}. \tag{3.1}$$

In the above equation $\gamma_{s,v}$ represents the free energy of the substrate/vacuum surface, $\gamma_{e,v}(\theta)$ is the free energy of the epilayer/vacuum surface, and $\gamma_{s,e}$ is the

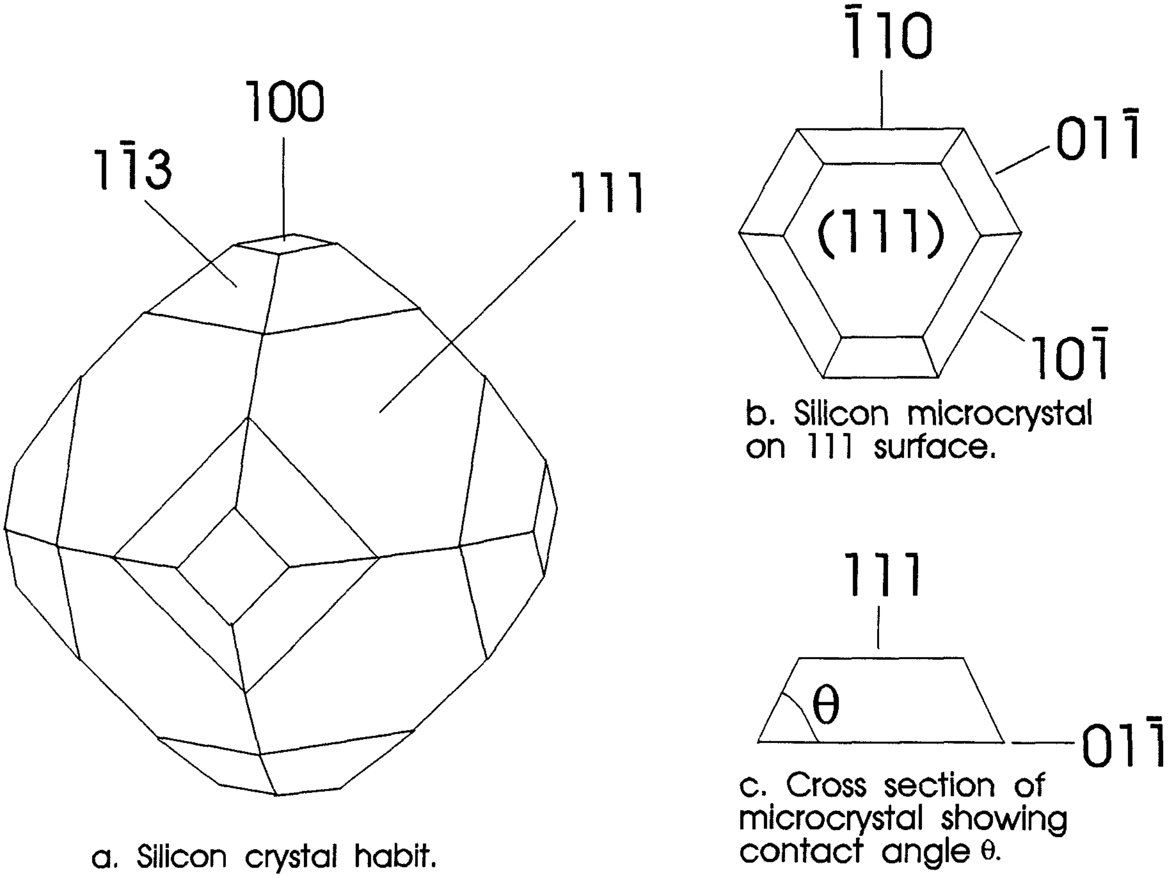

a. Silicon crystal habit.

b. Silicon microcrystal on 111 surface.

c. Cross section of microcrystal showing contact angle θ.

Figure 3.9: The silicon crystal. a) The crystal is bound by the three faces {113}, {111}, and {100}. b) The hexagonal microcrystal growing on a (111) surface. c) Definition of the contact angle between the microcrystal and the substrate.

free energy of the interface between the substrate and the epilayer. We approximate the silicon epilayer free energy as $\gamma_{e,v}(\theta) = \gamma_{111}\sin\theta + \gamma_{01\bar{1}}\cos\theta$, where $\gamma_{111}$ and $\gamma_{01\bar{1}}$ are the free energies of the (111) and (01$\bar{1}$) silicon surfaces respectively; by comparing the number of broken bonds on the surfaces, we find that $\gamma_{01\bar{1}} = \frac{4}{3}\gamma_{111}$. Note that we ignore any passivating effect that the "surfing" calcium might have on the silicon surface.

Using the free energies given above and the measured contact angle for the zero dose case, equation 3.1 yields an interface free energy of $\gamma_{s,e}$=-1100 ± 60 ergs/cm$^2$. Since the interface bonding has been determined to be dominated by the Si–Ca bonds [15], this implies that the Si–Ca bond energy at the interface is 2.5 ± 0.3 eV. This value is reasonable considering that a rough estimate based on the average of the Si–Si and Ca–Ca bond energies with corrections for the differences in electronegativity puts the Si–Ca bond energy at 2.6 eV [12]. If we interpret the lower contact angle in the 1.0 mC/cm$^2$ case as an increase in the surface free energy of the $CaF_2$ surface ($\gamma_{s,v}$) due to induced F-centers and assume that the the Si/$CaF_2$ interface free energy ($\gamma_{s,e}$) remains the same as in the zero dose case, then equation 3.1 yields an F-center $CaF_2$ surface free energy of 520 ± 95 ergs/cm$^2$. As expected, this energy is larger than the free energy of the normal $CaF_2$ surface. The large uncertainty in the free energy is due to the compounding of the substantial uncertainty in the measured contact angles.

## 3.8 Discussion: Low temperature growth

For the low temperature growth, it appears that the surface morphology smooths out with increasing electron dose and assumes the morphology of the underlying $CaF_2$ layer. A simple thermodynamic explanation, similar to the high temperature model, is that the unirradiated $CaF_2$ surface has too high a surface free energy for the Si to wet. Thus since the temperature is below epitaxial growth conditions for Si on $CaF_2$, the surface forms amorphous clusters. For the irradiated surface, the $CaF_2$ surface free energy is increased to the point that the subsequent Si layer wets the surface, thus leaving a morphology that closely resembles the underlying $CaF_2$ layer. A possible kinematic explanation is that the electron irradiation causes small surface defects that further reduces the mobility of the Si atoms. It should be noted that we did not see any evidence of surface damage from AFM micrographs upon irradiation of the $CaF_2$ surface. In the high temperature growths, the microscopic defects caused by the electron irradiation of the surface most likely did not significantly affect the surface mobility of the Si atoms. Thus for the high temperature growth, the surface mobility of the Si atoms was high enough for the surface to form equilibrium shaped crystalites, as observed. However, in the low temperature growths the surface mobility is high enough for the Si atoms to form clusters but too low to form equilibrium shapes. This is shown by the polycrystaline nature of the unirradiated sample in figure 3.5. So when the surface is irradiated, the defects generated by the electron dosage further reduced the surface mobility to the point that the Si atoms essentially stayed stationary at the point of impact with the surface. Thus, assuming a spatially homogeneous Si flux impinging on the surface, the subsequent Si layer will simply replicate the $CaF_2$ template.

Sasaki [8] thought that the increase in roughness of silicon epilayers on $CaF_2$ with increased silicon growth temperature was due to a chemical reaction between silicon and calcium. However, we observed that the roughness is smallest for an electron dose of 1 $mC/cm^2$. If a chemical reaction between the silicon and calcium was responsible for the 3D growth mode, one would expect the electron irradiated areas to be rougher due to the excess calcium available. Thus, the chemical reaction theory seems to be inconsistent with our experimental results whereas our simple model explains the data well.

## 3.9 Summary

These results indicate that electron beam assisted MBE does improve surface morphology for set range of dosages and temperatures. Evidence from AFM, LEED, XPS, and TEM supports the claim that a simple geometrical thermodynamic model can be used to explain the data. We have not attempted to optimize the parameters in search of a global minimum for surface roughness. Although these results indicate that it is currently impractical to manufacture devices that require thin smooth films of silicon on $CaF_2$, through electron irradiation of the $CaF_2$ surface there is some hope for this material system.

# Bibliography

[1] Leo J. Schowalter and Robert W. Fathauer, *CRC Critical Reviews in Solid State and Materials Sciences* **15** (4), 367-421 (1989).

[2] Seigo Kanemaru, Hiroshi Ishiwara, and Seijiro Furukawa, *J. Appl. Phys.* **63** (4), 1060 (1988).

[3] H.C. Lee, H. Ishiwara, S. Furukawa, K. Saiki, and A. Koma, *Applied Surface Science* **41/42**, 553 (1989).

[4] Kouji Miura, Kazuhiko Sugiura, and Hiroshi Sugiura, *Surface Science Letters* **253**, L407 (1991).

[5] V. Chakarian, T.D. Durbin, P.R. Varekamp, and J. A. Yarmoff (to be published).

[6] L. J. Schowalter, R. W. Fathhauer, F. A. Ponce, G. Anderson, and S. Hashimoto, *Material Research Society Symp. Proc.* **67**, 125 (1986).

[7] U.O. Karlsson, F.J. Himpsel, J.F. Morar, F.R. McFeely, D. Rieger, and J. A. Yarmoff, *Phys Rev B* **57**, 1247 (1986).

[8] M. Sasaki, H. Onoda, and N. Hirashita, *Mat. Res. Symp.* **53**, 149 (1986).

[9] J. Y. Tsao, *Materials Fundamentals of Molecular Beam Epitaxy*, (Academic Press Inc, New York, 1992), pp. 201.

[10] J.J. Gillman, *J. Appl. Phys.* **31**, 2208 (1960).

[11] Gunter A. Wolff, *Intermetallic Compounds* (John Wiley & Sons, Inc., New York, 1967), pp. 85.

[12] Linus Pauling, *General Chemistry* (Dover Publications, Inc., New York, 1988), pp. 912.

[13] Tanemasa Asano and Hiroshi Ishiwara, *J. Appl. Phys.* **55** (10), 3566 (1984).

# Chapter 4

# Observation of Transition from Schottky Barrier to thick Gap Device of ZnTe Surface using Scanning Tunneling Spectroscopy

## 4.1 Introduction

While the STM has been used to investigate a wide array of surface and bulk properties, one particularly important property for devices is the response of their surface to external fields. The nature of the surface states and particularly their density in energy is important for understanding the surface's response. Because of the STM's inherent design, it offers a unique opportunity to locally probe the surface states. The surface states have two roles; first, they represent local charge storage centers and affect the electrostatic potential of the sample. A large number of surface states will pin the surface Fermi level and screen the interior of the sample from external fields while a small number will allow the surface to accumulate, deplete, and even invert to adjust to changing external fields. Secondly, they also can act as generation-recombination centers for carriers. In this study we focus on the former effects. We find that the bias dependence of the spectroscopy is not consistent with the hypothesis that generation-recombination is a dominate current mechanism.

## 4.2 Determination of Surface Pinning by STM

Presently, there are three methods that have been developed for analyzing STM spectroscopy to determine the extent of Fermi level pinning. It is assumed that the surface state occupation is determined by the semiconductor's Fermi level position. One method involves the observation of an inflection point in the STM spectroscopy data that occurs at the band gap energy of the semiconductor surface [1] [2] (see figure 4.1). The cause of the inflection is the additional tunneling current from the dopant band in a near-degenerately doped semiconductor.

To clarify this point, consider a degenerately doped p-type semiconductor in a metal-insulator-semiconductor structure whose surface is in depletion when the structure is unbiased. That is, $\mathrm{W}_m < \chi_{sc} + E_{cf}$, where $\mathrm{W}_m$ is the metal workfunction, $\chi_{sc}$ is the semiconductor electron affinity, and $E_{cf}$ is the difference in energy between the semiconductor Fermi level and the conduction band edge. As one applies forward bias (see figure 4.1b), the unpinned surface will go from depletion to accumulation. Prior to strong accumulation, the tunneling current of holes from the semiconductor valence band into the metal can be appreciable if the doping level is near degenerate and the semiconductor band barrier is thin enough for holes to tunnel from the semiconductor to the metal tip. This represents the tunneling current before the inflection point. As the bias increases further, a new conduction path will appear of electrons tunneling from the tip into the semiconductor conduction band. This tunneling current represents the current after the inflection point. This feature implicitly demonstrates an unpinned surface since the surface must approach accumulation and be near flat band in order for the dopant tunneling

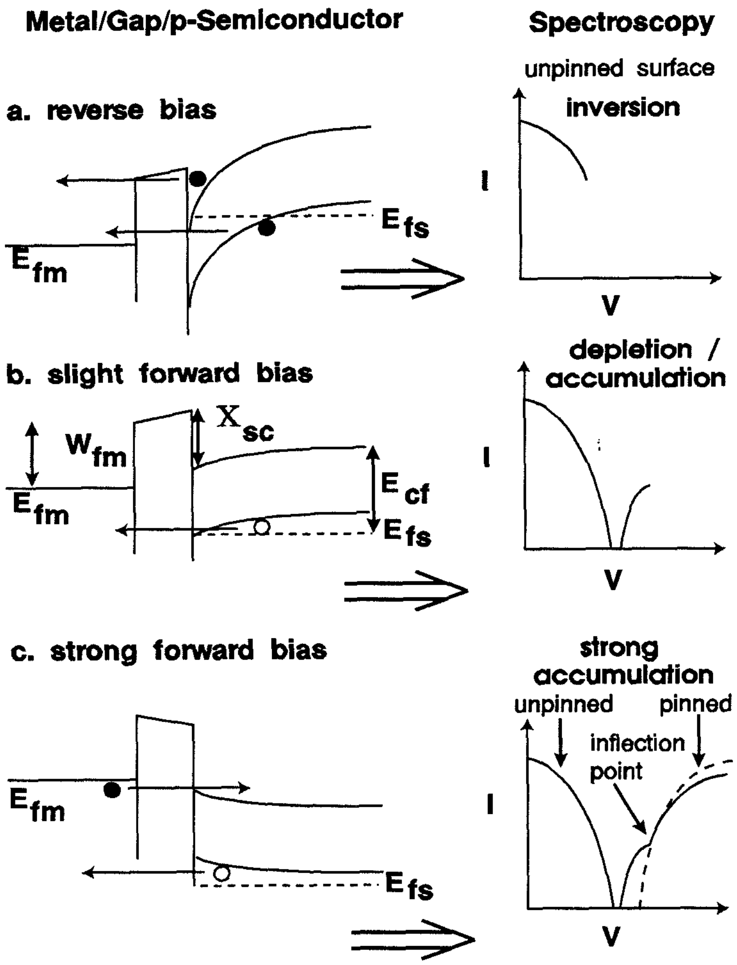

Figure 4.1: How unpinned semiconductor surfaces produce inflection points in STM spectroscopy

current to be measurable. Conversely, the pinned surface (shown in part in figure 4.1c) will stay in depletion and thus the valence band bending will block holes from tunneling into the metal. The drawback of this method is that the effect becomes weaker as the semiconductor doping decreases and is difficult to observe for doping levels less than $10^{18}$ cm$^{-3}$ [1].

A second method models the forward spectroscopy in terms of thermionic emission theory [3] (see figure 4.2). To apply this method, thermionic currents must dominate the other current mechanisms, including generation-recombination, diffusion, and thermionic-field emission. By assuming a simple expression for the thermionic current, $J = J_s[e^{(\Delta\phi_b(V,s)/KT)} - 1.0]$, one fits this expression to the data as a function of V, where $J_s$ is the saturation current, s is the tip-sample separation, and $\Delta\phi_b(V, s)$ is the lowering of the barrier due to the applied field [3]. $\Delta\phi_b(V, s)$ depends linearly on the separation and the applied field for an unpinned surface. A linear dependence of the log of the current to the applied field and separation confirms the surface is unpinned.

The drawback of this method is two fold. First, thermionic emission must dominate and second, one must be aware of other sources of field dependence on the current. For one, the saturation current is slightly field dependent through the Richardson constant. However, the barrier height dominates due to its exponential dependence [17]. There are generally two different field dependences of the barrier height, ignoring field penetration into the metal or metal wave function penetrations into the semiconductor [18]. The image potential correction, routinely used to approximate complex electron-electron interactions, is proportional to the square root of the field. Corrections to the potential in the gap region, on the other hand, depend linearly on applied field. A pinned surface only exhibits the image potential correction. A fit to the p-Si spectroscopy data in figure 4.2 showing a linear dependence in the field is evidence that the surface is unpinned.

The third method consists of plotting the differential conductance over the dc conductance as a function of applied voltage [4]. The current is measured as a

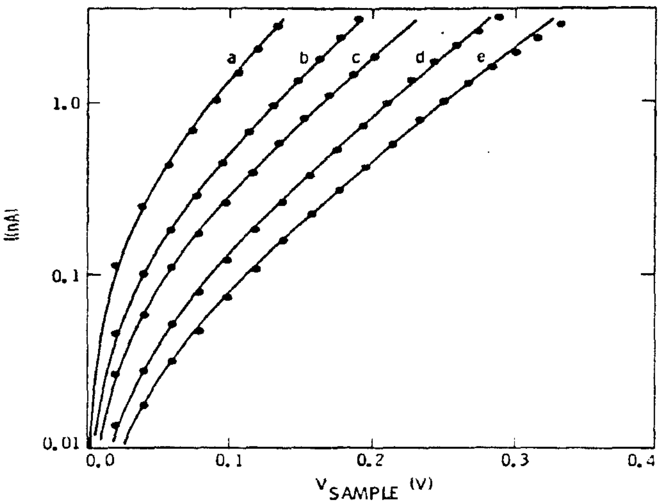

Figure 4.2: Thermionic theory fit to STM spectroscopy data by Kaiser et al., for forward biased unpinned p-Si surface, for tip-sample separations labeled a-e of 7.9, 9.2, 10.8, and 12.2 Å, respectively.

function of voltage while varying the tip-sample separation. A continuous linear ramp for the tip-sample separation is used, moving the tip toward the surface as the magnitude of the voltage is reduced. This yields a plot of a "normalized surface density of states" that is roughly independent of tip-sample separation . It can be used to determine the state density inside the semiconductor band gap region as well as the position of the band edges at zero bias. For typical tip-semiconductor separations the semiconductor should have "flatband" structure since nearly all of the potential drop will occur in the gap region. A lack of states inside the energy gap or lack of significant band bending implies an unpinned surface.

An example of the use of this technique used by Feenstra et al. is illustrated in figure 4.3 [4]. This figure represents a plot of the normalized conductance as a function of voltage for two different regions on a p-GaAs(110) surface with less than a monolayer of Sb deposited. One region is the edge of the Sb island and

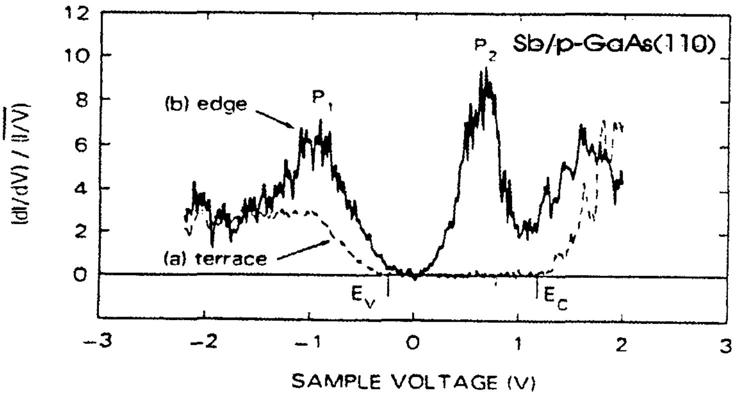

Figure 4.3: Example of the use of "normalized conductance" for interpreting STM spectroscopy of Sb deposited on a GaAs(110) surface.

the other is on the terrace of the island. From the edge data one can see a large number of surface states in the band gap that cause pinning of the Fermi level. The terrace data, although it does not show states in the gap, is also pinned. This is because the valence and conduction bands have shifted to the left about 0.4 eV relative to a clean (110) surface (not shown). This shift is due to surface states created by the Sb clusters.

This method has significant problems for wide bandgap materials because the ratio of the two conductances diverges near the band edges since the current becomes negligible at a finite rate. This can be remedied by "broading" (averaging I/V) over the bandgap in order to smooth out the diverges. For very wide bandgap materials, the features in the gap depends somewhat on the "broading" technique used as Martensson et al. has shown [5]. This problem aside, the above technique is unapplicable for the phenomena described in this paper, as we will show. This is due to the fact that the functionality of the transmission probability with gap separation prevent's this ratio from being scaled or "normalized" in such a straightforward and meaningful manner to extract the surface density of states.

We describe yet another technique for determining surface Fermi level pinning using STM spectroscopy. We show that for lightly doped materials, an enhancement of the reverse bias current as a function of gap separation can be observed and this effect can be used to show an absence of surface states in the energy gap. The enhancement effect can be shown to result from two competing tunneling mechanisms; tunneling through the tip-surface gap and tunneling through the semiconductor band-bending region. The dominate mechanism is determined by the magnitude of change in the band bending in the semiconductor as a function of voltage. This phenomena is sensitive to changes in workfunction differences between the tip and the semiconductor and to the doping level of the semiconductor.

## 4.3 Chapter Outline

The chapter's format is as follows; in the experimental section we discuss the details of the sample preparation of the ZnTe(110) surface, the experimental environment, and the measurement technique. The next section presents the spectroscopic data for small tip-sample separations and its agreement with thermionic emission theory. The following section presents spectroscopic data for larger tip-sample separations and compares the observed reverse bias current enhancement with theoretical predictions. The next section, we present the spectroscopy for the surface after exposure to contaminates (mostly oxygen and carbon) and show that the surface subsequently pins the Fermi level about midgap. In the final section we summarize the results.

## 4.4 Experiment

The material we studied is the cleaved (110) surface of p-type ZnTe. A II-VI semiconductor material with a wide band gap (2.26 eV), ZnTe has strong technological potential especially for electro/optical applications, including green and blue LEDs and lasers. In addition, ZnTe has been shown to alloy with HgTe and CdSe over the entire compositional range [7] for tailorable band gaps from 2.3 to 0.1 eV, making it a suitable material for infrared multi-spectral imaging. It is a convenient material to study since the material has a natural cleavage plane along the (110) direction and possesses a relatively inert surface as we have seen in our Auger and scanning tunneling spectroscopy surface studies. In addition, previous experimental and theoretical studies indicate that the clean (110) ZnTe is unpinned and free of surface states. Energy-loss spectroscopy by Ebina, Asano, and Takahashi [8] shows the absence of occupied surface states on the ZnTe (110) surface. This agrees with theoretical predictions using tight-binding models of Beres et al. [9] which predicts the absence of intrinsic surface states in the band gap of the (110) surface.

The samples consisted of intrinsic ZnTe with a typical doping of 1-2 x $10^{17}$ $cm^{-3}$. The doping levels were determined by standard Hall measurements. The crystal quality of the substrates varied as seen from X-ray rocking curves. A typical value for the rocking curve of undoped ZnTe is 54 arcseconds. A typical value we obtained for GaAs was 26 arcseconds, indicating nonstochiometries and defects in the ZnTe and the difficulty in obtaining high quality samples. An ohmic contact was made to each sample by evaporating $Sb_2Te_3$ on the rough side of the sample and annealing the sample in $H_2$:He at 200 °C for about one hour. The experiments were carried out in an inert atmosphere consisting of an argon filled Vacuum Atmosphere glove box with 0.3 micron HEPA filters. The unit is fitted with an alumina molecular sleeve to remove moisture and carbon dioxide, an alumina filter to remove oxygen, and a cold trap which removes any remaining condensible gases and hydrocarbons. The oxygen content is less than one ppm as determined by alumina oxide capacitance measurements and moisture content is less than 10 ppb as determined by lead fuel cell current measurements. The samples were freshly cleaved prior to each experiment. We have found from Auger spectroscopy and STM studies of ZnTe surfaces that the surface is relatively inert to gas absorption and contamination. Auger spectroscopy on ZnTe (110) surfaces etched for one minute in a 20:1 methonal:bromine etch and subsequently exposed to air for about 10 minutes shows a nominal oxygen and carbon coverage of 0.4 monolayers. This low level of reactivity is further supported by studies on similar materials that suggest that the partial pressure of oxygen and moisture need only be in the millitorr range in order to limit absorption to a point where the spectroscopy is unaffected [10].

A commercial scanning tunneling microscopy was used to carry out the investigation [6]. The spectroscopy was obtained by disconnecting the feedback loop, and ramping through the sample bias voltage while measuring the current at a constant tip-sample separation. Generally ten separate spectroscopy scans were averaged together.

Figure 4.4 shows an image of a freshly cleaved ZnTe surface acquired in the constant current mode. A single atomic step is shown in the image. The surface height has a standard deviation of about one angstrom over a 1000 x 1000 angstrom area. This standard deviation is about the same as other authors typically achieve on atomically flat H-passivated silicon for a similar area and is furthermore reasonable considering the normal relaxation distance between Te and Zn is about 0.5 angstroms on the surface [19, 1].

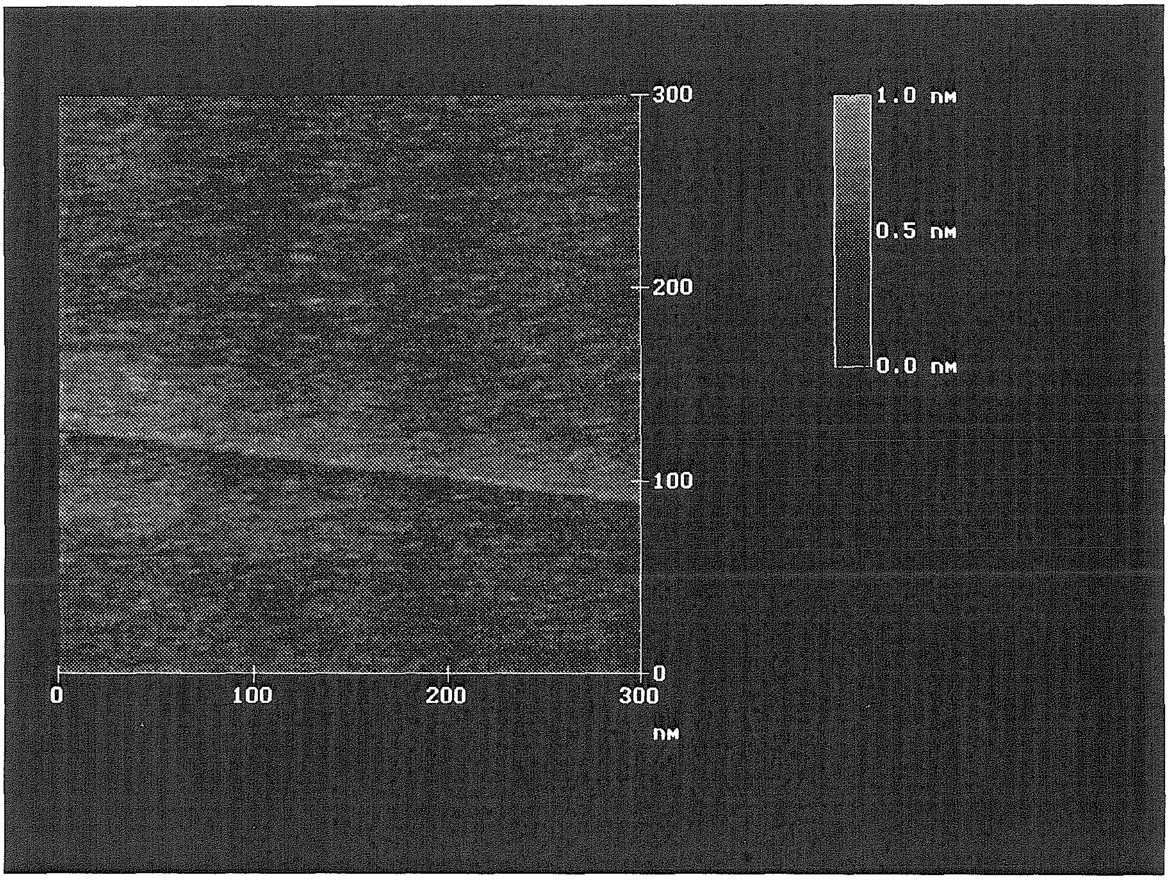

Figure 4.4: STM image of ZnTe(110) surface acquired in the constant current mode.

## 4.5 Data and Discussion for Small Tip-Sample Separations

### 4.5.1 Spectroscopy and the Thermionic Model

Prior to spectroscopy measurements, we deliberately dulled the tip to ensure adequate energy resolution and tip stability during spectroscopic measurements. The energy resolution may be limited due to the uncertainty principle applied to very small tips and the momentum of the electrons used in current transport, as we discussed in chapter one. We conditioned the tip by ramping the voltage up rapidly while maintaining the tip at a fixed close distance to the surface. Large currents result that other investigators have speculated cause the tip end to locally "melt" and form a large stable tip that is several hundred angstroms in radius [13].

From the observed functional dependence of the spectroscopy with the applied bias and for small tip-sample separations, we expected the current to follow either thermionic emission or diffusion theory. To test which model is most applicable, we use Bethe's criterion that states that thermionic emission will dominate when $d_l >> d_{kT}$, where $d_l$ is the mean free path of the carriers, and $d_{kT}$ is the distance over which the band changes by an amount kT. We note that $d_{kT} = kT/(qE_{max})$, where $E_{max}$ is the maximum field in the semiconductor. For a nondegenerate semiconductor we estimate $E_{max} = (2qN_aV_d/\epsilon_{sc})^{1/2}$, where $V_d$ is the band bending, $N_a$ is the doping, and $\epsilon_{sc}$ is the dielectric constant in the semiconductor. Near zero bias, $V_d$ is about 0.33 eV, $N_a = 1 \text{ x } 10^{17}$, and $\epsilon_{sc} = 9.6\epsilon_0$ where $\epsilon_0$ is the dielectric constant in vacuum. Thus $E_{max}$ is on the order of $10^5$ V/cm and $d_{kT}$ is on the order of $2.5 \text{ x } 10^{-7}$ cm. From the mobility at room temperature we estimate that $d_l$ is on the order of $10^{-6}$ cm. Thus $d_l >> d_{kT}$ and from Bethe's criterion we expect that thermionic emission should dominate the transport processes. A more reliable criterion is that of Berz et al. that states that $d_l > 5d_{kT}$ [14]. This criterion is not so well satisfied and so one must investigate the functionality of the fit more

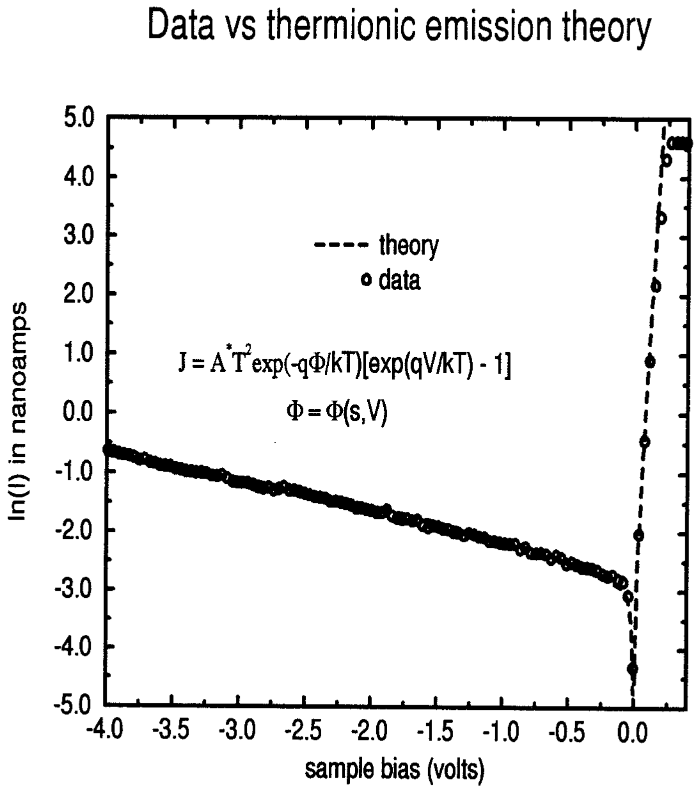

Figure 4.5: Spectroscopic data of ZnTe(110) surface with thermionic fit for small tip-sample separation.

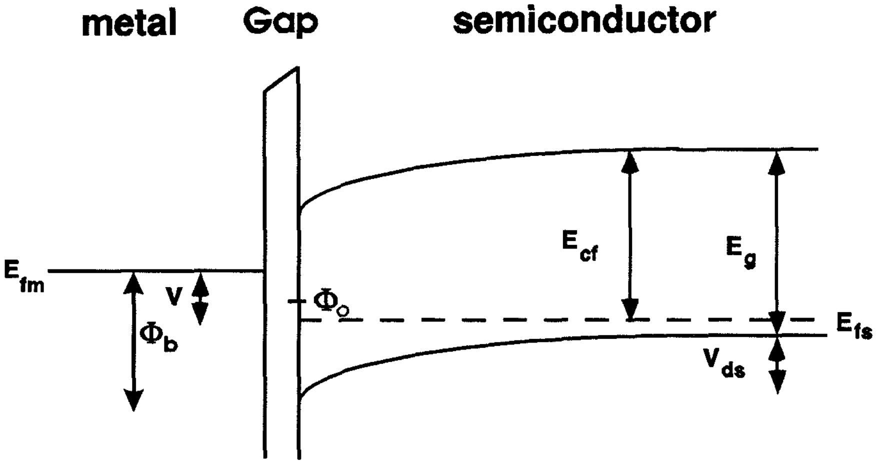

Figure 4.6: Energy band diagram for the thermionic model

closely to see which model is more strongly supported. We have found, along with other investigators, that the field dependence of the spectroscopy supports the thermionic emission model[23].

Figure 4.5 shows typical spectroscopy data acquired with a bias of -3.0 volts and a demanded current of 0.25 nA, along with a theoretical fit from thermionic emission theory. The bias and demanded current determine the tip-sample separation. From thermionic emission theory, the current should obey

$$J = A^{**}T^2 e^{(-q\phi_b/KT)}[e^{(qV/KT)} - 1.0], \tag{4.1}$$

where A** is the effective Richardson constant, $\phi_b$ is the barrier height, and T is the temperature [15]. The barrier height was calculated from $\phi_b$(V) = V + $E_g$ -($V_{ds}$ + $E_{cf}$) where $E_{cf}$ is the energy difference between the conduction band and the semiconductor Fermi level, $V_{ds}$ is the semiconductor band-bending energy (downward curvature is negative), V is the applied bias, and $\phi_b(0) = (\chi_{sc} + E_g) - W_m$, where $\chi_{sc}$ is the semiconductor electron affinity and $W_m$ is the tip work function. We use the values $\chi_{sc}$ = 3.5 eV, $W_m$ = 5.3 eV, $E_g$=2.26 eV, and $E_{cf}$ = 2.13 eV for $N_a$ = 1 x $10^{17}$. We ignore the image force corrections to $V_{ds}$ since the image force approximates electron-electron interactions only for distances larger than those used here. In addition, even if we were to insist on image force corrections, it is not apparent whether one should use the standard metal-semiconductor correction or the more complex metal-gap-semiconductor correction. In the former case $V_{ds}$ would be reduced with respect to its uncorrected value while in the later case, $V_{ds}$ is increased [21] [25].

For fitting parameters we used the gap separation and the effective area of the tip. The gap separation was used to calculate $V_{ds}$ using a one-dimensional double integration of Poisson's equation with full Fermi-Dirac statistics. $V_{ds}$ was then used to calculate $\phi_b$ and the current density. A gap distance of 2 angstroms was found to supply the best fit, leading to a lack of saturation for the reverse bias current. This "soft" reverse bias characteristic is the result of the potential dependence in the gap region, leading to a linear dependence of the barrier height with the applied field.

To see this dependence, we invoke the continuity of displacement current along with the following equations,

$$\epsilon_i E_i - \epsilon_s E_{sc} = Q_{ss} \tag{4.2}$$

$$W_m = V_i + \chi_{sc} + \phi_b \tag{4.3}$$

$$V_i = \delta E_i \tag{4.4}$$

$$Q_{ss} = qD_{ss}(\phi_b + \phi_o - E_g) \tag{4.5}$$

where $E_i$ and $E_{sc}$ are the electric fields in the gap and semiconductor surface, respectively, $\epsilon_i$ and $\epsilon_s$ are the dielectric constants for the gap and semiconductor region, respectively, $V_i$ is the potential drop in the gap region, $\delta$ is the gap region distance, and $Q_{ss}$ is the semiconductor surface charge which is a function of the surface density of states, $D_{ss}$. $\phi_o$, called the "neutral level", is a phemonological surface energy level for the semiconductor's Fermi level at which the surface is charge neutral. Solving these equations for $\phi_b$ yields

$$\phi_b = \lambda(W_m - \chi_{sc}) - \lambda\delta[(\epsilon_{sc}/\epsilon_i)E_{sc} + qD_{ss}(\phi_o - E_g)], \tag{4.6}$$

where $\lambda = (1 + qD_{ss}\delta)^{-1}$. If a surface is pinned, $\phi_b \approx E_g - \phi_o$, and thus the barrier height and the current is nearly independent of the applied field. However, for unpinned surfaces, $\phi_b \approx W_m - \chi_{sc} - \delta(\epsilon_{sc}/\epsilon_i)E_{sc}$ and one observes a linear dependence of the barrier height to the applied field.

The small gap distance from the fit confirms that tunneling is not the dominant mechanism. However, one might suspect that the tip may be in slight "contact" and may be modifying the surface. To test this hypothesis, we note that we do not see any surface modification from continuous scanning and that when we increase the size of the scan area to include the previously scanned region, we do not see signs of modification. In addition, since the current characteristics are reversible, we conclude that the tip does not modify the surface.

We have also fit the forward spectroscopy to the thermionic equation for various tip-sample separations (see figure 4.7). The experimentally measured tip height compares well with the calculated separation, as shown in the caption. However, it should be noted that the thermionic fit is relatively insensitive to changes in separation for these doping levels and hence does not represent a good test of the theory. This is because nearly all the voltage drop will occur in the semiconductor space charge region for a wide range of separations. This is indeed what we see in the spectroscopy as the ln(I) is nearly parallel for various separations.

From the fit we also estimated the area and radius of the tip. Using a simple spherical model for the tip (consistent with the model used in spreading resistance calculations, that is, area = $2\pi R^2$), we estimate an effective tip radius of about 50 nm. The droop in the current for strong forward bias is due to the spreading resistance. By fitting this region, we find the spreading resistance to be about 3 x $10^5$ ohms. If we assume the Maxwellian form for the spreading resistance (see figure 4.8 and chapter one for discussion), for the given doping level the tip radius is estimated to be greater than one hundred angstroms, consistent with the estimated tip radius of 50 nm from the thermionic fit.

We have also plotted ln[I/( $e^{(qV/KT)}$) - 1.0] vs V, from which the ideality factor

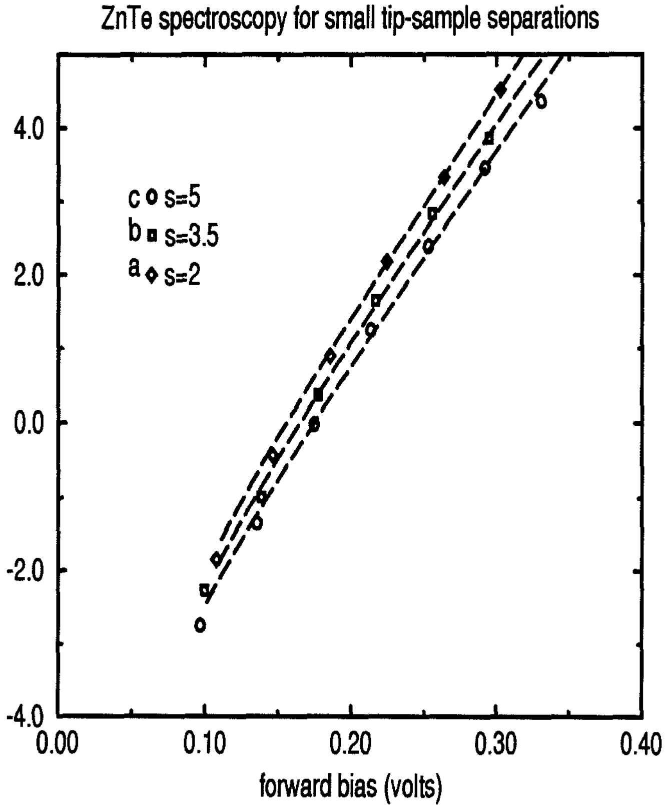

Figure 4.7: Thermionic fit to measured tip-sample separations (a-c) of 2, 2.9, and 3.9 angstroms. The thermionic fit parameters are 2, 3.5 and 5 angstroms, respectively

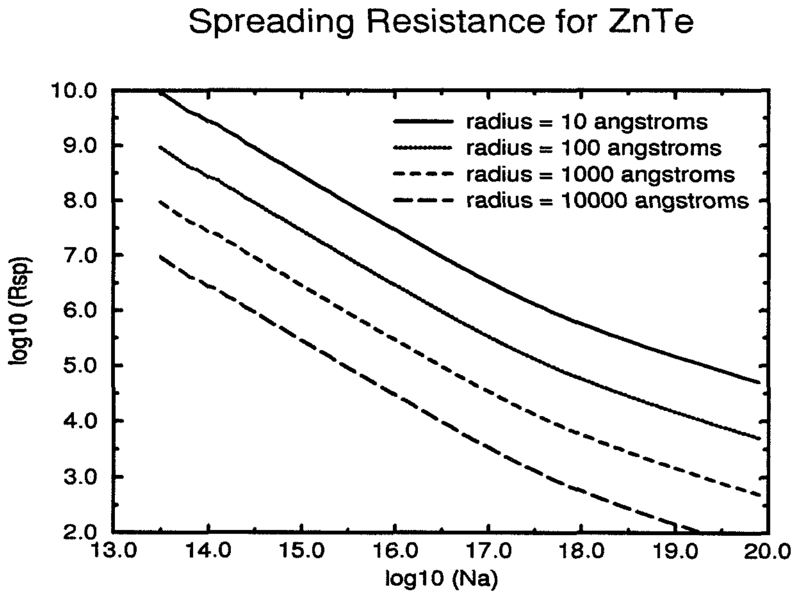

Figure 4.8: Maxwellian spreading resistances for various tip radii.

and saturation current were determined. The linear regression fit of the data shows excellent linearity over nearly four decades of current, indicating that the structure closely obeys thermionic emission theory. From the slope we determined the ideality factor to be 1.02, in which the deviations from one can be accounted for by possible image potential corrections. This value compares favorably to the results of Baker et al., who found ideality factors of about 1.09 and 1.15 for gold and nickel contacts on ZnTe, respectively [23]. The deviations from these previous studies have also been attributed to nonstochiometries in the sample which can cause generation-recombination and trapping processes to occur that increase the measured ideality factor [11].

### 4.5.2 Noninversion

From an inspection of the reverse bias current, it is apparent that the surface does not invert since the electron current from the semiconductor conduction band to the metal is negligible. This implies that the electron quasi-Fermi level follows the metal Fermi level as the bias changes. This is because the rate in which the semiconductor can supply minority carriers to the surface is much less than the rate in which carriers can tunnel from the surface to the metal. To illustrate this point, we can estimate the separation for when the tunneling current matches the semiconductor supply rate for minority carriers. To estimate the rate that the semiconductor can supply minority carriers, the electron current can be expressed in reverse bias as $J_{no} = J_{df} + J_{rg}$, where $J_{df}$ is the diffusion current and $J_{rg}$ is the generation-recombination current in the depletion region. From pn junction theory we find $J_{df} = (qD_n n_o)/L_n$ and $J_{rg} = (qn_i W)/t_e$, where $D_n$ is the diffusion coefficient, $L_n$ is the diffusion length, $n_o$ is the electron concentration in the bulk, $n_i$ is the intrinsic carrier concentration, $t_e$ is the recombination lifetime, and W is the depletion width, and we have assumed $n, p < n_i$ [12]. With a electron mobility of 330 $\text{cm}^2/\text{V}$ sec, recombination lifetime for electrons of $10^{-9}$ seconds, intrinsic concentration of of 0.4 $\text{cm}^{-3}$, and a depletion width of 0.1 microns, we find for ZnTe with $Na = 10^{17}$ $\text{cm}^{-3}$ that $D_n = 8.25$ $\text{cm}^2/\text{sec}$, $L_n = 9.08 \text{ x } 10^{-5}$ cm, $n_o = 1.6 \text{ x } 10^{-18}$ $\text{cm}^{-3}$, $J_{df} = 2.3 \text{ x } 10^{-32}$ $\text{A}/\text{cm}^2$, and $J_{rg} = 6.4 \text{ x } 10^{-16}$ $\text{A}/\text{cm}^2 \approx J_{no}$. To estimate the conduction band tunneling current, we use the approach of Card and Rhoderick adapted to electron minority carrier tunneling,

$$J_n = A^{**}T^2 e^{(-\alpha\chi^{1/2}s)} e^{((\phi_n - E_{fm})/KT)}[1.0 - e^{(-qV/KT)}], \tag{4.7}$$

where $\chi$ is the mean barrier height relative to the conduction band edge at the surface, $\alpha = 1.012$ $\mathring{A}eV^{1/2}$, T is the temperature in kelvin, $\phi_n$ is the quasi-Fermi level for electrons at the semiconductor surface, $A^{**}$ is the effective Richardson constant, and $E_{fm}$ is the metal Fermi level. This equation is much like the thermionic emission equation except for the $e^{(-\alpha\chi^{1/2}s)}$ term. Thus we see the current characteristics approach the thermionic limit as the gap and the barrier height decrease. If we require that the quasi-Fermi level change by 1 meV across the gap, and assume a free electron tunneling mass and a bias greater than a few KT, we obtain $J_n$

$= (1.08 \text{ x } 10^7)e^{(-\alpha\chi^{1/2}s)}\text{A/cm}^2$. To find the separation required for nonequilibrum conditions to be maintained in the semiconductor, we set $J_{no} = J_n$ and assume a typical gap barrier height for ZnTe of 3.5 eV. We find that s = 27 angstroms, a gap distance that ensures us that the semiconductor will always be in nonequilibrum conditions for small tip-sample separations.

## 4.6 Data and Discussion of Large Tip-Sample Separations

### 4.6.1 Spectroscopy

As the gap separation increases, we see from the previous equation that the current characteristics will become dominated by tunneling rather than thermionic emission. That is, as the separation increases, a transition occurs in which the structure's I/V characteristics change from that of an ideal Schottky barrier to a thick film MOS structure, in which tunneling then dominates. For semiconductor structures, the tunneling occurs through two different regions; tunneling through the gap between the tip and the semiconductor and tunneling through the semiconductor depletion region. The transmission probability through the depletion region increases with decreased band bending, and consequently, with larger gap distance if the surface is unpinned. These two competing mechanisms can actually cause an increase in the tunneling current with tip-sample separation when the structure is in reverse bias.

Figures 4.9a-d shows spectroscopy data that demonstrates this effect. The spectroscopy data was acquired with a demanded current of 0.2 nA and a sample bias of 1.2, 1.4, 2.0, and 2.5 volts, respectively, representing increasing tip-sample separation. Starting with figure 4.9a, in which the gap separation is smallest, the structure behaves as a near ideal Schottky barrier with low ideality factor. The reverse bias current in figure 3a clearly shows how effectively the carriers are blocked by the valence band bending in the semiconductor. The electron current from the semiconductor conduction band to the metal is negligible since the quasi-Fermi level for minority carriers (electrons) follows the metal Fermi level.

In figure 4.9b, as the gap separation increases, the forward bias current decreases while the reverse bias current increases due to a lower semiconductor band barrier for the holes. From figure 4.9b, we see that the decreased band bending has enhanced the tunneling probability.

In figure 4.9c, the gap separation has increased further so that the semiconductor bands are practically flat and the reverse bias current has reached a maximum. In figure 4.9a and b, the gap tunneling dominated the reverse bias characteristics but now any further increase in gap separation will cause the transmission probability to be gap-dominated and thus decrease monotonically with current.

In figure 4.9d, we see that the transmission probability and current characteristics are gap-dominated and the surface will start to follow equilibrium statistics for minority carrier. This phenomena clearly demonstrates in a new way the unpinned nature of the surface. Furthermore, the physics involved may be exploitable for the fabrication of very sensitive accelerometers or height detectors since the reverse bias as a function of separation is extremely sensitive.

An alternative possibility for this reverse bias enhancement of the current is that the tip simply could have drifted over a conductive region momentarily. To test this hypothesis, we measured the current vs. the separation for a given bias directly (see figure 4.10). From figure 4.10 we clearly see an increase in current with increasing separation, thus we can reject this hypothesis. We should mention that the tip had a tendency to crash into the surface while performing this measurement. It appeared that the reverse bias current enhancement disappears when the tip interacts with the surface.

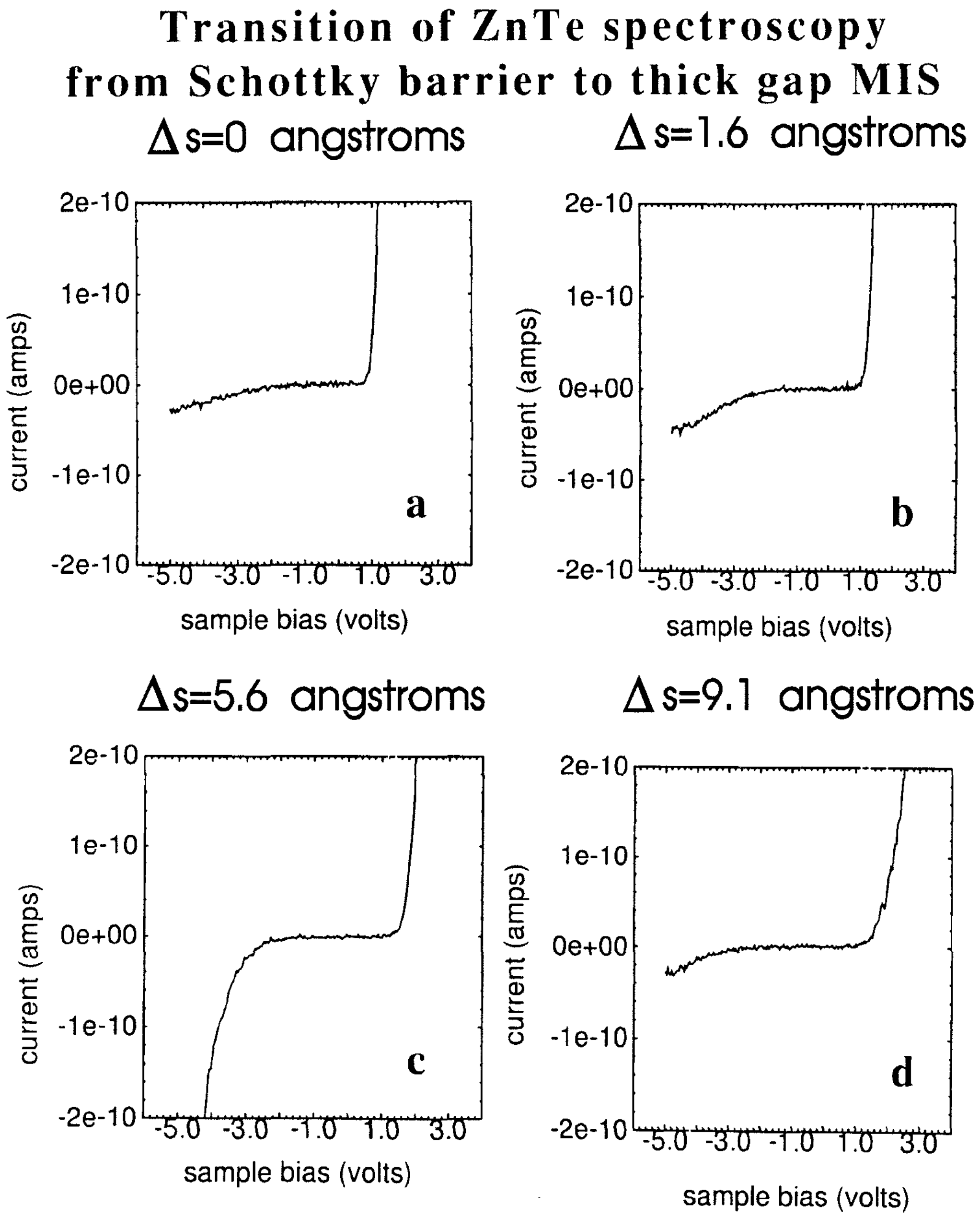

Figure 4.9: Spectroscopy with setpoint current of 200 pA for different tip-sample separations.

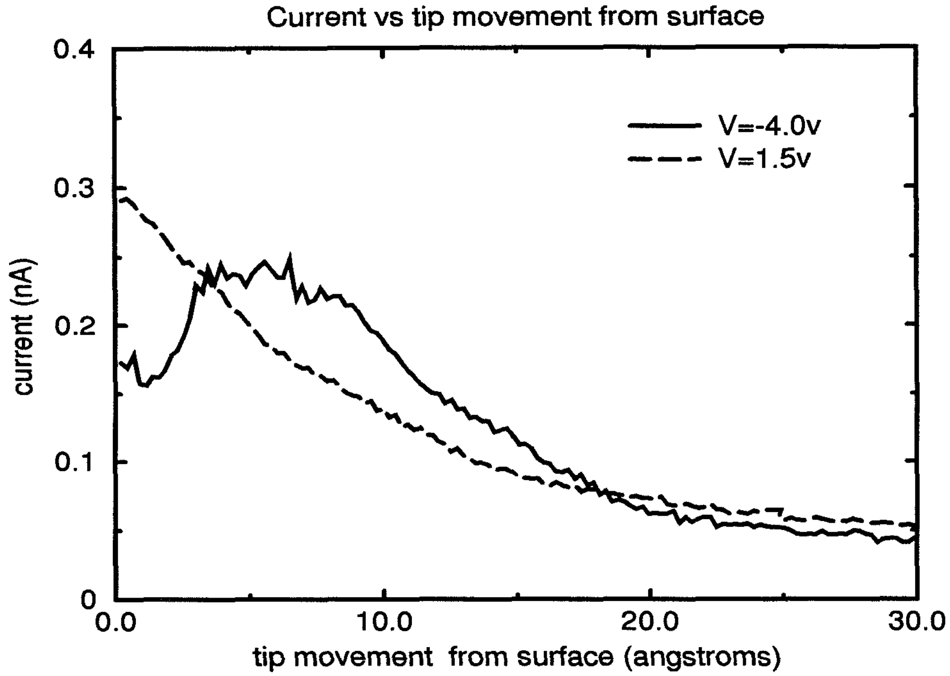

Figure 4.10: Current vs. separation for forward and reverse biases

### 4.6.2 Model

The simple model that explains this phenomena is illustrated in figure 4.11. Figure 4.11 shows the dependence of the semiconductor band-bending on the tip-sample separation for a metal-gap-ZnTe structure. For small tip-sample separations, most of the bias drop occurs in the semiconductor space charge region and so the bands of the semiconductor will swing significantly as the bias is changed. For strong reverse biases, the bands will block carriers from tunneling through the space charge region into the metal. For larger tip-sample separations a significant portion of the bias drops in the gap region, leading to smaller swings in the semiconductor bands as they respond to changing biases. In this case, the carriers can more easily tunnel through the space charge region and into the metal.

Figure 4.12 is a theoretical calculation of the reverse bias current and demon-

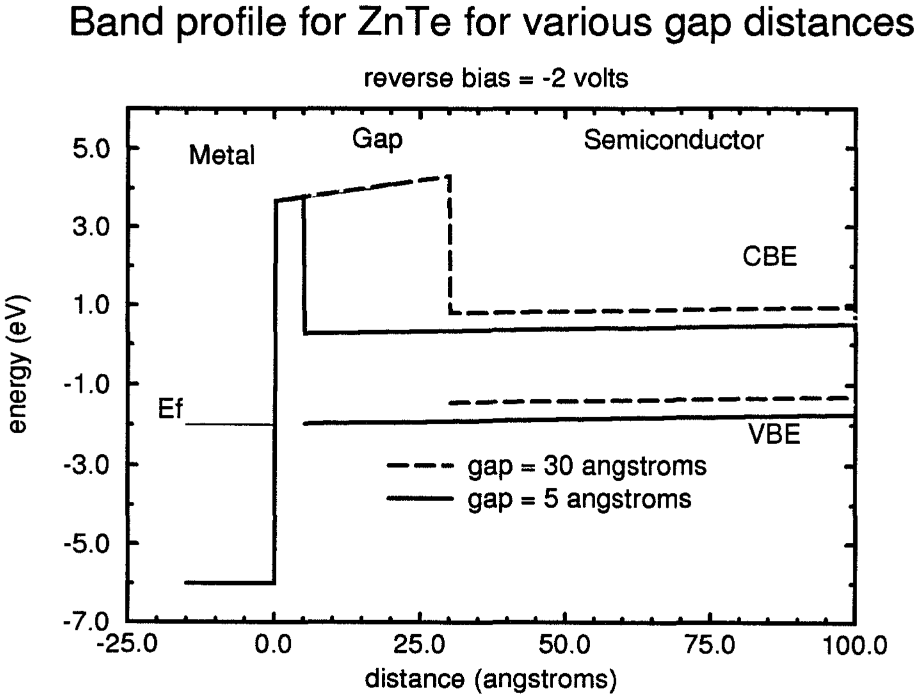

Figure 4.11: Energy bands of metal-gap-semiconductor structure for various bias voltages

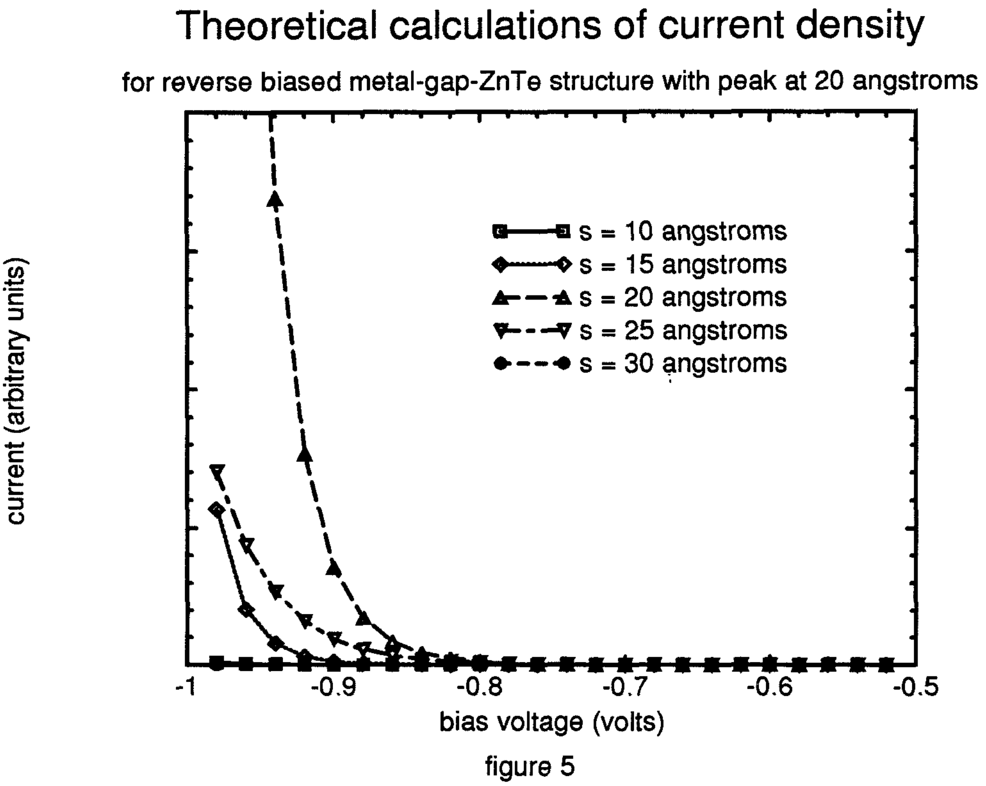

Figure 4.12: Theoretical spectroscopy curves for lightly doped large gap semiconductor structure discussed in text

strates qualitative agreement between the theory and the experimental data. The current was calculated following the formulation of Duke [24] in which the hole current can be expressed as

$$J_h = q\int_0^\infty T(E_z)[N_{tip}(E_z) - N_{sc}(E_z)]dE_z$$

where $E_z$ is the carrier energy perpendicular to the barrier, $T(E_z)$ is the transmission probability, and $N_{tip}$ and $N_{sc}$ are the supply functions of the tip and semiconductor, respectively. The integration of the Fermi functions in the tip and semiconductor over the parallel wavevectors is represented by the supply functions, given by

$$N_i = 2\pi m_i s(KT/h^3)ln[1.0 + e^{(E_{f_i}-E_z)/KT)}]$$

where i represents either the tip or semiconductor, $m_i$ is the respective effective mass, $E_{f_i}$ is the respective Fermi level, s is the spin degeneracy, and K,T and h are the usual constants. Details of the calculation can be found in Appendix A. From figure 4.12, we see that there is good qualitative agreement between the model and the spectroscopy data in figure 4.9a-d.

## 4.7 Data and Discussion for Contaminated Surface of ZnTe(110)

We also performed studies of the ZnTe surface after exposure to contaminates, especially oxygen, water, and carbon. Figure 4.13 shows the same cleaved surface as before except the surface has been exposed to 6.5 x $10^7$ langmuirs of oxygen, less than 6.5 x $10^5$ langmuirs of water, and an unknown amount of carbon, calculated from the partial pressures in the glove box and kinetic gas theory. The standard deviation of the surface height in the regions without visible particulates is 2.0 angstroms, indicating a certain roughing of the surface due to absorbates. The spectroscopy data, shown in figure 7, was taken at -3.0 volts bias with a demanded

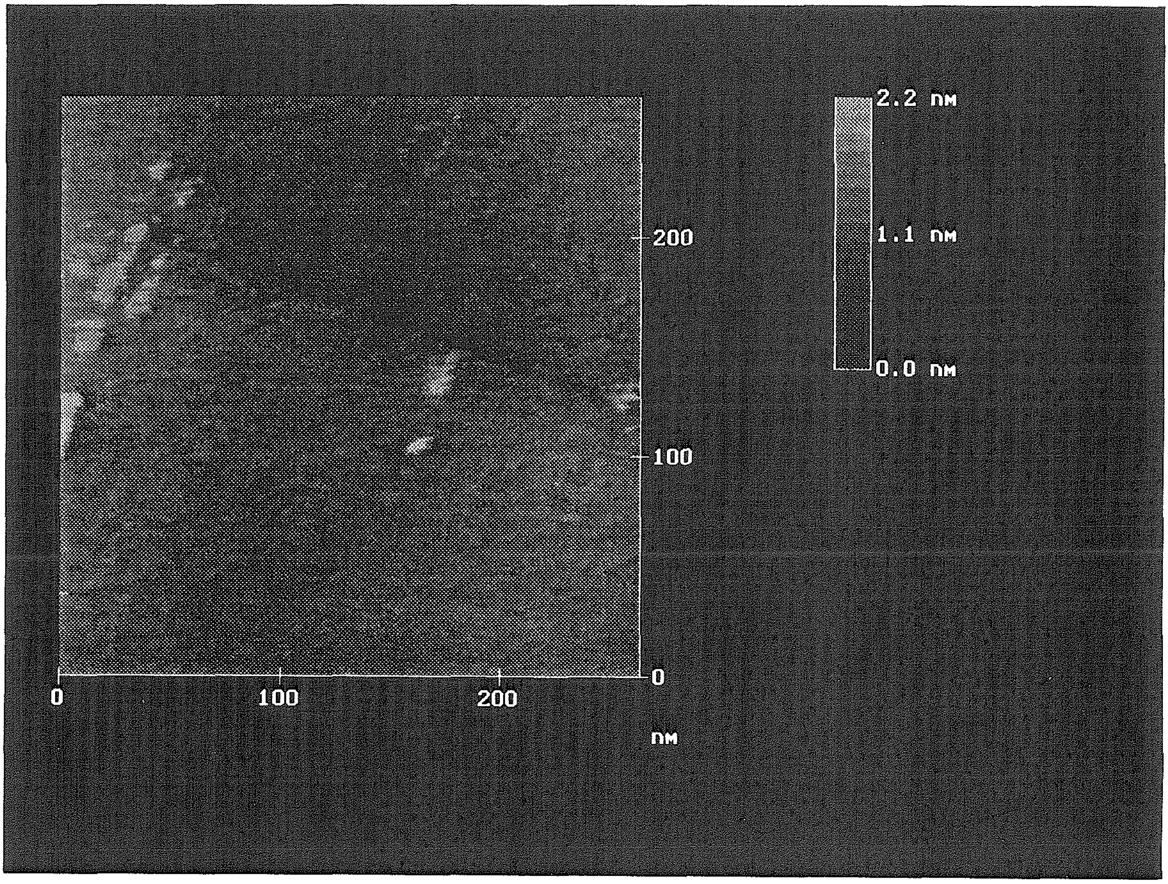

Figure 4.13: STM image of contaminated ZnTe(110) surface.

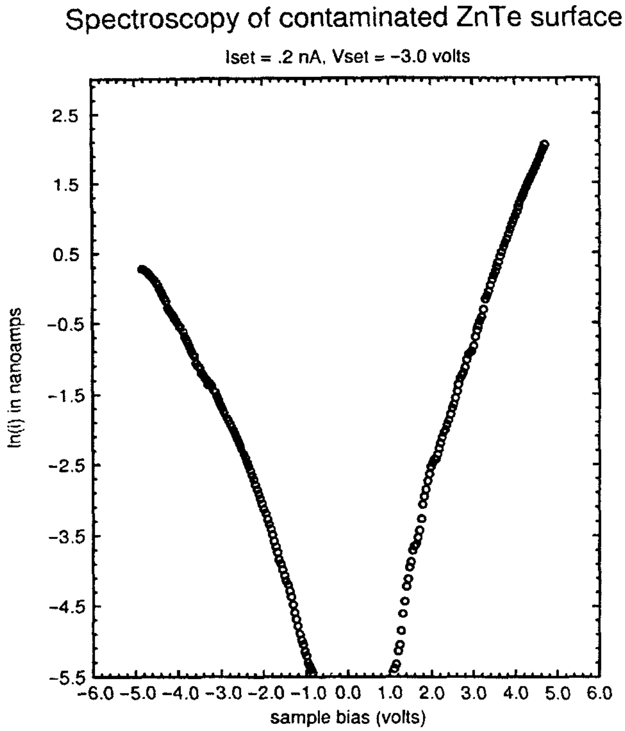

Figure 4.14: Spectroscopy of contaminated ZnTe(110) surface.

current of 0.2 nA. The spectroscopy, while not homogeneous across the whole sample, becomes increasingly more prevalent as exposure increases, indicating that the spectroscopy is due to absorbates on the surface. From the spectroscopy seen in figure 4.14, the surface appears to be pinned near midgap by the absorbates with a band gap of about 2 eV. Furthermore, the data exhibits neither the thermionic emission characteristics nor the reverse bias current enhancement of the freshly cleaved surface. We feel that the most likely cause of the pinning is oxygen absorption on the surface, which attaches strongly to the Zn and has caused similar effects on GaAs [2] [16].

To obtain a rough estimate of the percentage of surface coverage by contaminates, we can note that over a large area (about 500 x 500 $\AA^2$) scan of the surface, the distribution of pixel height of a clean surface from the constant current image scan is approximately gaussian about the mean pixel height. By fitting a gaussian distribution to the clean surface, we can extract the first through fourth moments of the distribution. These distributions are actually slightly leptokurtic, reflecting the atomically sharp features. In contrast, we see that for a contaminated surface (in areas without large visible particulates), the distribution is best fit with two gaussians, implying in the simplest approximation a distribution about the "clean" mean pixel height and the "contaminated" mean pixel height.

Fig. 4.15 shows the distributions for the clean and contaminated surface with the gaussian fits. To extract the percentage coverage of contaminates, we use two methods. In the first method, we simply divide the area of the contaminated gaussian by the total area of both gaussians and obtain a 27% surface coverage. For the second method, we subtract from the total area the area of a gaussian similar in all respects to the clean gaussian except scaled for the mean value, and divide by the total area. The percent coverage in this case is 36%. These numbers agree reasonable well with a 0.4 monolayer coverage of oxygen on similarily exposed etched ZnTe surfaces estimated by Auger analysis. Thus it appears that the surface coverage does not have to be 100% to pin the surface, consistent with studies on GaAs in which a large radius (4 angstroms) was found pinned around oxygen absorbates [4].

## 4.8 Summary

In summary, we have shown a new criterion to demonstrate the lack of surface pinning on the clean ZnTe (110) surface using STM. The mechanism involves the reverse bias current enhancement as the tip-sample separation increases over a certain range. There are potential device applications for this mechanism, par-

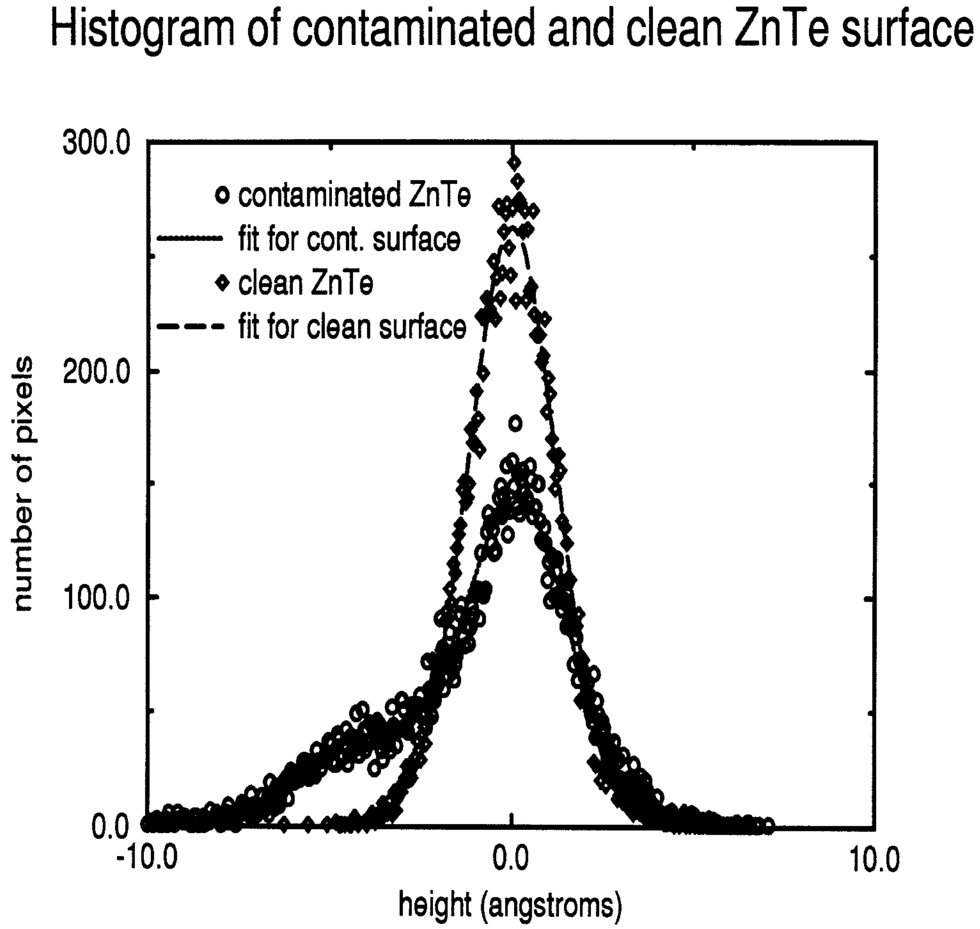

Figure 4.15: Histograms of pixels for clean and contaminated ZnTe(110) surface.

ticularly accelerometers or highly sensitive gap monitors. We also demonstrated that the spectroscopy is well explained by thermionic emission theory for small tip-sample separations. In addition, contamination (mostly oxygen and carbon) on the surface of cleaved ZnTe (110) pins the Fermi level about midgap with an energy gap of about 2.0 eV. The pinning mechanism appears to be similar to pinning of oxygen on GaAs, in that total coverage does not appear to be required to pin the surface.

# Bibliography

[1] M. B. Johnson and J. M. Halbout, *J. Vac. Sci. Technol.* **10**, 508 (1992).

[2] J. A. Dagata and W.Teng, *Appl. Phys. Lett.* **62**, 591 (1993).

[3] E. H. Rhoderick and R. H. Williams, *Metal-Semiconductor Contacts*, 2nd ed. (Oxford, New York, 1988).

[4] R. M. Feenstra, *STM and related methods*, (Norwell, Ma, 1990).

[5] P. Martensson and R. M. Feenstra, *Phys. Review B* **39**, 7744 (1989).

[6] Nanoscope III, Digital instruments, Santa Barbara Ca 93117.

[7] A.Sher, M. A. Berding, M. Van Schilfigaard, A. B. Chen, and R. Patrick, *J. Cryst. Growth* **86**, 15 (1988): S. N. Ekperuma and C. M. Myles, *J. Vac. Sci. Technol. A* **7**, 321 (1989).

[8] A. Ebina, T. Unno, Y. Suda, H. Koinuma, and T. Takahashi, *J. Vac. Sci. Technol.* **19**, 301(1981).

[9] R. P. Beres and R. E. Allen, *Physical Review B* **26**, 769(1982).

[10] D. A. Bonnel and G. S. Rohrer, *J. Vac. Sci. Technol.* **9**, 551(1991).

[11] D. P. Bortfeld and H. P. Kleinknecht, *J. Appl. Phys.* **39**, 6104 (1968).

[12] S. M. Sze, *Physics of Semiconductor Devices*, 2 ed.(John Wiley and Sons, New York, 1981).

[13] R. M. Feenstra, private communication.

[14] F. Berz, *Solid State Electron.* **28**, 1007(1985).

[15] S. Dushman, *Rev. Mod. Phys.* **2**, 381 (1930); F. Seitz, The Modern Theory of Solids p161 (McGraw-Hill, New York, 1940).

[16] J. A. Stroscio, R. M. Feenstra, and A. P. Fein, *Phys. Rev. Lett.* **58**,1668 (1987).

[17] C. R. Crowell and S. M. Sze, *Solid St. Electron.* **9**, 1035 (1969).

[18] J. M. Andrews and M. P. Lepselter, *Solid St. Elect.* **13**, 1011 (1970).

[19] M. H. Tsai, W. M. Hu, J. D. Dow, and O. F. Sankey, *J. Vac. Sci. Technol. A* **10**, 2511 (1992).

[20] W. J. Kaiser, L. D. Bell, M. H. Hecht, and F. J. Grunthaner, *J. Vac. Sci. Technol. A* **6**, 519 (1988).

[21] A. Tugulea and D. Dascalu, *J. Appl. Phys.* **56**, 2823 (1984).

[22] M. Kleefstra and G. C. Herman, *J. Appl. Phys.* **51**, 4923 (1980).

[23] W. D. Baker and A. G. Milnes, *J. Appl. Phys.* **43**, 5152 (1972).

[24] C. B. Duke, *Tunneling in Solids* (Academic, New York, 1969).

[25] D. Z. Ting, E. T. Yu, and T. C. McGill, *Phys. Rev. B* **45**, 3583(1992).

# Chapter 5

# Interface Studies and Ballistic Electron Emission Microscopy

## 5.1 Introduction

Interface studies and lateral inhomogeneities have been of intense technological interest over recent years. In particular, key characteristics such as carrier transport and electronic structure of both surface and subsurface interfaces determine the properties of many important semiconductor devices. In order to facilitate our studies of subsurface electrical properties, we have modified a commercial STM to perform Ballistic Electron Emission Microscopy (BEEM). Historically, BEEM has been used to study metal-semiconductor interfaces along with elastic and inelastic scattering mechanisms in thin metal layers. However, recently the technique has been extended to semiconductor-semiconductor interfaces [1][2]. We have attempted to extend these studies even further to study semiconductor-barrier-semiconductor structures.

As discussed briefly in chapter one, BEEM is a three-terminal modification of the two-terminal STM, where the additional connection is used to measure the current between the base and the collector(see figure 5.1). The base is normally a thin conductive layer from which ohmic contacts can be made with ease and also allows a significant fraction of electrons to travel through it without significant inelastic scattering. The collector, on the other hand, must form a substantial barrier to the base to eliminate near-zero voltage leakage currents while also supporting the formation of ohmic contacts.

## 5.2 Chapter Outline

This chapter has been organized as follows; first a review of the prevalent theoretical approaches for BEEM transport, followed by a study of Au/Si(100) structures and a preliminary study of InAs/AlAs/GaAs(100) structures. Each structure section will be further subdivided into discussions concerning sample preparation, surface and interface images, and local spectroscopy of the interface current with an interpretation of the data in light of current theoretical understanding. Detailed discussions of general sample preparation, BEEM construction and its operation can be found in Appendix B.

## 5.3 Theoretical Review

Prior to the presentation and interpretation of the data it is instructive to briefly discuss the two prevalent theories for BEEM transport. For simplicity, we will assume throughout that electrons cannot tunnel through the interface (Schottky) barrier but must have sufficient energy in the perpendicular direction to surmount it. We will also assume conservation of energy and transverse momentum across interfaces, which is equivalent to ignoring inelastic or elastic scattering along the interfaces. Furthermore, we will assume parabolic semiconductor band structure and free-electron dispersion in the tip. We will refer to figure 5.2 for the following theoretical discussions.

If we assume that there is little or no elastic scattering of the injected carriers

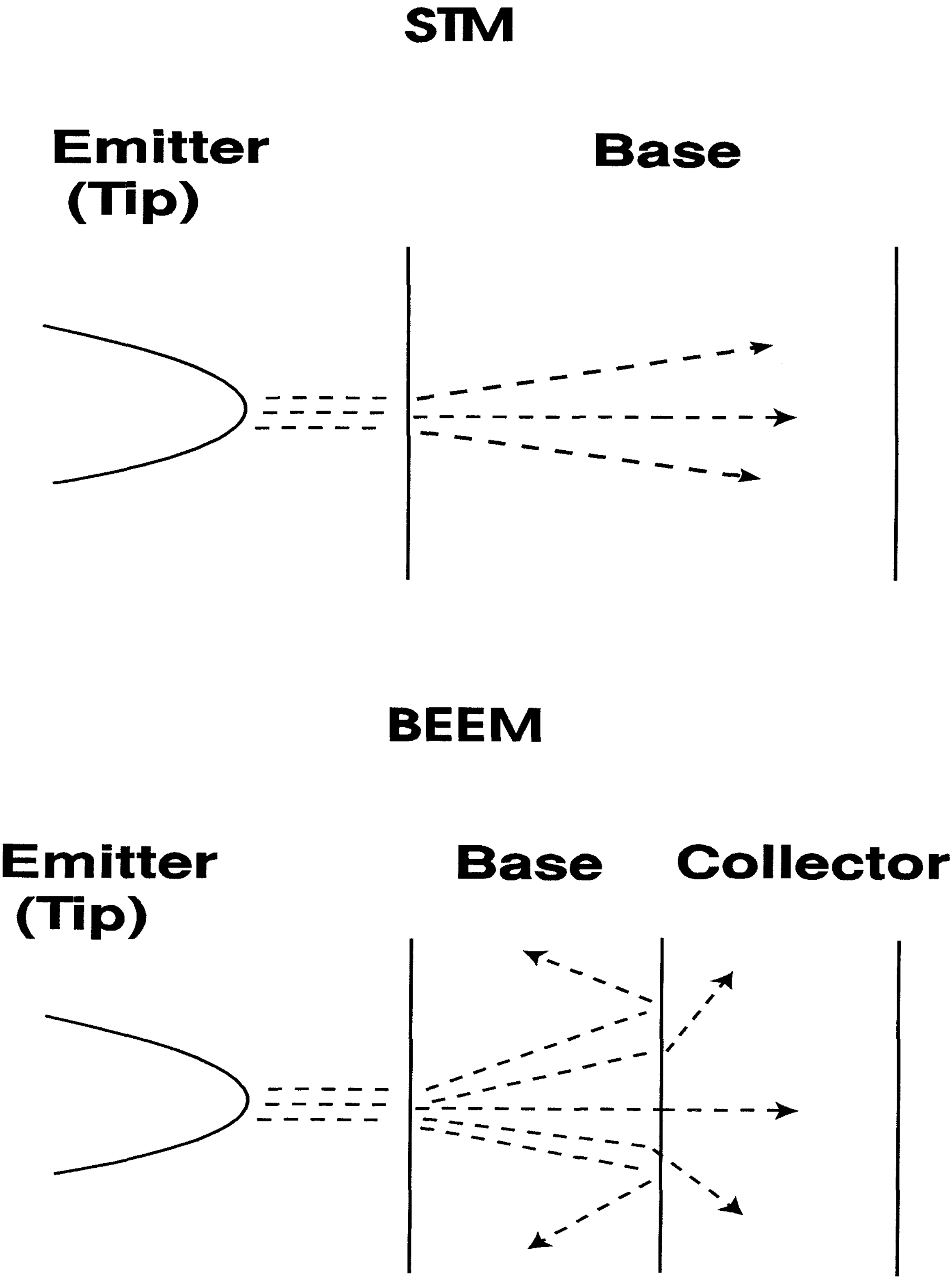

Figure 5.1: Comparison between Ballistic Electron Emission Microscopy and STM. Current in base is measured to set tip-sample separation while collector current measures interface properties.

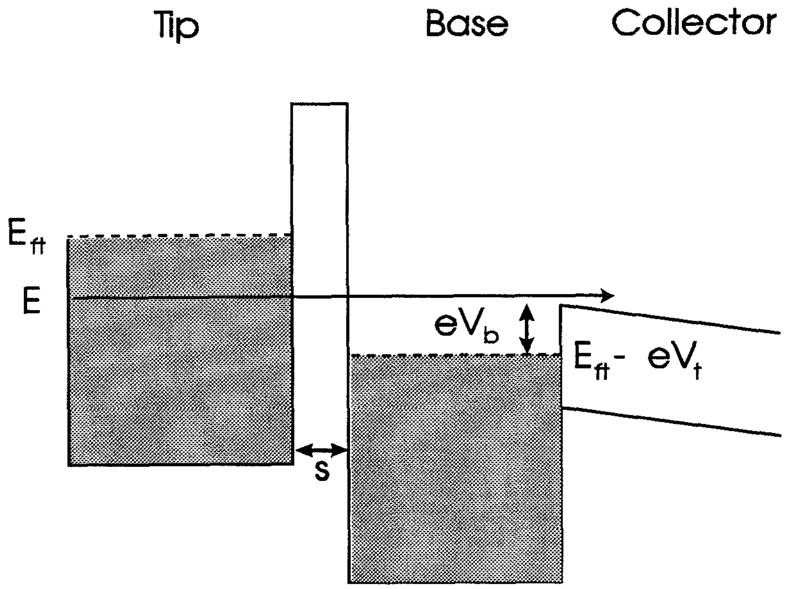

Figure 5.2: Basic band structure for theoretical review for BEEM transport

in the base region, then the distribution of electrons that needs to surmount the interface barrier is determined by the electron transmission probability across the tip-sample gap. Kaiser and Bell were the first to express these assumptions into what is now known as the KB theory [3] [4]:

$$I_{c_{bk}} = C \int_{E_{\perp_{min}}}^{\infty} dE_{\perp} T(E_{\perp}) \int_{0}^{E_{||_{max}}} dE_{||} f(E), \tag{5.1}$$

where C is a scaling factor, f(E) is the normal Fermi distribution in the tip, $E_{||}$ and $E_{\perp}$ are the energies associated with the parallel and perpendicular components of the momentum, and $T(E_{\perp})$ is the transmission probability across the tip-sample gap. In the above equation $E_{\perp_{min}}$ represents the minimum perpendicular energy that the carriers must possess in order to surmount the interface barriers and by conservation of energy is equal to $E_{ft} - e(|V_t| - V_b)$, where $E_{ft}$ is the Fermi level of the tip, $V_t$ is the applied bias, and $V_b$ is the barrier height at the interface. $E_{||_{max}} = [m_{||}/(m - m_{||})][E_{\perp} - E_{ft} + e(|V_t| - V_b)]$, where m and $m_{||}$ are the free electron mass and transverse mass in the semiconductor.

The form of $E_{||_{max}}$ is the result of both the conservation of energy and transverse momentum. To show this, one merely relates the carrier's momentum in the tip to the semiconductor by

$$\frac{\hbar^2 k_{||}^2}{2m} + \frac{\hbar^2 k_{\perp}^2}{2m} = \frac{\hbar^2 k_{||}^2}{2m_{||}} + \frac{\hbar^2 k_{\perp}^2}{2m_{\perp}}. \tag{5.2}$$

In the above equation, $k_{||}$ and $k_{\perp}$ correspond to the transverse and perpendicular momentums, respectively, and the first term on each side of the equation represents $\mathrm{E}_{||}$ while the second term represents $\mathrm{E}_{\perp}$. Because in general m > $\mathrm{m}_{||}$, the carriers will "refract" at the interface and some of $\mathrm{E}_{\perp}$ of the tip carriers will be converted to $\mathrm{E}_{||}$ in the semiconductor. Thus $\mathrm{E}_{||_{max}}$ is reached when all the *excess* $\mathrm{E}_{\perp}$ is converted to $\mathrm{E}_{||}$ and $\frac{\hbar^2 k_{\perp}^2}{2m_{\perp}} = 0$. The excess of $\mathrm{E}_{\perp}$ is simply $E_{\perp} - E_{\perp_{min}}$. Thus equation 5.2 becomes

$$E_{||_{max}} + (E_{\perp} - E_{\perp_{min}}) = (m/m_{||})E_{||_{max}}. \tag{5.3}$$

Rearranging terms yields $E_{||_{max}} = [m_t/(m - m_t)][E_{\perp} - E_{ft} + e(|V_t| - V_b)]$. In addition, one can also specify an "acceptance" cone or critical angle that the carriers must enter in phase space in order to surmount the interface barrier. This angle is simply

$$\begin{aligned} sin^2\Theta_c &= k_{||_{max}}^2/(k_{||_{max}}^2 + k_{\perp}^2) \\ &= (m_{||}/m)(|V_t| - V_b)/(E_{ft} + |V_t|). \end{aligned} \tag{5.4}$$

To facilitate interpretation of the data, it is desirable to find a simple analytical expression for the threshold collector current. Using the zero-temperature approximation, we find near threshold that $T(E_{\perp}) \approx T(E_{ft})$ and equation 5.1 reduces to

$$I_{c_{bk}} = CT(E_{ft}) \int_{E_{\perp_{min}}}^{E_{ft}} dE_{\perp} \int_{0}^{E_{||_{max}}} dE_{||}[1 - H(E_{||} + E_{\perp} - E_{ft})], \tag{5.5}$$

where H() is the Heaviside function. To solve this integral, one must recognize that the step function leads to two cases, $E_{||_{max}} > E_{ft} - E_{\perp}$ and $E_{||_{max}} < E_{ft} - E_{\perp}$. The transition between the two cases occurs when $E_{\perp} = E_{\perp_{max}} = E_{ft} - e(|V_t| -$

$V_b)(m_{||}/m)$. Thus equation 5.5 becomes

$$I_{c_{bk}} = CT(E_{ft})[\int_{E_{\perp_{min}}}^{E_{\perp_{max}}} E_{||_{max}} + \int_{E_{\perp_{max}}}^{E_{ft}} (E_{ft} - E_{\perp})]. \tag{5.6}$$

The final result upon integration is

$$I_{c_{bk}} = CT(E_{ft})e^2(|V_t| - V_b)^2(m_{||}/m). \tag{5.7}$$

Thus the collector current has a quadratic onset near $|V_t| \approx V_b$. It can further be shown that the quadratic onset is a general characteristic of any emission process that involves a source with a constant occupation density below a certain energy maximum and injects carriers into a medium with a parabolic band minimum.

To support the above conclusion, we can take an opposite view and assume that the injected carriers are totally randomized by elastic scattering in the base region. This model was first proposed by Lee and Schowalter (LS model) [5] and includes all the other assumptions of the BK theory. In this theory the form of the collector current is

$$I_{c_{ls}} = (C/2) \int \int dE_{||} dE_{\perp} f(E)[1 - cos\Theta_c(E)]T(E_{\perp}), \tag{5.8}$$

where the integral is bounded by $E > E_{ft} - e(|V_t| - V_b)$, that is electrons with only energies greater than the interface barrier get collected. $\Theta_c$ is the critical angle for collection and means that only carriers with energies that fall in this cone will be collected. Using similar assumptions in the previous derivation, one again arrives at a similar quadratic onset relationship. It should be noted that although the functionalities of the onset relationships are the same, $I_{c_{bk}}$ is greater than $I_{c_{ls}}$ by nearly two orders of magnitude for typical material parameters since the widen carrier distribution in the LS theory necessarily reduces the number of carriers that can be collected. We will use both the quadratic form and the complete BK theories to fit the Au/Si(100) data and extract Schottky barrier height information. Our data shows excellent agreement with the theoretical predictions while using only the barrier height $V_b$ and the constant C as adjustable parameters. Furthermore, we will exploit the quadratic onset to extract local band structure characteristics form the spectroscopic BEEM data of the InAs/AlAs/GaAs structure.

## 5.4 BEEM studies of Au/Si structures

### 5.4.1 Sample Description and Preparation

After the construction of the BEEM apparatus, we performed studies on Au/n-Si(100) structures in order to verify operation of the equipment and establish minimum signal-to-noise requirements. The Si substrates were phosphorous doped to 1 x $10^{15}$. The surface was prepared by first performing a RCA etch (consisting of TCE, acetone, methonal, and distilled water for two minutes each) to remove organics followed by a 2 minute etch in buffered HF and a distilled water dip. The sample, blown then with filtered nitrogen, should be hydrophobic. Au mesas with a diameter of about 0.8 mm were deposited to provide the interface with the substrate for investigation. The exact thickness of the Au mesas was unknown since the mini-evaporators lacked a thickness monitor. Through calibration measurements of depositing gold on glass and measuring the thickness with an alpha-stepper, we estimate the thickness to be approximately $250\pm150$ angstroms. The uncertainty is large since the gold forms large grains upon deposition. Following the gold deposition, a back contact of Al was made using mini-evaporators to form an ohmic contact. The quality of the ohmic back contact was verified by measuring the resistance between two Al dots using conventional iv measurements. The resistance was dominated by the sheet resistance of the Si substrate. In addition, we verified the quality of the Au/Si(100) Schottky barrier using the same measurement above except between a Au dot and an Al back contact. The results are shown in figure 5.3. It is important for accuracy to perform the iv measurements with a light shield since photoexcitation of the carriers in the metal and their transport into the semiconductor will yield erroneous data. Using the thermionic

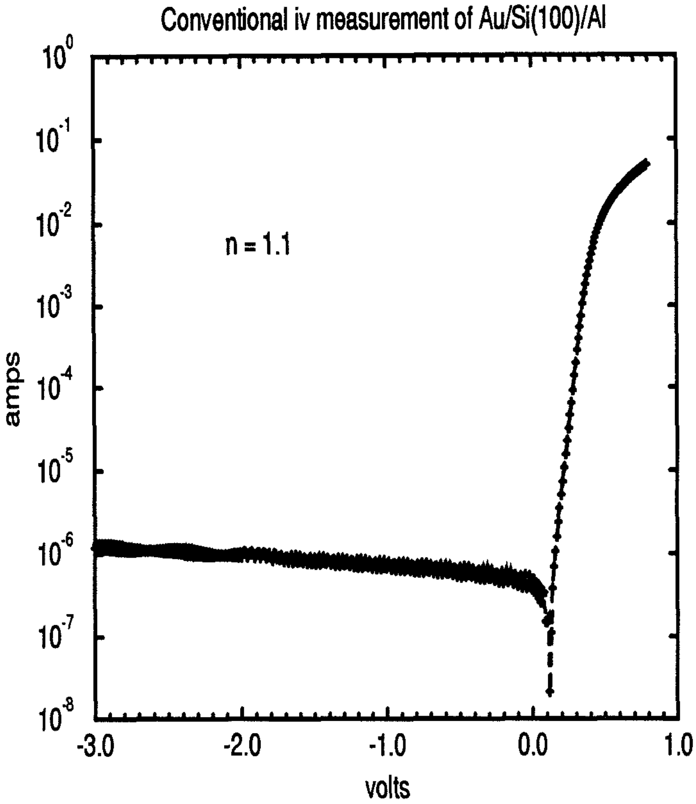

Figure 5.3: Conventional iv measurement of Au/Si(100)/Al taken using conventional contact techniques.

emission equation, we measure an ideality factor of about 1.1 and a barrier height of 0.74±.05 eV from figure 5.3. We also determined the barrier heights using cv measurements and found good agreement. The closeness of the measured barrier with the theoretical barrier height of 0.81 eV and the low ideality factor indicates an interface of good quality. It should be noted that Au interdiffuses into the Si substrate so that good interface characteristics last only about 8 hours. We found that by deliberately allowing a thin layer of $SiO_2$ to grow on the substrate prior to the deposition of Au, we can produce interfaces whose characteristics are stable for days. Finally the sample was mounted on a custom-built sample holder where a gold wire was used to contact the gold dot and silver paint was used to securely fix the back contact of the sample (collector region) to minimize vibrations.

### 5.4.2 Surface and Interface Images of Au/Si

Figure 5.4 shows the surface image of the gold mesas along with the corresponding Au/Si(100) interface simultaneously obtained in air. Feedback was used for the base current to maintain 1 nA at a voltage of -1.0 volts. The corresponding corrections to the piezos to maintain this setpoint generates the surface image. From figure 5.4 one can see the roughness due to the evaporation process along with the direct correlation of extreme features with the interface image. The RMS roughness of the surface is about 32 angstroms with a range of about 30 nm between high and low surface features. The evaporation process leads to the formation of large grains and extreme features that are tens of nanometers in height. Since the inelastic and elastic mean free path of carriers about 1 eV above the gold's Fermi level is roughly 120 nm and 10 nm, respectively, one expects significant increases in elastic and inelastic scattering of the carriers near these high features[6]. The increased scattering will tend to decrease the number of carriers that have sufficient energy to surmount the Schottky barrier and collect in the substrate. A comparison of figure 5.4a and 5.4b supports this hypothesis since the large features in figure 5.4a correspond to low collector current in 5.4b. It should be noted that this argument can still be challenged since the mean free path is energy dependent and has a significant uncertainty associated with it. The wavelike features seen in figure 5.4 are most likely due to inadequate vibration isolation of low frequency noise of the experimental apparatus. Figure 5.5 shows a top view of the same data in order to emphasize the grains and grain boundaries in the gold layer. A direct correspondence of these boundaries can be seen in both the surface and interface images. The boundaries appear as dark outlines in the surface image and correspond to light outlines (increased collector current) in the interface image. There are two possible explanations for the increase of collector current along the grain boundaries. One is that the grain boundaries represent a decrease in gold thickness so that carriers, since they scatter less, will have an increased probability of being collected. A second possibility is that the grain boundaries act as channels for carriers and hence one would see an increase of the collector current along these boundaries. It is unclear how powerful these arguments are since one could just as well postulate that grains should increase scattering due to surface imperfections, hence decreasing the collector current.

From the image we can investigate whether there is evidence of the "searchlight" effect. This effect can be observed when the surface has regions with large slopes (see figure 5.6). If one assumes that the electrons are transmitted from the region of the tip closest to the surface, then the electron distribution entering the base will possess momentum vectors that have large angles to the base-collector interface. This means that the electrons will possess a corresponding small component of perpendicular energy necessary to surmount the interface potential energy, *if* we assume that scattering is negligible. This effect manifests itself as a strong reduction in collector current at steeply sloped regions that do not show a strong dependence on base layer thickness.

To investigate this effect we compared the surface image and the interface image cross-sections taken at the same points. Figure 5.7 shows two such cross-

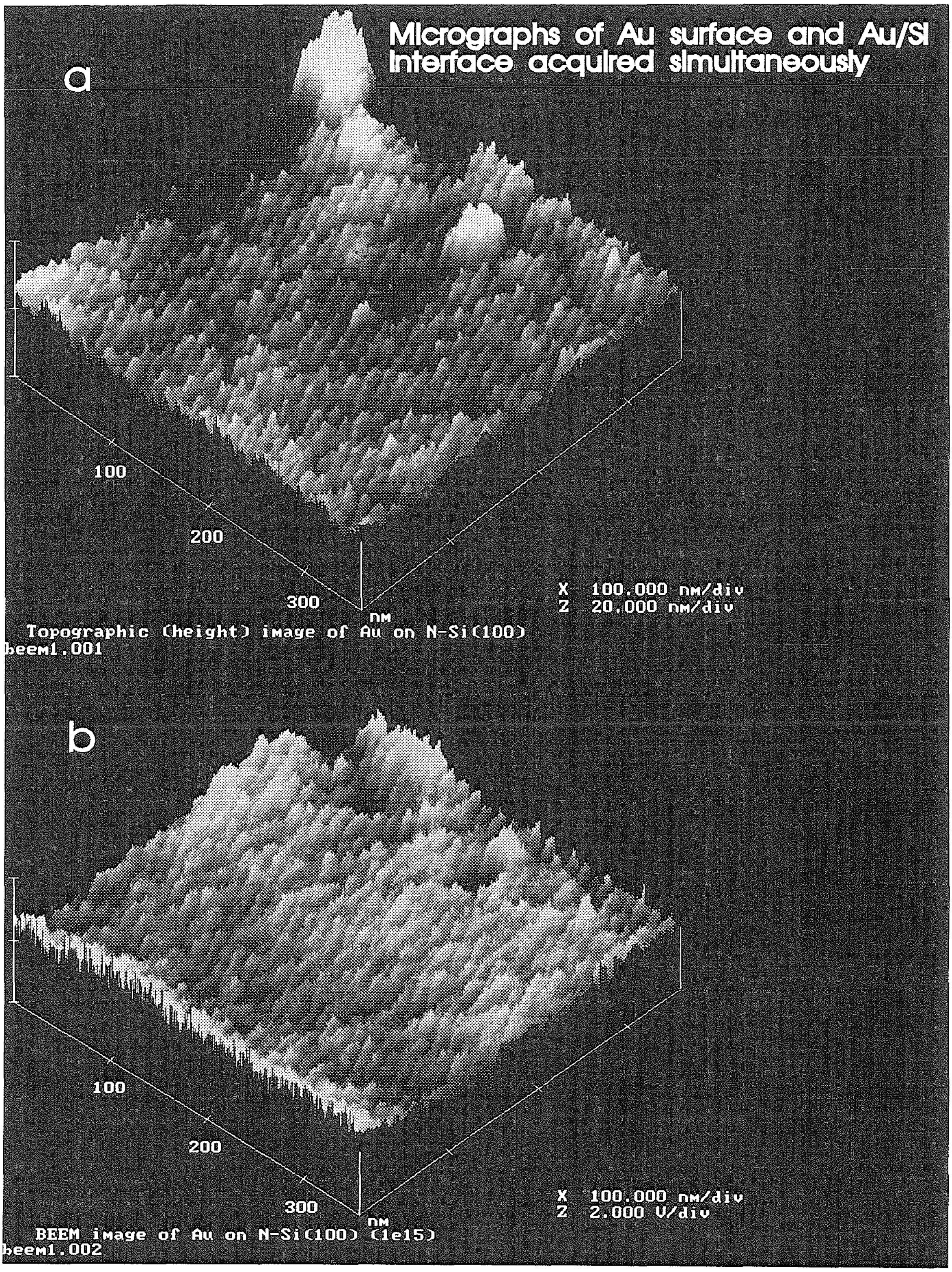

Figure 5.4: Side view of Au surface and Au/Si interface simultaneously acquired.

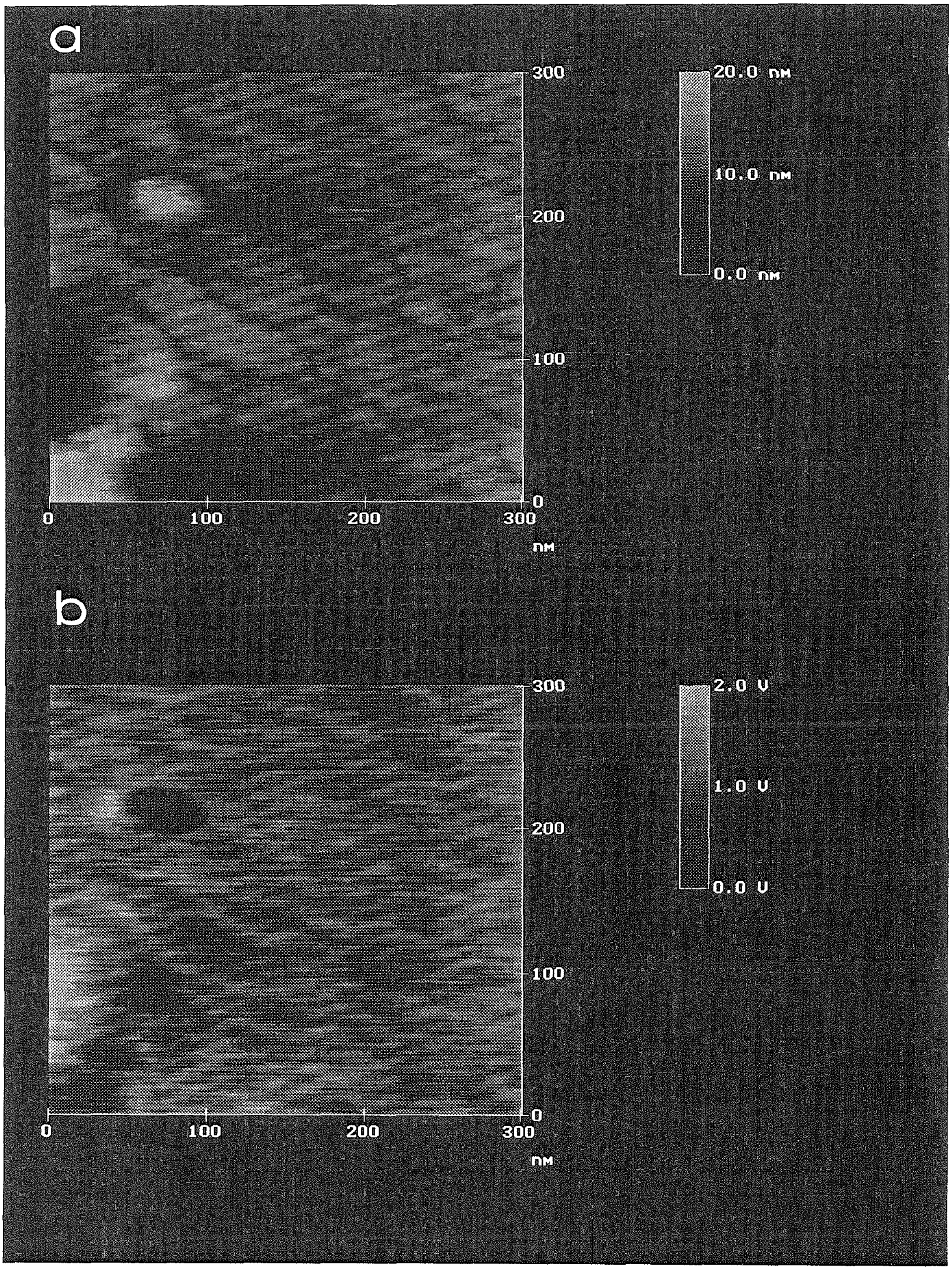

Figure 5.5: Top view of Au surface and Au/Si interface simultaneously acquired.

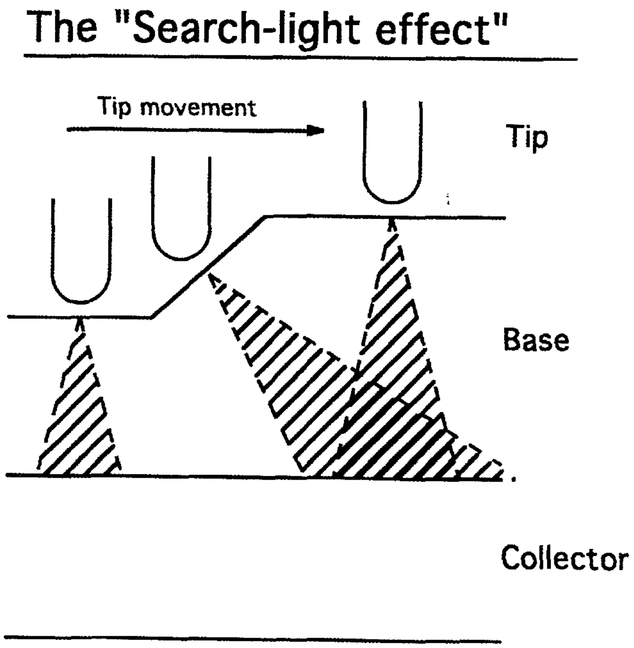

Figure 5.6: Illustration of mechanism behind “searchlight” effect

sections. The top line in each graph is the surface topography while the bottom is a measure of the collector current. The vertical lines show extreme regions in the surface topography with the corresponding BEEM current. In general there is a close negative correlation between the gold thickness and the collector current. This seems to indicate that either the increased inelastic scattering due to increased gold thickness is dominating any effects and/or elastic scattering is randomizing the electron distribution and minimizing the "searchlight" effect.

### 5.4.3 Collector Spectroscopy

The collector current should clearly show a turn-on voltage where the carriers injected from the tip have sufficient energy to surmount the Schottky barrier at the Au/Si(100) interface. To clarify our presentation of the data, figures 5.8 and 5.9 correspond to one location of the surface while figures 5.10 and 5.11 correspond to another. Figures 5.8 and 5.10 are BK theoretical fits to the spectroscopy while figures 5.9 and 5.11 represent fits using the quadratic function $(|V_t| - V_b)^2$. From figures 5.8 and 5.9 we see that the BK theory and the quadratic fit give similar fits, with the BK theoretical barrier height at 0.73 volts and the the quadratic fit yielding 0.65 volts. Most of the barrier heights we found are below the reported Schottky barrier heights on 0.81 volts of Au/Si. A possible explanation for this is the fact that gold readily diffuses into Si, and that this diffusion reduces the effective barrier height. Since we have to wait many hours in order to reduce thermal drifting of the tip over the surface, enough time transpires for diffusion to take place. Figures 5.10 and 5.11 demonstrates spectroscopic data where there appears to be two different barrier heights. Figure 5.10 shows a poor BK theoretical fit to the data with an extracted barrier height of 1.04 volts. Figure 5.11, on the other hand, shows the quadratic fit to two regions of the data and extracts barrier heights of 0.80 and 1.2 volts. We speculate that the larger barrier height is due to a thin layer of $SiO_2$ between the Si surface and the gold. Although

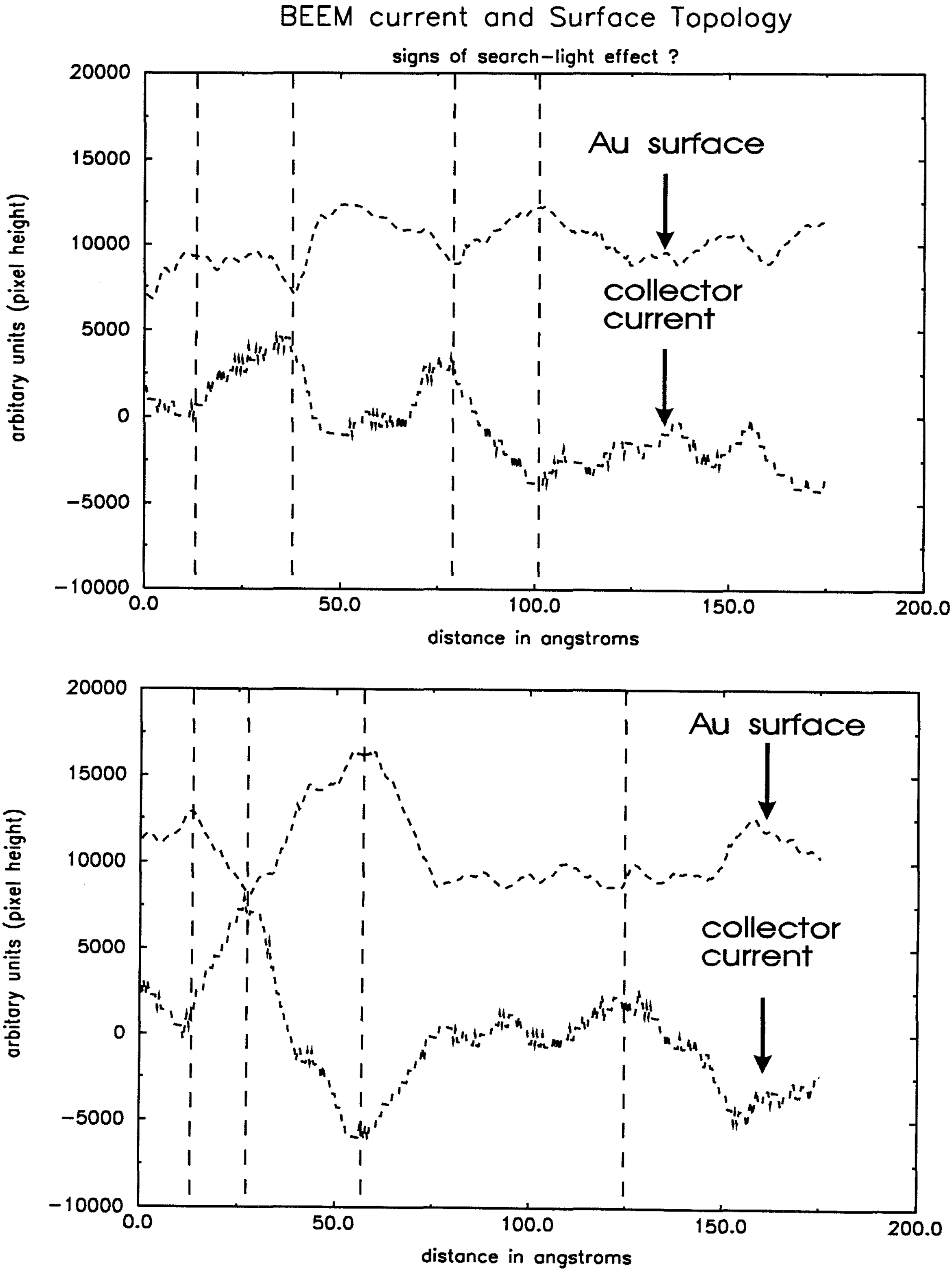

Figure 5.7: Cross sections of surface topography and collector current.

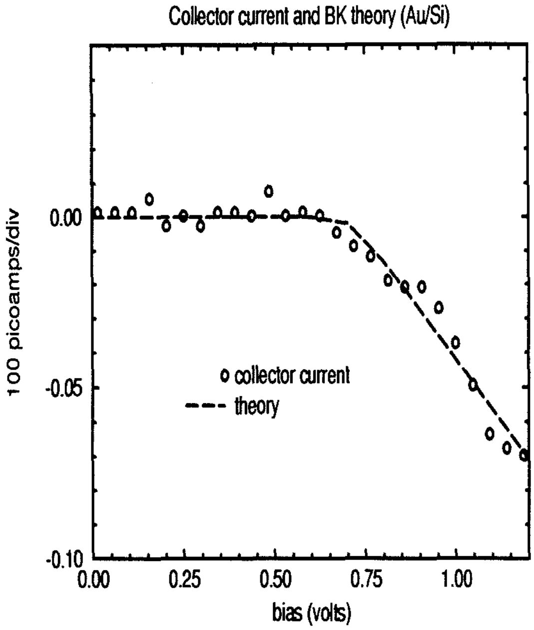

Figure 5.8: Collector current and fit to BK theory. Measured barrier height = 0.73 volts.

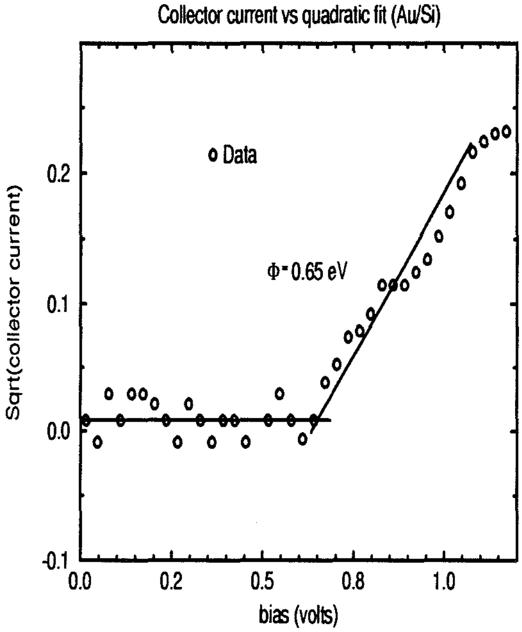

Figure 5.9: Collector current and fit to quadratic function. Vb = 0.65 volts.

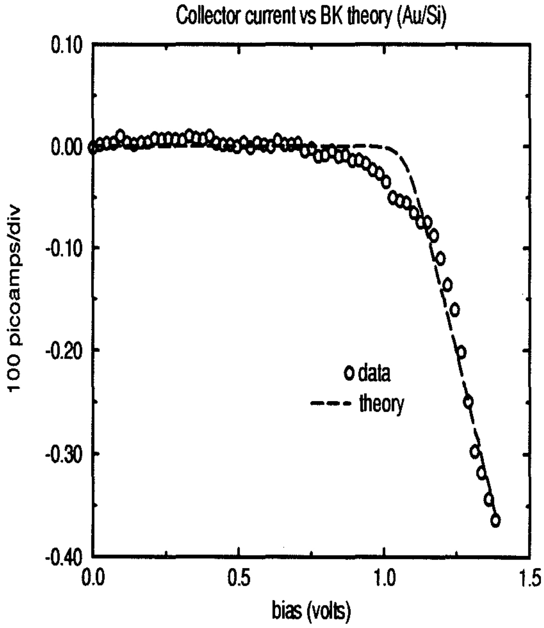

Figure 5.10: Collector current and fit to BK theory. Vb = 1.07 volts.

the Si surface was passivated with buffered HF, it was still exposed to atmosphere for up to 1/2 hour prior to the Au deposition. In addition, thermal drift as data was acquired means that the data represents some sort of spatial average over the surface. Figure 5.12 shows a frequency plot with bin size of 0.05 eV of measured barrier heights (using the quadratic fit) for 10 BEEM spectra. The sum of the frequency is greater than 10 since some spectra have two barrier heights. The large number of occurrences about 0.72-0.80 volts seems to verify the significance that the first onset represents transport over the Au/Si(100) Schottky barrier. The large number of occurrences near 1.2 volts seems to confirm that this effect is real and possibly corresponds to local oxide growth.

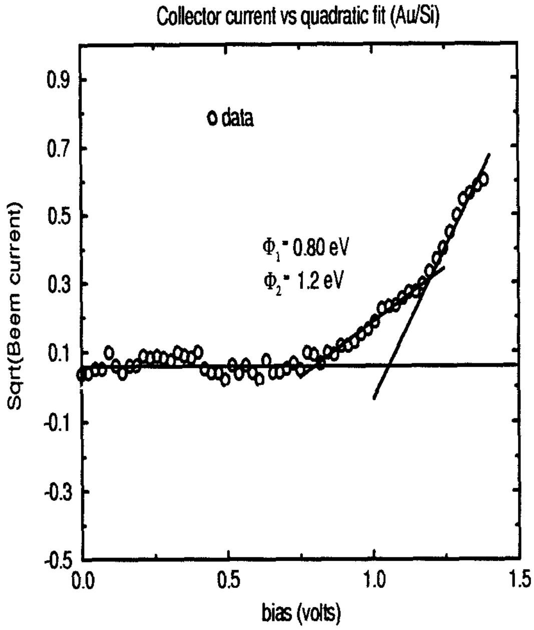

Figure 5.11: Collector current and fit to quadratic function. Vb = 0.8 and 1.2 volts.

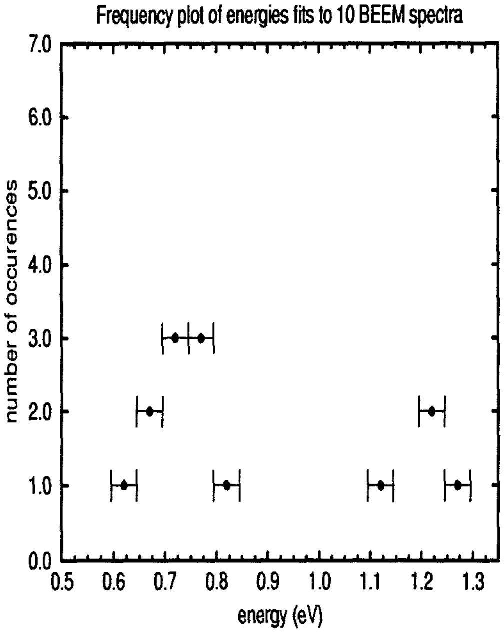

Figure 5.12: Histogram of BEEM spectra barrier heights

## 5.5 BEEM studies of Au/InAs/AlAs/GaAs structures

### 5.5.1 Sample Description and Preparation

In this section we will present preliminary studies of BEEM spectra of Au/InAs/AlAs/GaAs structures. It must be mentioned that the results are suggestive and that subsequent studies must be performed in order to verify the proposed hypotheses. The purpose of this study is to investigate the transport inhomogeneities in single barrier devices, particularly those associated with local band structure.

A cross-section of the structure is shown in figure 5.13. The InAs/AlAs/GaAs layers were grown by Molecular Beam Epitaxy (MBE). A thin buffer layer of lightly Si-doped GaAs was first grown on lightly n-doped GaAs(100) substrate, followed by the growth of 100 angstroms of lightly Si-doped AlAs and then 100 angstroms of Si-doped InAs. The InAs was doped to approximately $10^{19}$ cm$^{-3}$ while the AlAs and GaAs were doped below $10^{17}$ cm$^{-3}$. A thickness of 100 angstroms was chosen for the AlAs in order to provide a sufficient barrier to carriers to reduce spurious currents near zero-bias conditions of the device. This is necessary to ensure an adequate signal-to-noise ratio under experimental conditions. The InAs was deposited on top of the AlAs to provide a well defined and well characterized interface with the AlAs and to form a highly conductive surface to tunnel to (since its surface is pinned in the conduction band).

We initially performed BEEM experiments without the Au layer and found that the experiments were hindered by two effects. First, the surface appeared rough with surface features tens of angstroms high, possibly due to selective oxide growth. This contributed to unstable behavior of the spectra during data acquisition. Secondly, we noticed gradual turn-on characteristics in the spectra that indicated slight biasing across the device. Thus we decided to deposit Au onto

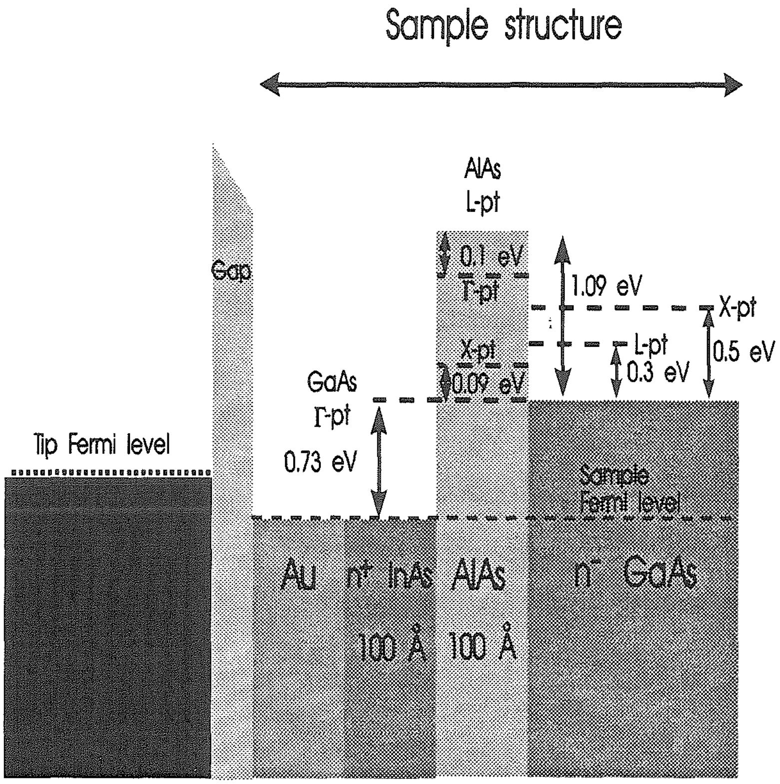

Figure 5.13: Cross-section of Au/InAs/AlAs/GaAs structure

the InAs in order to shield the sample from the external fields of the tip and also to provide an inert surface in which to tunnel to. Consequently, the sample was exposed briefly to air before a thin Au mesa approximately 0.8 mm in diameter was deposited on top of the InAs using mini-evaporators. This exposure may still cause oxides to form on the InAs prior to Au deposition. The thickness of the Au is between 100-400 angstroms according to previous calibration runs. The contact to the GaAs substrate was made by melting In to the backside of the wafer (used in the MBE process to adhere the sample to the transfer block). The top Au layer was grounded through contact with a Au wire. As before with Au/Si, the Au deposited by the mini-evaporators formed large grains that dominate the surface and interface images. Thus it is not instructive to investigate the interface images at this time until the deposition process can be better controlled.

In order to characterize the structure we performed conventional iv measurements and performed a band bending calculation in order to simulate the probable band structure. The calculations were made by performing a double integration of Poisson's equation using full Fermi statistics with the assumption that the InAs layer extends until flat-band conditions are reached. For the iv measurements, contacts were made directly to the In backcontact and the top InAs layer. Figure 5.14 shows the results of the measurement. From a fit to the current onset at about 0.5 eV to the thermionic emission equation we extract a barrier height of $0.632\pm0.015$ volts. If we compare this to figure 5.15 we see that the barrier height at the GaAs/AlAs interface with band bending is about 0.5 eV, showing that the observed onset current corresponds well to the band bending calculation. The fact that the InAs surface is only 100 angstroms thick means that flat-band conditions in the InAs will not be reached and will cause additional band-bending above our estimated value. From figure 5.14 the calculated zero-bias resistance is about 1 Mohm, high enough so that the collector current signal to noise will be adequate to permit BEEM experiments.

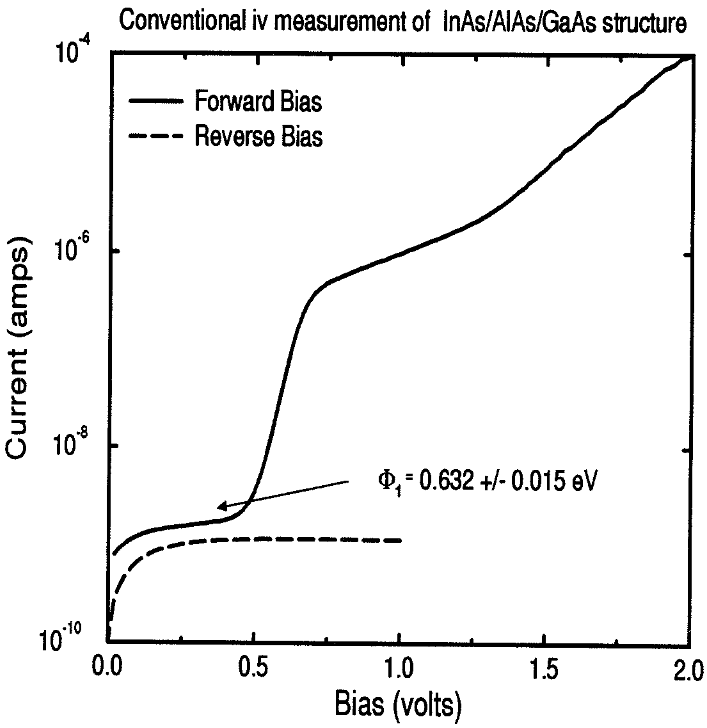

Figure 5.14: Conventional iv of InAs/AlAs/GaAs structure

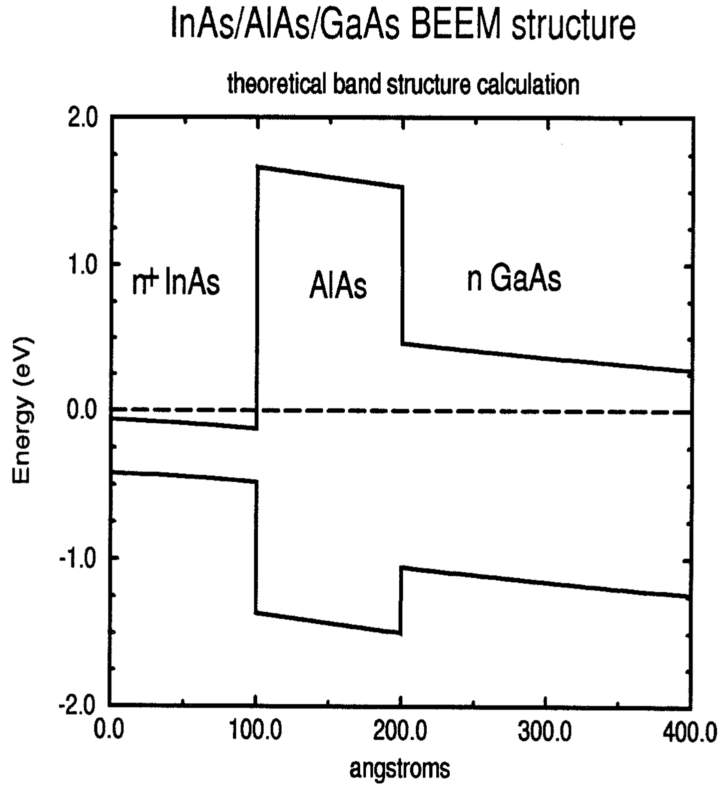

Figure 5.15: Energy band calculation of InAs/AlAs/GaAs structure.

### 5.5.2 Collector Spectroscopy

The collector current should clearly show a sharp current onset at voltages where the carriers injected from the tip see new transport channels into the GaAs substrate. From figure 5.13 we can see the potential channels for transport; the X-pt, L-pt, and Γ-pt in GaAs(100) and in AlAs(100). To see what transport channels are most important, one needs to examine the accessibility of states for transport. If momentum and energy are strictly conserved throughout the structure, which is the equivalent to the BK model for transport, the only allowed states for carriers injected into the sample would be X-pt and Γ-pt states in the collector. This is because carriers tunneling across the tip-sample gap have low transverse momentum and thus have momentum only in the growth direction of the crystal, the (100) direction. On the other hand, if we allow elastic scattering of the carriers, all states are accessible in the collector, including the L-pt states. This is equivalent to the LS model for transport. In addition to the accessibility of states, one also needs to consider the size of the "acceptance" cone to these accessible states. If we assume conservation of energy and momentum across the AlAs and GaAs interfaces along with parabolic conduction band minimums, then from equation 5.4 we see that the size of the acceptance angle is proportional to $(m_{||}/m)$, thus a larger $m_{||}$ means greater transport into those accessible states. Now, for AlAs $m_{||_{X-pt}} =$ 1.1m, $m_{||_{\Gamma-pt}} =$ 0.15m, and $m_{||_{L-pt}} =$ 1.9m, while for GaAs $m_{||_{X-pt}} =$ 0.257m and $m_{||_{\Gamma-pt}} =$ 0.067m[7]. Thus intuitively one would expect relatively large transport through the AlAs X-pt into the GaAs Γ-pt as well as transport through the AlAs L-pt and over the AlAs Γ-pt.

Figure 5.16 shows two collector current spectra taken at two different locations on the surface, demonstrating the sharp current onsets. In this figure we have fit each sharp onset of the data to the function $I_c = \sum_i C_i(V_t - \phi_i)^2$, where $\phi_i$ is the energy of the new channel that transports carriers into the GaAs, $C_i$ a scaling constant, and the index i enumerates the transport channels. In fitting the data

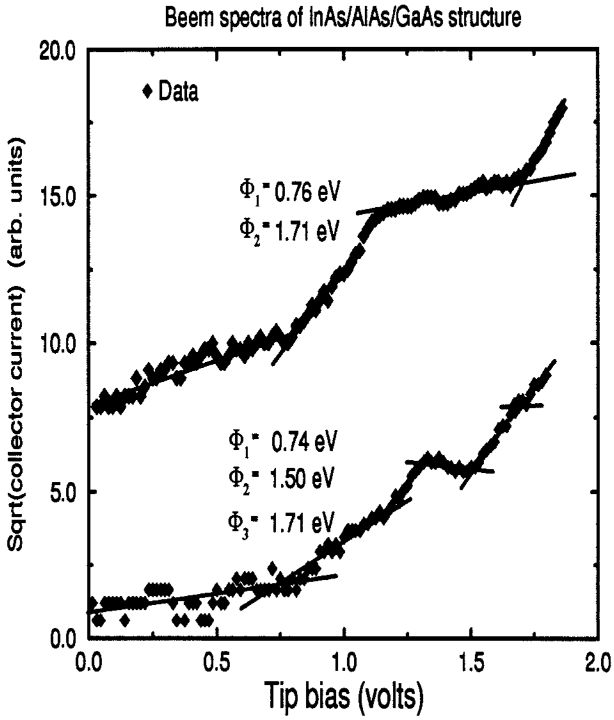

Figure 5.16: BEEM spectra of InAs/AlAs/GaAs structure along with quadratic fit.

to the quadratic function, we have assumed that each new channel or band can be approximated by a parabolic minimum in energy and that the current increase due to each new channel or band is additive. Although it is questionable to apply the parabolic band approximation near the X-pt and L-pt, the data appears to follow the functional form that this assumption leads to. The current is also seen to plateau between onsets. We feel that this is due to the saturation of a given channel by carriers and hence the current remains approximately constant until a new channel is reached in energy. It should be noted that the energy extracted from the fit, $\phi_i$, represents only a rough approximation of the transport channel energy.

From the two data sets we have extracted from the fits approximate band energies. Comparing these energies to figure 5.13, we see that several of the energies can be attributed to local band structure characteristics in the AlAs and GaAs. For example, energies near 0.75 eV can be attributed to tunneling into the GaAs Γ-pt, and energies near 1.71 eV can be attributed to transport over the Γ-pt in AlAs into the GaAs substrate. One could speculate that the 1.5 eV channel present in the lower data set could possibly represent tunneling through the L-pt in the AlAs barrier. This would require the L-pt band to shift down in energy. One mechanism that could cause this is the formation of strain. InAs and AlAs have a lattice mismatch of about 6%, thus the AlAs could be under local compressive strain in the transverse direction and tensile strain in the longitudinal (100) direction. In III-V compounds, tensile strain generally shifts the X-pt and L-pt bands downward in energy [8]. Another possibility is that the 1.5 eV channel is simply a lower local barrier due to defects for the Γ-pt in AlAs.

To verify the significance of these fit energies, we performed frequency statistics on 10 BEEM spectra. Figure 5.17 shows the distribution of the occurrences as a function of the fit energy. The bin width for each energy is 0.05 eV. From the plot it is apparent that there is a high occurrence about 0.70, 1.5, and 1.7 eV for the onset of current in the collector current data. The high occurrence near 0.70 eV supports the hypothesis that the X-pt tunneling into the Γ states of GaAs represents a strong current channel while the high occurrence near and above 1.5 and 1.7 eV eV may represent transport over the AlAs Γ-pt barrier. We see other energies present that could represent tunneling through the AlAs into the GaAs X-pt, however, the occurrences are too low to express any confidence in their significance.

## 5.6 Summary

In summary, we have developed the ability to perform Ballistic Electron Emission Microscopy. We have confirmed its operation though an investigation of the Au/Si

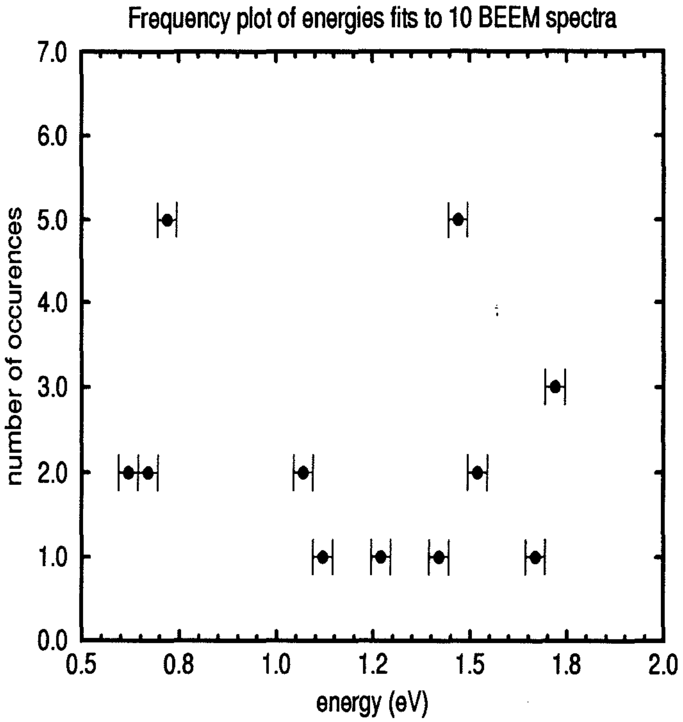

Figure 5.17: Frequency plot of fit energies for 10 BEEM spectra.

structure, by extracting the local Schottky barrier and examining simultaneous images of both the surface and the Au/Si interface. In addition, we have performed preliminary BEEM experiments on Au/InAs/AlAs/GaAs and have found evidence of local band structure effects, particularly into the Γ-pt of the GaAs and possibility above the AlAs barrier. Further experiments need to be performed in order to confirm these band related effects including varying the AlAs barrier thickness and experimenting with the sample surface preparation to ensure oxides are removed and that the Au deposition is smooth.

# Bibliography

[1] L. D. Bell, S. J. Manion, M. H. Hecht, W. J. Kaiser, R. W. Fathauer, and A. M. Milliken, *Phys. Rev. B* **48**, 5712 (1993).

[2] A. E. Fowell, A. A. Cafolla, B. E. Richardson, T. H. Shen, M. Elloitt, D. I. Westwood, and R. H. Williams, *Applied Surf. Science* **56**, 622 (1992).

[3] L. D. Bell and W. J. Kaiser, *Phys. Rev. Letters* **61**, 2368 (1988).

[4] P. Neidermann, L. Quattropani, K. Solt, I. Maggio-Aprile, and O. Fischer, *Phys. Rev. B* **48**, 8833 (1993).

[5] E. Lee and L. Schowalter, *Phys. Review B* **45**, 6325 (1992).

[6] J. J. Quinn, *Appl. Phys. Lett.* **2**, 167 (1963); D. R. Penn, *Phys. Rev. B* **35**, 482 (1987).

[7] O. Madelung, *Semiconductors and Group IV Elements and III-V Compounds* (Springer-Verlag, New York, 1991).

[8] J. I. Pankove *Optical Processes in Semiconductors* (Dover Publications, New York, 1975).

# Appendix A

# STM Tunneling Theories and AFM Interactions

## A.1 3-D Metal-Gap-Metal Tunneling

The fundamental question for STM experiments is that, even if one had an ideal tip, an ideal sample, and were using an instrument perfect in every way, what exactly is being measured? The answer is not trivial since only a full quantum-mechanical 3-dimensional analysis is truly satisfactory by the very nature of the problem. A quantum-mechanical treatment requires full knowledge of the tip and sample wavefunctions not just asymptotically but in the small gap region as well, where the wavefunctions have to be matched. Thus in attacking this problem, theorists have in general relied on perturbative approaches that assume only weak coupling between the tip and the sample. This of course only holds when the tip and sample are well separated and at low biases and currents. Another approach is to ignore the 3-dimensional character of the problem which simplifies the calculation tremendously yet still seems to yield reasonable results. We will briefly review these different theoretical approaches and compare their results with experimental evidence.

J. Tersoff was the first to derive the theoretical results for the 3-D STM model[40] by using a first-order quantum-mechanical perturbation method called the transfer Hamiltonian. This has proved to be the method of choice for theorists concerning this 3-D problem. According to first-order perturbation theory, the current density J can be expressed as

$$J = \frac{2\pi e}{\hbar} \sum_{u,v} [f(E_u)(1 - f(E_v)) - f(E_v)(1 - f(E_u))] |M_{uv}|^2 \delta(E_v + eV - E_u), \quad \text{(A.1)}$$

where f(E) is the Fermi function, V is the applied voltage, $M_{uv}$ is the tunneling matrix element between states $\phi_u$ and $\phi_v$ of the tip and the sample, respectively, $E_u$ is the energy of $\phi_u$, $E_v$ is the energy of $\phi_v$, and e and $\hbar$ are the normal constants. Assuming small V and replacing the Fermi functions by their zero-temperature approximations (i.e., step functions), the second term in the brackets goes to zero and the equation simplifies to

$$J = \frac{2\pi}{\hbar} e^2 V \sum_{u,v} |M_{uv}|^2 \delta(E_u - E_f)\delta(E_v - E_f). \quad \text{(A.2)}$$

This simple expression still requires the rather difficult task of evaluating the tunneling matrix elements.

Bardeen[41] derives a rather simple expression for the tunneling matrix elements for a metal to the left of $x_v$ and another metal to the right of $x_u$. He assumes that $\phi_v$ is the solution of the Schrodinger equation with energy $E_v$ for $x < x_v$ but there is a region to the right of that where it is not, where the wavefunction drops smoothly to zero. Likewise, $\phi_u$ is a solution with energy $E_u$ for $x > x_u$ but not for a region right of that. Both $\phi_v$ and $\phi_u$ are a good solution in the barrier region, $x_v < x < x_u$.

One then forms a time-dependent solution as a linear combination of both states as

$$\phi = a(t)\phi_v e^{-iE_v t} + \sum_u b_u(t)\phi_u e^{-iE_u t} \tag{A.3}$$

and substituting this into Schrodinger's equation. From Fermi's golden rule we get the result

$$M_{uv} = \int \phi_v^*(H - E_u)\phi_u d\tau \tag{A.4}$$

where the integral vanishes where $\phi_v$ disappears, to the left of $x_v$. To make the equation symmetric and by assuming conservation of energy (i.e., $E_v = E_u$), we substract $\phi_u(H - E_v)\phi_v$ and limit the integration to the left of $x_v$ and get

$$M_{uv} = \int_{x_v} [\phi_v^* H\phi_u - \phi_u^* H\phi_v] d\tau. \tag{A.5}$$

Finally, we introduce under the integral a step function that is unity between some point where $\phi_u$ vanishes (left of $x_v$) and just to the right of $x_v$. After integrating by parts and assuming a constant potential we find,

$$M_{uv} = \frac{\hbar^2}{2m} \int d\vec{S}(\phi_u^* \vec{\nabla}\phi_v - \phi_v^* \vec{\nabla}\phi_u), \tag{A.6}$$

where the integral is over the surface lying entirely within the barrier region[41]. In order to complete the calculation, one must explicitly know the wavefunctions of the sample and tip. Unfortunately, the atomic structure of tip is not well characterized and even if it were, the asymmetric character of the tip would make the wavefunction very difficult to calculate. Thus one must attempt to find a reasonable but general model for the tip.

As a simple but illustrative case, consider an ideal STM with a tip that is represented as a mathematical point source at $\vec{r}_t$. This tip would of course give maximum resolution and minimum interaction with the sample. In this case current density can be shown to be

$$J \propto \sum_v |\phi_v(\vec{r}_t)|^2 \delta(E_v - E_f) \equiv \rho(\vec{r}_t, E_f). \tag{A.7}$$

Thus an ideal STM would measure the sample's local density of states at the Fermi level as seen at the tip's position. This is probably the most important result from theory even though it is only strictly true for metals at low biases.

A more realistic tip model represents the tip as a spherical potential well of effective radius R [40]. It had been noted by experimentalists that W, Mo, and stainless steel tips produced similiar STM images, implying that the details of the tip's electronic structure were unimportant[42]. Thus in the early models only s states were assumed for the tip wavefunctions. States with higher angular momentum were estimated to make little contribution to the tunneling current since they will have nodes directly below the tip and because of the exponential dependence of the current on the separation. From this approach Tersoff showed the relationship expressed in equation A.7 remained valid and that the lateral resolution is roughly equal to $[2\text{Å}(\text{R} + \text{d})]^{1/2}$ where d is the tip-sample separation, in agreement with experiment.

Lang employed a more realistic model in order to answer whether the tip wavefunctions significantly affect the current[43]. Lang used a similiar perturbation method to Tersoff's but modeled the tip as a single atom. The simplification of the low voltage limit was assumed along with a jellium model for the metal surface; wavefunctions were already known for the jellium surface both with and without the adsorbed atom. Several different atoms were used in the model in order to test the effect of the different tip wavefunctions on the current and resolution. The result is that nonzero angular momentum states in the tip, although they can contribute significantly to the density of states, make only a small contribution to the current. Chung et al., further showed that for accidental degeneracies occurring between the s and d states, the d states may contribute up to 10% of the total current[42].

There are several problems that exist with the above theories even when applied to ideal metal-gap-metal systems. We will first discuss the more significant difficulties for this simple system and then look at further difficulties when the sample is a semiconductor.

One problem with most complex quantum-mechanical treatments concerns what basis set of wavefunctions to use[44]. Most techniques that solve for wavefunctions solve the Schrodinger equation, discretize space, and transform the problem into one of diagonalizing the Hamiltonian. Even though information concerning the wavefunction tails is generally lost, this procedure has worked well for band structure or energy calculations. However, for the STM it is these wave tails that extend several angstroms away from the surface that contribute most significantly to the current. Thus the problem is one of accurately representing the wavefunctions at relatively large distances from the nuclei. A planewave basis requires a prohibitively large number of basis waves for accuracy. Local basis sets can lead to severe errors in compound systems such as GaAs, where the true wavefunction is some mix of the component wavefunctions. Using a local basis set, different atoms will have different decay lengths and eventually one atom will dominate. However, the true wavefunction has a single decay length and either atom can dominate depending on the bias voltage[45].

An inaccurate representation of the potential in the gap region is also a source of errors. Without an accurate description of the potential the correct wavefunctions cannot be calculated. Not only may the applied voltage be appreciable, but the workfunctions of the tip and surface may also be significantly different. In addition, correlation and exchange effects such as image potentials can drastically affect the potential especially for the distances we are considering[46, 25]. In addition, the accuracy of the perturbation method can be called into question with regard to calculating the tunneling matrix. Bardeen's formula assumes the the potential in the barrier region is constant in the gap region between the tip and surface which, for systems with large varying potentials, is not true. In addition, by assuming conservation of energy, one is ignoring all inelastic tunneling processes. Although one does not expect significant scattering in the barrier region, rough surfaces may allow carriers to scatter into states otherwise inaccessible.

When one considers the details of a semiconductor surface, the complications increase tremendously. Leaving aside the complications of full quantum-mechanical treatments and the calculations of wavefunctions, we still find plenty of difficulties even with the semi-classical approach. First, the potential must be calculated not only in the barrier region but also in the semiconductor. To compute the potential profile correctly, a self-consistent transport equation must be solved along with Poisson's equation with full semiconductor statistics. We need to also include exchange and correlation effects in the semiconductor and barrier and the effect of surface states on the potential profile. We then must calculate transmission probabilities for tunneling not just through the barrier but also through the semiconductor space charge region. We need to consider other transport mechanisms in addition to tunneling such as recombination in the space charge region or at the surface states.

## A.2 1-D Metal-Gap-Semiconductor Tunneling

Because of the overwhelming complications involved with the introduction of a semiconductor, we will employ a model that includes many simplifying assumptions in order to facilitate interpretation of data in this thesis, particularly chapter 4. The assumptions we make have been used by several authors for explaining data for STM experiments, where the sample is a semiconductor such as Si and GaAs[49, 48]. These assumptions emphasize the classical semiconductor complications at the expense of a true quantum-mechanical approach. Indeed it is surprising that this approach has been used so successfully for modeling the data. We assume independent single electron one-dimensional tunneling as formulated by Duke et al., and will include quantum effects only through the electron transmisson probability[47]. We will also assume the conservation of energy (E) and $k_{||}$, which means that we are assuming no scattering and translational symmetry at the interfaces. We will use a classical model that includes the effects of semiconductor band bending, image potentials, and surface states to emphasize the accurate calculation of the potential. This potential is then used to calculate the transmission probability (see figure A.1). We will neglect tunneling into and out of these surface states along with recombination. We also assume small current densities so that the semiconductor is in equilibrium ( we see the consequences of relaxing this assumption in chapter 4).

We assume the tip behaves as an ideal metal whose behavior is determined solely by Fermi-Dirac statistics and a dielectric constant $\epsilon_m$, and the gap is a vacuum although it is a straightforward extension to include an oxide barrier. The gap region is depicted as a charge-free region with multiple image force corrections due to both the metal and semiconductor surface.

The insulator (gap) region can be characterized by the following equations:

$$\phi(x) = \phi_1(x) - \phi_{image}^{gap}(x) \tag{A.8}$$

$$\frac{d^2\phi_1(x)}{dx^2} = 0 \tag{A.9}$$

with the boundary conditions

$$\phi_1(s^-) = \chi_{sc} + V_{ds} + E_{cf} \tag{A.10}$$

$$\phi_1(0^+) = V + W_m \tag{A.11}$$

$$\epsilon_o \frac{d\phi_1(s^-)}{dx} - \epsilon_s \frac{d\phi_1(s^+)}{dx} = Q_{ss}, \tag{A.12}$$

where $\phi_{image}^{gap}(x)$ is the multiple images correction to the potential, $\phi_1(x)$ and $\phi(x)$ are the potential in the insulator region with and without the image potential correction, respectively, s is the tip-sample separation, q is the charge, V is the applied bias, $W_m$ is the metal workfunction, $\chi_{sc}$ is the semiconductor electron affinity, $V_{ds}$ is the amount of semiconductor band-bending, $Q_{ss}$ is the surface charge on the semiconductor, $E_{cf}$ is the difference in energy between the conduction band and the semiconductor's Fermi level, and $\epsilon_s$ and $\epsilon_o$ are the dielectric constants for the sample and insulator, respectively.

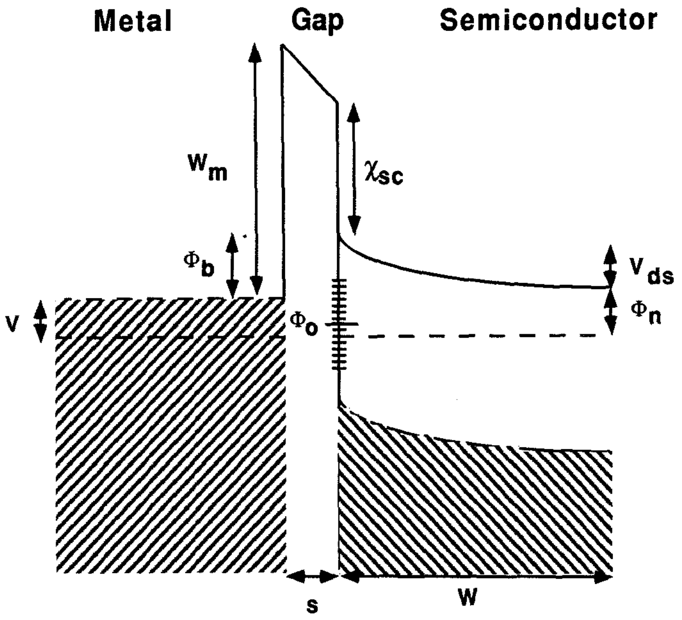

Figure A.1: Typical metal-gap-semiconductor band structure (image potential correction not shown)

In the semiconductor region, the potential is described by Poisson's equation and an image force correction term:

$$\phi(x) = \phi_1(x) - \phi^{sc}_{image}(x) \tag{A.13}$$

$$\frac{d^2\phi_1(x)}{dx^2} = \frac{-q^2}{\epsilon_{sc}}[p(x) - n(x) + N_d^+(x) - N_a^-(x)], \tag{A.14}$$

where p, n, $N_d^+$, and $N_a^-$ represent the concentration of holes, electrons, ionized donors and ionized acceptors, respectively. To find n, p, $Nd^+$, and $Na^-$, the complete form for the density of states and Fermi-Dirac statistics are used, for example

$$n = 4\pi(\frac{2m_e^*}{\hbar^2})^{3/2}\int_{E_c}^{\infty}\frac{(E-E_c)^{1/2}dE}{1+exp[(E-E_f)/KT]}, \tag{A.15}$$

where K is the Boltzman constant, T is the temperature, $E_c$ is the conduction band edge, and $E_f$ is the Fermi energy. Numerically integrating equations A.9 and A.14 over the entire gap-semiconductor region and using equations A.10, A.11, and A.12 as boundary conditions, we solve for the potential everywhere. We then correct for the image potential and then perform a cubic fit at the boundaries to ensure continuity of the potential and its derivative. This model describes, assuming equilibrium and neglectible current densities, the semiconductor in accumulation, depletion, and inversion.

The semiconductor's surface charge, as referred to in equation A.12, is determined by the occupation of the surface states. We characterize this occupation by a simple model, $Q_{ss} = qD_s[\phi_o - (E_g - \phi_b)]$, where $D_s$ is the density of surface states per eV, $\phi_b$ is the barrier height referenced to the tip's Fermi level, and $\phi_o$ is the neutral energy level and is fixed relative to the semiconductor conduction band[50]. The main characteristic of the neutral level is that when the semiconductor's Fermi level is at the same energy as the neutral level, the surface is assumed to be locally charge neutral. The neutral level is surrounded by donor-like states that are lower in energy and acceptor-like states that are higher in energy. It is these states that act as an electrostatic feedback mechanism to pin the Fermi level at the neutral level. We assume that the states occupation is determined by the semiconductor's Fermi level [26].

It is easy to show (we will spare the reader the drudgery) the nondegenerate approximation for the semiconductor one can show that the band bending in the semiconductor is

$$V_{ds} = V_o\{[(\frac{s}{s_o(1+c)})^2 + (\frac{c}{1+c})\frac{(\phi_o - \phi_n)}{V_o} + (\frac{1}{1+c})(\frac{V_o + V}{V_o})]^{1/2} - \frac{s}{s_o(1+c)}\}^2, \tag{A.16}$$

where $V_o$ and W$_o$ are the band bending and the depletion layer width in the semiconductor with zero tip-sample separation and zero bias, $s_o = W_o/\epsilon_s$, s is the tip-sample separation, $\phi_n$ is the difference in energy between the conduction band and the semiconductor's Fermi level, and $c = \frac{sqD_{ss}}{\epsilon_o}$. As the surface density of states increases to infinity, so does c and the band bending V$_{ds}$ becomes pinned at $\phi_o - \phi_n$.

Intuitively the pinning mechanism can be understood by first assuming the junction is electrically neutral, that is $Q_m + Q_{ss} + Q_{sc} = 0$, where Q$_m$ is the fixed charge on the metal surface and Q$_{sc}$ is the total charge in the semiconductor space-charge region and that initially Q$_{ss}$ = 0. Thus $\Delta Q_{ss} = \Delta Q_{sc}$. If we bias the junction so the semiconductor bands bend, surface charge will accumulate on the semiconductor surface since the neutral level follows the semiconductor bands. This positive (negative) surface charge induces a negative (positive) space charge in the semiconductor. The semiconductor space charge causes the semiconductor bands to bend in the direction that moves $\phi_o$ toward E$_{fm}$ and hence reduces Q$_{ss}$. Thus the surface states act as a sort of negative feedback in order to reduce Q$_{ss}$ and pin the neutral energy level to the metal Fermi level. Increasing the density of the surface states can be viewed as increasing the "gain" of the feedback. In our model, we can adjust the position of the neutral level and the distribution of the surface states to take on any realistic configuration.

To calculate the current density we assume independent electron tunneling:

$$J = \frac{q}{h}\int_0^\infty dE_z T(E_z)\int \frac{dk_{||}^2}{(2\pi)^2}[f(E) - f(E + eV)] \tag{A.17}$$

where q and h are the usual constants, f(E) and f(E + eV) are the Fermi functions in the tip and semiconductor region, respectively, and T($E_z$) is transmission probability for single electron tunneling. The transmission probability can be estimated using several methods, the most popular using the WKB theory. We use a tightbinding matrix method that is fully quantum mechanical and has proven numerically stable even with rapid changing potentials[51]. We also include tunneling through the semiconductor space charge region in our calculations.

Introducing the Jacobian $\frac{dE_{||}}{d^2k_{||}} = \frac{h^3}{8\pi^3 m^*}$ and integrating over $dE_{||}$, we obtain the following expression for the tunneling current:

$$J_i = \frac{2\pi qKT}{h^3}\int_0^\infty dE_x T(E_x)[N_m(E_x) - N_i(E_x, V)] \tag{A.18}$$

where K is the Boltzman constant and $N_m$ and $N_i$ are the metal and semiconductor supply function, respectively and i denotes conduction band (cb) or valence band (vb) tunneling in the semiconductor. The supply functions are represented as:

$$N_m = (2s + 1)m_m^* \ln[1 + e^{(E_f - E_x)/KT}] \tag{A.19}$$

$$N_i = (2s_i + 1)m_i^* \ln[1 + e^{(E_f - E_x - eV)/KT}] \tag{A.20}$$

where $m_m^*$ and $m_{sc}^*$ are the metal and semiconductor effective mass, respectively and s is the electron or hole spin degeneracy.

To calculate the total current, we add the contributions due to valence and conduction band tunneling:

$$J = J_{vb} + J_{cb}. \tag{A.21}$$

## A.3 AFM Tip-Surface Interactions

The tip-surface interaction and how it specifically influences AFM data is still not well understood. In actuality a whole array of forces can be acting between the tip and sample at any one time depending on the specific properties of the two materials and the microscopic details of their structure. These forces can vary in range and magnitude and it is important to have some understanding of their relative importance in order to acquire and understand AFM data. For this discussion we will ignore magnetic and electrostatic forces since they only dominate at long range and under special sample surface conditions which we experimentally avoid.

There are two main forces whose influence dominates the tip-surface interaction for the samples we are interested in. These are the van der Waals force and ionic repulsion[52]. Van der Waals forces are always present and include induction forces (the interaction of a dipole and an induced dipole), orientation forces (the interaction between two orientated permanent dipoles), and dispersion forces (induced dipole-induced dipole interaction). Dispersion forces are also referred to as London forces and generally follow a $1/r^6$ power law. They are relatively long ranged (2 Å to > 100 Å) and can be attractive or repulsive. When the tip is several nanometers from the surface the dominant force is the van der Waals force.

Ionic repulsion begins to dominate when two surfaces are within a few angstroms and their electron clouds begin to overlap significantly, giving rise to a repulsive force. Both the van der Waals force and the ionic repulsion has been expressed in the Lennard-Jones potential that describes intermolecular pair interaction;

$$U(r) = 4N\epsilon[(\frac{\sigma}{r})^{12} - (\frac{\sigma}{r})^{6}] \tag{A.22}$$

where $\epsilon$ is the potential minimum, r is the separation of the two atoms, N is the number of interacting pairs, and $\sigma$ is a constant dependent on the nature of the materials involved. This is the dominant force when operating in the contact mode.

Atomic resolution can be achieved because of the ionic repulsion's strong distance dependence.

Another significant factor for AFM imaging is the medium in which it is taken. For example, since the majority of our AFM experiments are performed in air, the surface becomes coated with a thin layer of liquid (predominately water). This thin layer, typically only a few nanometers thick, can have a profound effect on the tip-surface interaction. The fluid forms a meniscus bridge between the tip and sample that produces a strong attractive effect, called the capillary force. The magnitude of this force can be simply estimated from the Laplace equation for pressure, $P = \gamma_l/r = F/A$, where P is the pressure, $\gamma_l$ is the surface tension of the liquid, r is the radius of curvature of the meniscus between the tip and sample, F is the force, and A is the surface area of the meniscus [58]. If we approximate the meniscus as a cylinder of radius R ($R >> r$) and height h, we find that the force exerted by the meniscus can be written as $F = (2\pi Rh)\gamma_l/r$. For reasonable values of $h = 2$ nm, $R = 100$ nm (typical AFM tip radius), $r = 1$ nm, and $\gamma_l = 72$ $mJ/m^2$ (for water), we get $F = 90nN$. For AFM experiments, a reasonable van der Waals force for these parameters would be about 60 nN for materials of average surface energy, indicating the capillary force can dominate tip-surface interactions, producing tip instabilities.

When the tip is in intimate contact with the surface, such as in the contact mode, adhesion forces may be present. Adhesion forces are correlated with surface reconstructions, atomic segregation, and chemical reactions between surfaces. Although these forces can be significant given moderately reactive surfaces, the atomic details are not well known. Adhesion forces can also produce a hystersis in the force curves upon unloading the tip from the surface.

Elastic and plastic behavior of the surface and tip are also important interaction properties. First, most surfaces are elastoplastic, that is, they only partially return to their original shape after deformation. Of course if one is trying to image the surface, any plastic deformation is a permanent distortion of the true surface.

The elastoplastic characteristics of a surface can be determined by the penetration of the tip into and away from the surface as a function of applied force. For example, Sneddon solved for the force applied by a nonadhesive rigid flat ended cylinderical tip to a flat surface with modulus of elasticity E and Poisson's ratio v as $F = 2Erh/(1 - v^2)$, where F is the applied force, r is the tip radius, and h is the penetration depth[54]. In addition, the area of the tip-sample contact will also distort under loading. Under nearly any repulsive contact force, the tip distorts at the very end so single atom imaging rarely occurs. In addition, as the tip-sample contact area increases, the resolution will significantly be reduced as we previously showed.

# Bibliography

[1] R. K. Watts, *Submicron Integrated Circuits* (John Wiley and Sons, New York, 1989).

[2] W. Boudville, Ph.D. Thesis, California Institute of Technology, 1988.

[3] M. Phillips, Ph.D. Thesis, California Institute of Technology, 1993.

[4] J. O. McCaldin, *J. Vac Sci. Technol. A* **8**, 1188 (1990).

[5] D. J. Chadi, *Appl. Phys. Lett.* **59**, 3589 (1991).

[6] R. M. Park, M. B. Troffer, C. M. Rouleau, J. M. DePuydt, and M. A. Haase, *Appl. Phys. Lett.* **57**, 2127 (1990).

[7] S.Guha, J. M. DePuydt, M. A. Haase, J. Qiu, and H. Cheng, *Appl. Phys. Lett.* **63**, 3107 (1993).

[8] S. M. Sze, *VLSI Technology* (McGraw-Hill, New York, 1988) p. 366.

[9] K. Miura, K. Sugiura, and H. Sugiura, *Surface Science Letters* **253**, 1407 (1991).

[10] W. J. Kaiser and L. D. Bell, *Physical Review Letters* **60**, 1406 (1988).

[11] M. C. Phillips, J. F. Swenberg. M. W. Wang, J. O. McCaldin, and T. C. McGill, *Physica B* **185**, 485 (1993).

[12] M. C. Phillips, M. W. Wang, J. F. Swenberg, J. O. McCaldin, and T. C. McGill, *Appl. Phys. Lett* **61**, 1962 (1992).

[13] Y. Fan, J. Han, J. Sarave, R. C. Gunshor, M. M. Hagerott, and A. V. Nurmikko, *Appl. Phys. Lett* **63**, 1812 (1993).

[14] L. J. Schowalter, R. W. Fathauer, R. P. Goehner, L. G. Turner, R. W. DeBlois, S. Hashimoto, J.-L. Peng, W. M. Gibson, and J. P. Krusius, *J. Appl. Phys.* **58**, 302 (1985).

[15] L. J. Schowalter and R. W. Fathauer, *CRC Reviews of Solid State Materials Sciences* **15**, 367 (1989).

[16] T. Asano and H. Ishiwara, *Appl. Phys. Lett.* **3**,68 (1982).

[17] R. W. Fathauer, N. Lewis, E. L. Hall, and L. J. Schowalter, *J. Appl. Phys.* **60**, 3886 (1986).

[18] J. J. Gillman, *J. Appl. Phys.* **31**, 2208 (1960).

[19] C. Mead, *Scaling of MOS Technology to Submicrometer Feature Sizes*, Colloquium at Caltech, Pasadena, California (1993).

[20] L. D. Bell and W. J. Kaiser, *Phys. Review Lett.* **61**, 2368 (1988).

[21] A. M. Milliken, S. J. Manion, W. J. Kaiser, L. D. Bell, and M. H. Hecht, *Phys. Review Lett.* **46**, 12826 (1992).

[22] E. Y. Lee, B. R. Turner, J. R. Jimenez, and L. J. Schowalter, *J. Vac. Sci. Technol. B* **11**, 1579 (1993).

[23] A. E. Fowell, A. A. Cafolla, B. E. Richardson, T. H. Shen, M. Elliot, D. I. Westwood, and R. H. Williams, *Appl. Surface Science* **56**, 622 (1992).

[24] H. D. Hallen, A. Fernandez, T. Huang, J. Silcox, and R. A. Buhrman, *Phys. Review B* **48**, 5712 (1993).

[25] M. Kleefstra and G. C. Herman, *J. Appl. Phys.* **51**, 4923 (1980).

[26] E. H. Rhoderick and R. H. Williams, *Metal-Semiconductor Contacts* (Oxford Science Publications, Oxford, 1988) p. 136.

[27] G. Binning and Rohrer, *Helv. Phys. Acta.* **55**, 726 (1982).

[28] G. Binning and Rohrer, *IBM J. Res Develop* **30**, 355 (1986).

[29] Materials Analytic Services, Raleigh, North Carolina, 27607.

[30] L. Montelius and J. O. Tegenfeldt, *Appl Phys. Lett.* **62**, 2628 (1993).

[31] R. M. Feenstra, private communication.

[32] Y. Kuk and P. J. Silverman, *Rev. Sci. Instrum.* **60**, 165 (1989).

[33] D. W. Pohl, *IBM J. Res. Develop* **30**, 417 (1986).

[34] T. Tiedje and A. Brown, *J. Appl. Phys.* **68**, 649 (1990).

[35] M. B. Johnson and J. M. Halbout, *J. Vac Sci. Technol. B* **10**, 508 (1992).

[36] A. G. M. Jansen, F. M. Mueller, and P.Wyder, *Science* **199**, 1037 (1978).

[37] G. Wexler, *Proc. Phys. Soc. London* **89**, 927 (1966).

[38] J. C. Maxwell, *A Treatise on Electricity and Magnetism* (Clarendon, Oxford, 1904).

[39] Y. V. Sharvin, *Zh. Eksp. Teor. Fiz.* **48**, 984 (1965).

[40] J. Tersoff and D. R. Hamann, *Phys. Rev. Lett.* **50**, 1998 (1983).

[41] J. Bardeen, *Phys. Rev. Lett.* **6**, 57 (1961).

[42] M. S. Chung, T. E. Feuchtwang, and P. H. Culter, *Surface Science* **187**, 559 (1987).

[43] N. D. Lang, *Phys. Rev. Lett.* **56**, 1164 (1986).

[44] J. Tersoff, *Scanning Tunneling Microscopy and Related Methods* (Kluwer Academic Publishers, 1990) p. 77.

[45] R. M. Feenstra, J. A. Stroscio, J. Tersoff, and A. P. Fein, *Phys. Rev. Lett.* **58**, 1192 (1987).

[46] Z. H. Huang, M. Weimer, and R. E. Allen, *J. Vac. Sci. Technol. B* **9**, 2399 (1991).

[47] C. B. Duke, *Tunneling in Solids* (Academic Press, New York, 1969) p. 30.

[48] M. Weimer, J. Kramar, J. D. Baldeschwieler, *Phys. Rev. B* **39**, 5572 (1989).

[49] R. M. Feenstra and J. A. Stroscio, *J. Vac. Sci. Technol. B* **5**, 923 (1987).

[50] E. H. Rhoderick and R. H. Williams, *Metal-Semiconductor Contacts* (Oxford Science Publications, Oxford, 1988) p. 16.

[51] D. Z. Ting, E. T. Yu, and T. C. McGill, *Appl. Phys. Lett* **58**, 292 (1991).

[52] H. Heinzelmann, E. Meyer, H. Rubin, and H. J. Gunterrodt, *Force Microscopy* (Kluwer Academic Publishers, Boston, 1989) pp. 450.

[53] G. Binning and C. F. Quate, *Phys. Rev. Lett.* **56**, 930 (1986).

[54] I. N. Sneddon, *Int. J. Eng. Sci.* **3**, 47 (1965).

[55] N. A. Burnham and R. J. Colton, *J. Vac. Sci. Technol. A* **9**, 2548 (1991).

[56] N. A. Burnham, *Appl. Phys. Lett.* **63**, 114 (1993).

[57] D. R. Baselt and J. D. Baldeschwieler, *J. Vac. Sci. Technol. B* **10**, 2316 (1992).

[58] J. N. Israelachvili, *Intermolecular and Surface Forces* (Academic Press, New York, 1986).

# Appendix B

# BEEM Construction and Operation

## B.1 BEEM Instrumentation Overview

This appendix is designed to instruct a person with only a marginal aquaintance with the BEEM setup on how the equipment works, how to design a successful BEEM experiment, and finally how to perform an experiment with the existing setup. We will proceed in the above order, first starting with the construction of the BEEM equipment. As previously discussed, BEEM can be viewed as simply a three terminal extension of the basic STM. The BEEM setup allows the flexibility to image simultaneously both the surface and the interface of metal-semiconductor as well as multilayered semiconductor structures. In order to be able to do this, the BEEM instrumentation has been fully integrated into the preexisting Digital Instruments equipment including its software acquisition and analysis programs. Figure B.1 shows the BEEM experimental apparatus along with its general integration with the STM setup.

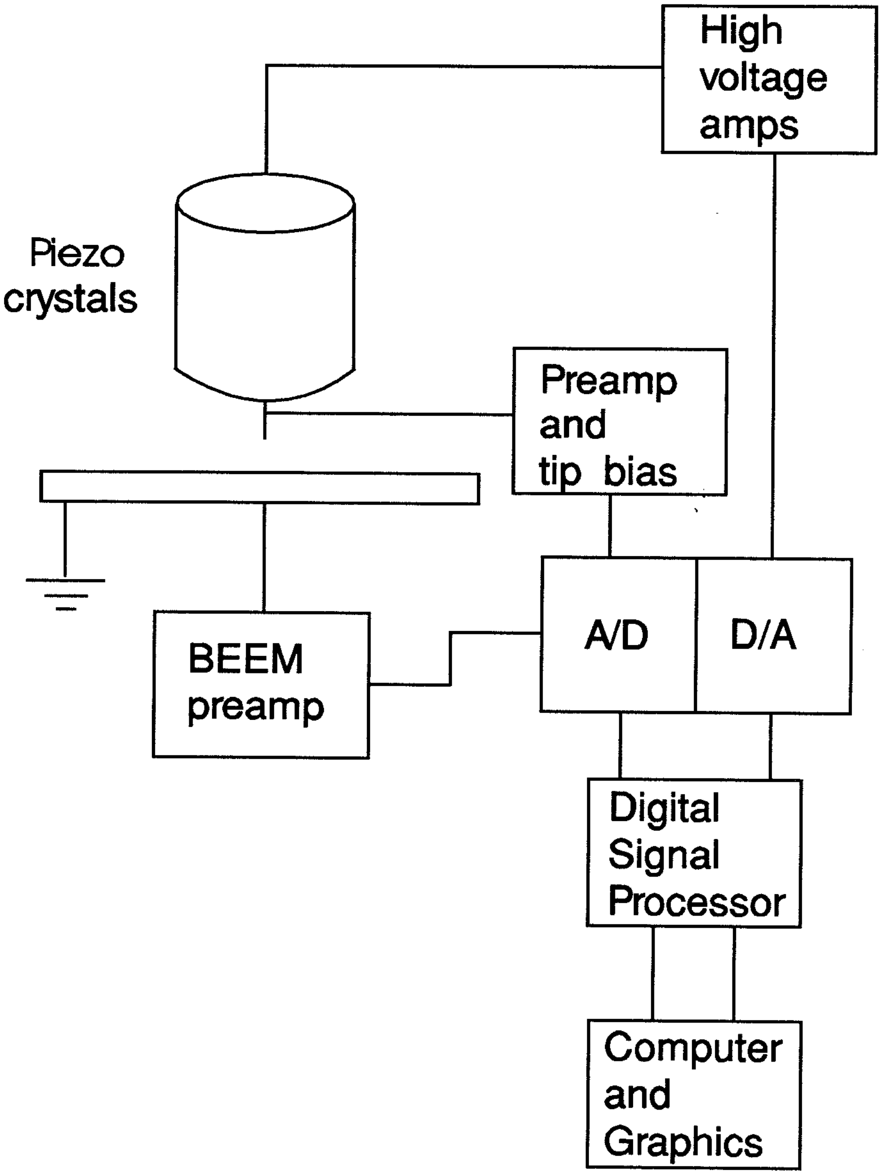

Figure B.1: Overview of BEEM and STM Setup.

## B.2 BEEM Instrumentation Construction

The purpose of this section is to provide the user with a detailed understanding of the modifications made to the STM in the construction of the BEEM equipment. The modifications can essentially be divided into three parts; the tip preamplifier, the collector amplifier, and the sample mount. The built tip preamplifier is entirely different from the Digital Instrument's design and must be working before any of the other parts can be tested. Hence we will discuss this first.

### B.2.1 Tip Preamplifier

The major difference between the built tip amplifier and the Digital Instruments preamplifer is the source of the sample-tip bias. In the Digital Instuments design the tip is hard-wired to ground while the sample's potential is varied. In our design, the sample is held at ground while the tip both measures the current and controls the voltage. While this may seem like a simple manner is renaming your reference voltage, it is important to sweep the tip bias and not the sample bias. Since the shielding everywhere is held at hard ground, sweeping the sample bias would require sweeping the shielding potential, leading to parasitic capacitances and currents that would be hard to eliminate.

The tip preamplifier sits on top of the piezoelectric crystals to which the tip is mounted. Figure B.2 shows a schematic of the interior electronics of the preamplifier along with a built-in picoammeter, all enclosed in the tip preamplifier housing. The picoammeter shown, along with the electronic board installed in the lower portion of the STM, could be used in place of the external Keithley picoammeter that is currently connected. It currently is not hooked up due to spurious voltage fluctations in the output. The current gain of the tip preamp is set at $10^8$ V/A but can be changed through a jumper on the AD-524 opamp. The two plugs connected together protruding from the back of the preamplifier are labeled as section B and C in figure B.2. The section labeled A is simply the stepper motor electronics kept in the base of the STM. The connections labeled X,Y,Z refer to the XYZ piezo voltages. Note that Z has only one connection since it is biased relative to the average of both X and Y. All STM and BEEM connections terminate at the 25 plug connector on the side of the STM base. The BEEM output signal itself outputs to what is called IN1A with its ground connection to SGND1A, which are pins 21 and 8 on the STM 25 plug connector, respectively. In addition, there is a LED light on the top of the tip preamp that is used to check sample connections. The pin connector for this is pin 6, OUTD0.

### B.2.2 Sample Holder

The sample holder acts as an interconnect between the tip preamp electronics and the BEEM preamp. Figure B.3 illustrates the modifications to the holder. The sample is mounted on the square copper area that is electrically connected by a copper strip to the BEEM signal plug. All the copper strips formed on the sample holder were made by patterned chemical etching of the surface of a bread board. The tip preamp has a lone wire pretruding from its base that connects hard ground to both the BEEM ground plug and to the sample surface. The wire from the tip preamp connects into the plug labeled "ground connection from tip premap" in figure B.3. The grounding of the surface of the sample is facilitated through the use of a gold wire, which is placed in contact with the surface. To make this connection more robust, one can place a drop of an InGa mixture at the end of the gold wire. The InGa mixture is highly conductive and remains liquid at room temperature, thus ensuring a good contact despite vibration or movement of the instrument. It should be noted that the gold wire is soldered onto the grounding wire and that this connection is relatively fragile.

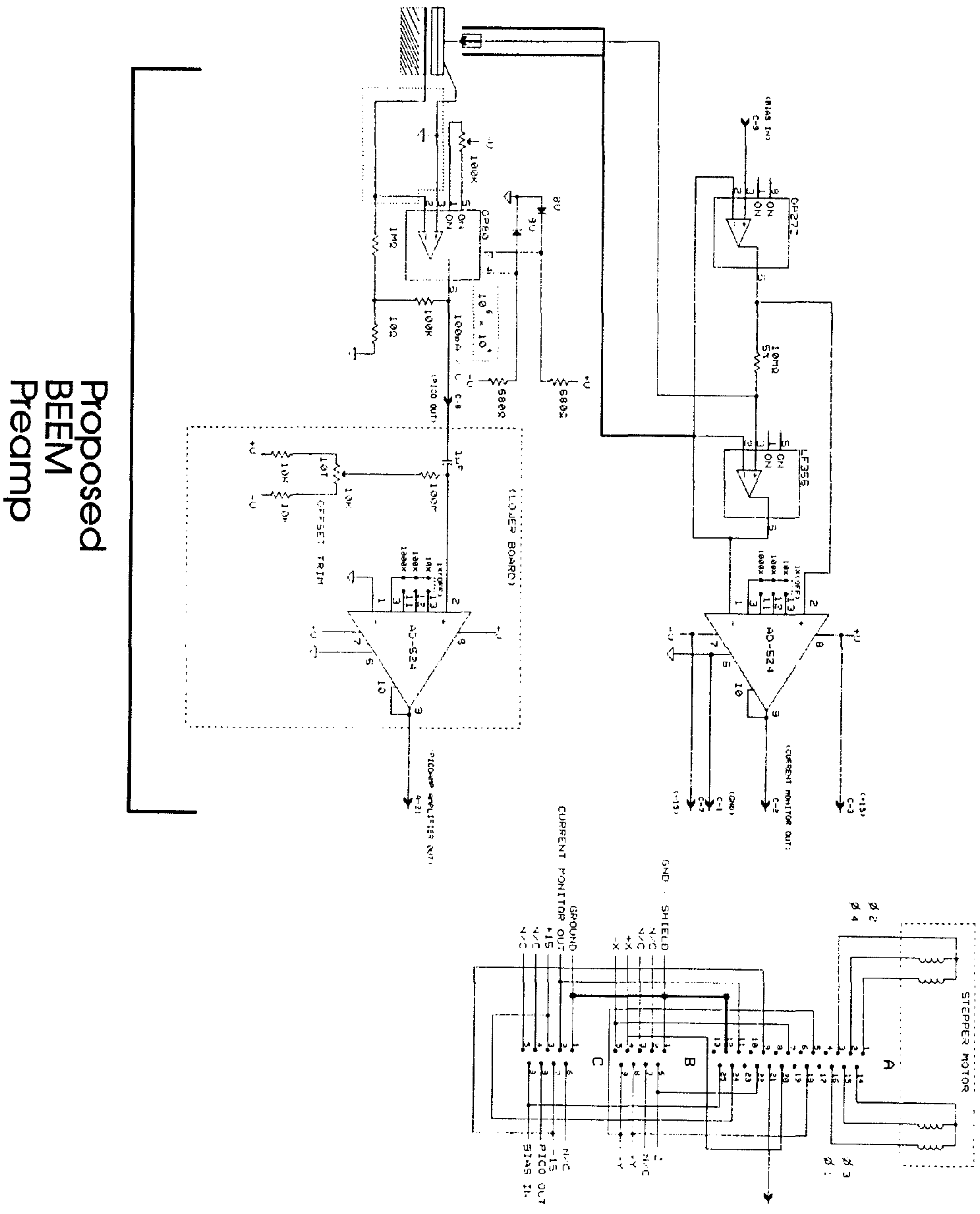

Figure B.2: Schematic of tip preamplifier.

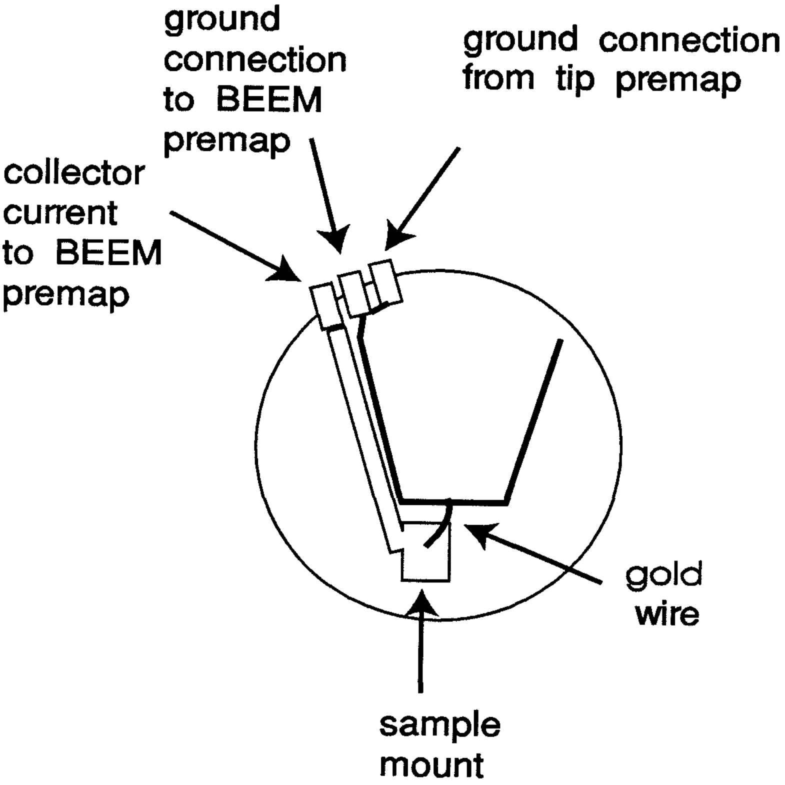

Figure B.3: Sample holder with modifications

### B.2.3 BEEM preamp

The BEEM preamp consists of a Keithley 486 picoammeter that receives its signals and ground reference from the sample holder BEEM plugs. In the lowest current range (2nA), the analog output is 2 volts, giving a gain of $10^9$ V/A. We further amplify this signal using software, as we will discuss in the software section. The BEEM preamp signal is connected to the collector current plug while the BEEM ground reference is connected to the ground connector plug, both located on the back of the sample holder. The BEEM ground plug is connected to the tip preamp ground plug through a small wire soldered between the two plugs. With a sample mounted and all connections properly made, the picoammeter should read in the $\mu$amp range. Thus is due to the photo-excitation of carriers from the conductive base into the collector. To test this hypothesis, simply wave your hand in front of the sample and the current should drop considerable ( with the Faraday cage/light shield over the instrument, the current should drop into the picoamp range). The analog output of the picoameter reconnects to the STM base by two wires going to pins 8 and 21.

## B.3 Sample requirements

BEEM samples must meet certain criteria in order for the experiment to be successful. A typical sample consists of at least two layers; a top layer called the base into which the tip injects carriers, and a lower layer called the collector to which the BEEM electronics are connected.

### B.3.1 Base requirements

The base layer must meet three requirements; it must be highly conductive, thin enough for ballistic transport, and inert and flat so that the surface morphology or contaminates do not dominate the interface characteristics. For the surface to be considered conductive, it should not charge up locally and it should readily make an ohmic contact with the gold wire for the ground connection. It should also sufficiently shield the interface from the external fields of the tip. The base should also be less than the inelastic mean free path of the carriers in the base material. This is generally on the order of several hundred angstroms although we have found that theoretical predictions are consistently longer than experimental measurements. It is also good practice to keep the thickness smaller than the elastic mean free path, since the elastic scattering of carriers can also significantly affect the collector current by spreading out the distribution in k-space and reducing the number that lie inside the "acceptance" cone (see chapter 5). Lastly, the base should also be smooth and inert since large thickness fluctuations in the base layer will yield strong variations in scattering. Clusters of contaminants will also act as scattering centers but have the additional effect of possibly modifying the tip. That is, if a contaminants is insulating, the tip may dig into the surface, thus damaging the resolution of the tip along with making the image difficult to interpret. Gold deposition by the Lesker sputter machine seems to have made significant improvements over the smaller mini-evaporators.

### B.3.2 Collector requirements

The collector materal and interface have another set of criterion to meet; it must present a significant barrier to carriers for acceptable signal-to-noise ratios and one must be able to make an ohmic contact to it. The ohmic contact is to prevent charging the collector and also provide an efficient means to measure the collector current. The barrier criterion is to ensure that the current noise across the interface at zero-bias voltage conditions across the sample is at most 1-2 picoamps. This is to ensure that the measured signal, which will be on the order of 1-2 picoamps at its threshold level, is measurable. In general, if we assume that the picoammeter produces voltage fluctations across the sample on the order of 1 $\mu$v and we wish to measure at a threshold current of 1 pA, then for a mesa size of 10 $mm^2$ we need the contact resistivity on the order of $10^5$ ohm $cm^2$. If the noise is too high the BEEM images will appear as popcorn noise and any barrier height or band information will be erroneous. Several tricks exist to increase the resistivity of the interface. One is cooling the sample, thus narrowing the distribution of carriers that could thermally excite over the barrier. Another is reducing the sample size, thus reducing the overall number of carriers that excite over the barrier. Thirdly, one could grow a thin layer of oxide or place a barrier between the layers to reduce the transmission probability between layers and also reduce problems related to interdiffusivity such as in Au/Si interfaces.

The above criteria are best met by choosing the proper sample for the experiment. For example, one generally knows the conductivity of a material as well as how easily ohmic contacts are made to it. The barrier critera is usually the most difficult to predict, since the zero-bias resistance is strongly related to the quality of the interface. It is always recommended to measure all contacts with conventional iv or cv techniques prior to attempting a BEEM experiment. Care should be used in selecting the frequency used to measure the iv or cv's of the sample since the resistance seen always has a reactive component to it.

## B.4 Operation

### B.4.1 Instrument operation

Now that the instrument components and sample selection criteria have been discussed, we will now layout the integrated operation that is necessary for a complete BEEM experiment. As previously mentioned, the most prudent practice is to ensure all contacts have been tested using conventional iv and cv measurements. After the contacts are shown to be ohmic and the zero-bias voltage resistivity is greater than $10^5$ ohms $cm^2$, the real fun begins. The sample, on the order of 1 cm$^2$ in size, is then mounted on the sample holder by first placing a dab of silver paint on the holder and spreading the silver paint as thin as possible, with the excess paint removed. The sample is placed on top of the paint, ensuring that none of the paint rides up along the side of the sample, possibly shorting across the interface. After the silver paint dries the sample should be firmly mounted to the holder. Connect the BEEM signal and ground plugs at this time. The picoammeter, assuming all the connections are in place, should now read several $\mu$amps. The gold wire is then lightly placed on the top of the sample, carefully allowing room for the tip to scan the surface. A new tip should be inserted into the tip holder prior to each experiment (STM tips are much less robust than AFM tips). The tip preamp is then placed on the mounting bearings over the sample holder. The tip grounding plug is connected to the sample holder and the dual electronic plug is connected to the back of the STM base. Ensure the 25 pin plug from the external controller is connected to the STM base. If this connection or the dual electronic plug is not connected, the engagement software will give false engagement of tip to the sample. With the tip preamp on, the picoammeter should now read several hundred picoamps.

The tip approach can now be made to the sample surface. The tip preamp is lowered toward the surface by turning the bearings clockwise. As the tip becomes close to the surface, through the hand held microscope one will be able to see the tip's reflection in the surface. Lower the tip until the actual tip and its reflection are separated by a tiny but visible amount (experience counts here). Ensure that the tip preamp is level and that it does not contact any of the connectors or wires associated with the sample holder. Place the Faraday cage/light shield over the tip preamp and sample holder and place the entire assembly on the vibration isolation platform (bunge cords with metal plate).

### B.4.2 Software operation

After all the equipment is in place, the remainer of the experiment is entirely controlled by the Digital Instrument's software. To call up the STM/BEEM menu, simply type "stm" in the dos shell. Prior to engagement, one must first select the proper piezo head for scanning. To do this , simply click on "Microscope," followed by "Select" and then "STMA." STMA is currently the only head modified for BEEM experiments. Next test the tip preamp by clicking on "Offset" and then "Leakage." Leakage measures the current leaking between the tip and the Y piezo (which is where the tip holder is mounted on). Offset measures the offset current that the tip preamp generates. Both currents should be less than about 50 picoamps. If the offset current is too high, a small screw accessible on the front of the tip preamp can be adjusted to zero the current. If the leakage current is too high the tip holder must be cleaned with acetone and methanol using a cotton swab, and then baked out at 80°C for about 2 hours in order to clean the holder of conductive contaminants. Note that the sum of the leakage and offset currents must be less that the setpoint current for tunneling or you will get false engagement of the tip.

The BEEM connections to the sample should now be checked. To do this, raise the voltage to "Analog 1" in the STM menu to about 2 volts. This will turn on the red LED mounted on top of the tip preamp, causing carriers to be photoexcited into the collector from the base. At this point, if all connections are properly made, the picoammeter should read a few $\mu$amps.

Once the premap has been selected and checked, the parameters for tunneling can be selected. These are truly sample dependent and hard rules do not apply. However, as a starting point the following parameters are recommended; the setpoint current should be initially set at about 0.5 - 0.4 nA to prevent excessive tip interaction with the surface. The bias should be set initally at about 0.5 volts or lower (high voltages with high currents tends to "sputter" the base material and cause tip modification). The integral and proportional feedbacks should be set at 10.0 and the scan rate should be set to about 1 Hz. These parameters were chosen in order to keep the tip relatively far from the surface, thus preventing the initially large thermal drift from damaging the tip and surface. Once thermal drift has decreased significantly, the parameters can be reset in order to measure a strong BEEM signal. Also one should assure that the collector signal is measured by channel A. This is verified by selecting "Calibration" in the Microscope menu and then selecting "Detector". The aux channel selected on the bottom right of the menu should read "Aux A." This ensures that when one selects the auxilary channel for viewing or spectroscopy, one is viewing channel A, which is the channel that the picoammeter is connected to. One can also amplify the signal by changing the sensitivity of channel A. It is currently set to 10V/V input, thus giving an amplification of 10x.

Once the parameters have been set, the tip can be engaged to the surface. To perform this, simply click on "Engage". The electronics will automatically advance the rear bearing until the setpoint current is detected. There will almost definitely be excessive thermal drift of the tip relative to the surface at this time. Several hours are usually required to reduce this to acceptable levels, that is, so that the tip will not modify if brought close to the surface and drifts less than 100Å/hr. To check the drift, view the scanned images for repeated features and see how much they move from frame to frame. Once thermal drift is deemed acceptable, the tunneling parameters can be changed to optimize the collector current. This means generally increasing the setpoint current and increasing the voltage to the point so that carriers can be injected over the interface barrier. To see the surface and interface images simultaneously, select (in the image mode) height data type for one screen and aux data type for the other. Surface topography and collector current levels will be displayed side by side. To measure BEEM spectroscopy, select in the view menu the "STS Plot (iv)." Once in this menu, select the aux channel for the input. The data displayed will be the collector current as a function of tip bias. One can improve the signal-to-noise by averaging over the signal. This is done by increasing the average count. The data sampling period should be as high as possible since there is a finite response time for the picoammeter to respond to increases in collector current levels (70 msec for a 90% response to a current step).